2015

Investigation of the numerical characteristics of the flowfield dependent variation method

Seyi Festus Olatoyinbo

INVESTIGATION OF THE NUMERICAL CHARACTERISTICS OF THE FLOWFIELD DEPENDENT VARIATION METHOD

by

SEYI FESTUS OLATOYINBO

A DISSERTATION

Submitted in partial fulfillment of the requirements
for the degree of Doctor of Philosophy
in
The Department of Mechanical and Aerospace Engineering
to
The School of Graduate Studies
of
The University of Alabama in Huntsville

HUNTSVILLE, ALABAMA

2015

In presenting this dissertation in partial fulfillment of the requirements for a doctoral degree from The University of Alabama in Huntsville, I agree that the Library of this University shall make it freely available for inspection. I further agree that permission for extensive copying for scholarly purposes may be granted by my advisor or, in his absence, by the Chair of the Department or the Dean of the School of Graduate Studies. It is also understood that due recognition shall be given to me and to The University of Alabama in Huntsville in any scholarly use which may be made of any material in this dissertation.

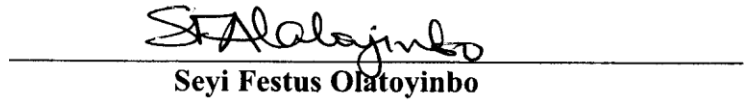

Seyi Festus Olatoyinbo

11/13/15

(Date)

DISSERTATION APPROVAL FORM

Submitted by Seyi Festus Olatoyinbo in partial fulfillment of the requirements for the degree of Doctor of Philosophy in Mechanical Engineering and accepted on behalf of the Faculty of the School of Graduate Studies by the dissertation committee.

We, the undersigned members of the Graduate Faculty of The University of Alabama in Huntsville, certify that we have advised and/or supervised the candidate of the work described in this dissertation. We further certify that we have reviewed the dissertation manuscript and approve it in partial fulfillment of the requirements for the degree of Doctor of Philosophy in Mechanical Engineering.

11/13/15 Committee Chair
Dr. K. Frendi (Date)

11/13/15
Dr. R.A. Frederick (Date)

11/13/15
Dr. S. S. Ravindran (Date)

11/16/15
Dr. B. Shotorban (Date)

11/13/2015
Dr. S. L. Rani (Date)

11/13/2015 Department Chair
Dr. Keith Hollingsworth (Date)

11/13/15 College Dean
Dr. Shankar Mahalingam (Date)

12/2/15 Graduate Dean
Dr. David Berkowitz (Date)

ABSTRACT

The School of Graduate Studies

The University of Alabama in Huntsville

Degree: Doctor of Philosophy College/Dept.: Engineering/Mechanical and Aerospace Engineering

Name of Candidate: Seyi Festus Olatoyinbo

Title: Investigation of the Numerical Characteristics of the Flowfield Dependent Variation Method

The Flowfield Dependent Variation (FDV) method is fundamentally derived from the Lax-Wendroff scheme (LWS) by replacing the explicit time derivatives in LWS with a weighted combination of explicit and implicit time derivatives. The increased implicitness and the intrinsic numerical dissipation of FDV contribute to the scheme's numerical stability, as well as monotonicity. The von Neumann stability analysis showed that FDV is more stable and less dispersive compared to LWS.

At first, a detailed investigation of spatial accuracy of the FDV scheme was conducted for grid and polynomial order convergence using the Method of Manufactured Solutions. The order-of-accuracy test, spanning both Euler and Navier-Stokes equations, showed that the observed order-of-accuracy of the scheme is nearly equal to the order of the shape function polynomial plus one, in good agreement with theory.

A new formulation was developed for quantifying the FDV numerical viscosity. Using this formulation, the intrinsic numerical viscosity and dissipation rate of the FDV scheme were quantified both in physical and spectral spaces, and compared with those of

the explicit subgrid-scale (SGS) models namely, the standard Smagorinsky and dynamic Smagorinsky models. Large-eddy simulations (LES) of incompressible freely decaying inviscid isotropic turbulence were performed involving the implicit LES approach using the FDV numerical dissipation and the two explicit SGS models. In the initial stages of turbulence development, all the three LES cases have similar viscosities. But, once the turbulence is fully developed, implicit LES is less dissipative compared to the two SGS LES runs. Furthermore, at a finite number of flow realizations, the numerical viscosities of FDV and of Streamline Upwind/Petrov-Galerkin (SUPG) finite element method were compared. It was observed that the SUPG method is significantly more dissipative than the three FDV-based LES approaches.

Simulations involving freely decaying viscous isotropic turbulence with and without an explicit SGS model were also performed, spanning both incompressible and compressible flow regimes. Results from the dynamic Smagorinsky model-based LES runs showed good agreement with the data from the experiments and those available in the published literature. These results suggest that the FDV scheme has potential for large-eddy simulations of free-shear turbulent flows.

Abstract Approval: Committee Chair 11/13/15
Dr. Kader Frendi

Department Chair 11/13/15
Dr. Keith Hollingsworth

Graduate Dean
Dr. David Berkowitz

ACKNOWLEDGEMENTS

First and foremost, I give all glory, honor and adoration to the Almighty God, the Author and Giver of life, for His sustaining grace that has kept me this far. He is God alone and worthy of my praise forever and ever, amen.

I am indebted to the leadership of the National Space Research & Development Agency (NASRDA), Nigeria for funding most part of my Ph.D. degree program. My sincere gratitude goes to Dr. Femi Agboola for his kindness and moral support.

Special thanks go to my advisor, Dr. Kader Frendi, for introducing me to the field of turbulent flows and for being available for consultation in the course of undertaking the research. Some valuable suggestions and insightful discussions with Dr. Sarma Rani are gratefully acknowledged. Thanks go to members of my dissertation committee for their constructive criticisms and for paying attention to my work at its various stages. My heartfelt appreciation goes to Ms. Claudia Meyering for her emotional support and administrative assistance. This research study would not have been made possible without the grant of high performance computing resources and technical support from the Alabama Supercomputer Authority who provided me with free CPU hours.

Finally, I am eternally grateful to my lovely wife and soulmate, Yetunde, and my wonderful children: Faith, Felicia and Felix, for all their sacrifices, prayers, love and unflinching moral support. With this awesome family of mine, my whole existence is complete.

TABLE OF CONTENTS

Page

LIST OF FIGURES

Figure Page

LIST OF TABLES

LIST OF LISTINGS

LIST OF SYMBOLS

SYMBOL	DEFINITION
$\boldsymbol{a}_i$	convection Jacobian tensor
$\boldsymbol{b}_i$	diffusion Jacobian tensor
c	wave speed
$\boldsymbol{c}_{ij}$	diffusion gradient Jacobian tensor
$\boldsymbol{c}_p$	specific heat at constant pressure
C	Courant number
C_{d}	dynamic Smagorinsky coefficient
C_{I}	normal stress constant
C_{s}	Smagorinsky constant
D	flow domain
DE_k	discretization error on grid level k
$\boldsymbol{\delta}_{ij}$	Knonecker delta $= \begin{cases} 1 \text{ if } i = j \\ 0 \text{ if } i \neq j \end{cases}$
$E(k)$	velocity field energy spectrum
e_t	total energy
f	turbulent field
$\boldsymbol{F}_i$	convective flux vector
G	filter kernel
$\boldsymbol{G}_i$	diffusive flux vector
γ	ratio of specific heats
h	grid spacing

h_k measure of element size on grid level k

Δ filter width

k thermal conductivity

k spectral wavenumber

L domain length

M Mach number

M_t turbulent Mach number

μ molecular viscosity

N number of grid nodes

n kinetic energy decay exponent

np observed order-of-accuracy

p pressure

Pr_t turbulent Prandtl number

φ_{exact} exact solution to partial differential equations

φ_k numerical solution to partial differential equations on grid level k

q_i conductive heat flux vector

q_i^{sgs} subgrid-scale heat flux vector

Q Q-criterion

R universal gas constant

Re Reynolds number

R_{ij} rotational-rate tensor

ρ fluid density

r grid refinement ratio

s_a first-order FDV parameter

s_b second-order FDV parameter

$s_{a,conv}$ first-order FDV parameter associated with convection

$s_{b,conv}$ second-order FDV parameter associated with convection

$s_{a,diff}$ first-order FDV parameter associated with diffusion

$s_{b,diff}$ second-order FDV parameter associated with diffusion

S_{ij} strain-rate tensor

σ_{ij} viscous stress tensor

T temperature

t time

τ_{ij}^{sgs} subgrid-scale stress tensor

θ_s sine or cosine function

u_i Cartesian velocity vector

$\boldsymbol{U}$ vector of conserved variables

$\boldsymbol{\nu}_{\mathrm{FDV}}$ numerical viscosity due to FDV method

ν_{sgs} turbulent eddy-viscosity

$\boldsymbol{\nu}_{\mathrm{SUPG}}$ numerical viscosity due to SUPG method

$\boldsymbol{\omega}$ vorticity vector

x, y Cartesian coordinates

Ω enstrophy

ϕ general solution variable

ACRONYMS

CFD	Computational Fluid Dynamics
DNS	Direct Numerical Simulation
EBE	Element-by-Element
FDV	Flowfield Dependent Variation method
FEM	Finite Element Method
FVM	Finite Volume Method
GLS	Galerkin/Least Squares method
GMRES	Generalized Minimal Residual
ILES	Implicit Large-Eddy Simulation
LES	Large-Eddy Simulation
LWS	Lax-Wendroff Scheme
MMS	Method of Manufactured Solutions
MPI	Message Passing Interface
RANS	Reynolds-Averaged Navier-Stokes simulation
SGS	Subgrid-Scale
SUPG	Streamline Upwind/Petrov-Galerkin method

To my family

CHAPTER 1

INTRODUCTION

This chapter is organized as follows. Section 1.1 presents an introductory review of the Flowfield Dependent Variation method, followed by a background of large-eddy simulation modeling approach in Section 1.2. The main objectives of the present research are provided in Section 1.3. Finally, a layout of the dissertation is discussed in Section 1.4.

1.1 Review of Flowfield Dependent Variation Method

During the past four to five decades, research in computational methods has resulted in a large number of numerical schemes for solving non-linear partial differential equations that govern the physics in fields such as fluid dynamics, magnetohydrodynamics, heat transfer, and combustion. An important area of current research is the development of numerical schemes that do not only perform well when applied to a specific aspect of physics, but also are robust and accurate when used for problems characterized by multiple regimes with widely varying spatial and temporal scales. One of such multi-regime problems in computational fluid dynamics involves the simultaneous occurrence of inviscid/viscous, incompressible/compressible, subsonic/supersonic, and laminar/turbulent flows in a domain e.g., shock-wave turbulent-boundary-layer interactions. Numerical solution of these flows presents complexities not only in terms of the multiplicity of physics, but also in terms of the numerically stiff linearized system of equations resulting from the large variations in flow parameters. For example, the velocity, Mach number and Reynolds number in the vicinity of a wall are very low, while away from the wall, high

velocities and Reynolds numbers occur. This transition from one flow regime to another and the interactions between the different regimes have been the subject of past and recent researches, both experimental and numerical [1–6].

The principal motivation for developing the Flowfield Dependent Variation (FDV) scheme [7, 8] was the desire for a common numerical method that can be successfully applied to problems with large gradients in fluid and flow variables (e.g., density, velocity, pressure, and temperature), rapid changes in characteristic parameters (e.g., Mach number, Reynolds number, Peclet number, and Damköhler number), as well as to multi-physics, multi-regime flows. It is possible to recover most of the current finite difference-, finite volume- and finite element-based schemes from FDV method as special cases [9].

In the context of the complex flow problems that motivated FDV, an active research area is the development of numerical schemes that can efficiently and accurately capture such flows without resorting to excessively fine grids and small time steps. To this end, one of the avenues being pursued by the computational researchers consists of developing higher order spatial and temporal schemes. Higher order methods hold significant potential due to the increased rates at which errors are reduced, thereby allowing the attainment of the desired accuracies on much coarser grids (commonly referred to as grid compression) and with larger time steps. Despite their favorable numerical properties, higher order methods are still not as commonplace as the lower order methods. Many of the existing high-order spatial discretization methods have tended to be somewhat less flexible in terms of how the flow domain is discretized. For example, finite-difference methods require nearly orthogonal alignment of grid points, while some finite-volume methods (e.g. *k*-exact, essentially non-oscillatory (ENO), and weighted essentially non-oscillatory

(WENO)) rely on wide mesh stencils to form higher order spatial reconstructions of functions in a grid cell. Due to their reliance on extended stencils, many of these methods require specialized treatment of boundary conditions in order to maintain accuracy, and also run into complications with solid bodies immersed in the flow domain (where, for example, the extended grid can start to wrap around the body). Methods that rely on extended stencils are also more difficult to parallelize due to their greater dependence on non-local data.

The Discontinuous Galerkin (DG) method, first proposed by Reed and Hill [10] in the context of neutron transport, and the more recent FDV method show promise in developing higher order spatial schemes for unstructured grids. The two methods, DG and FDV, share a number of common features. They are both locally conservative, stable and are well suited for *hp*-grid adaptation strategies (i.e., grid size and polynomial order adaptation). Both schemes entail solving the governing equations in their variational forms, with a higher order polynomial approximating the conserved variables. An important advantage of DG and FDV, compared to higher-order schemes discussed above (e.g., *k*-exact, ENO, and WENO), is that they both use compact stencils, thereby facilitating efficient parallelization. However, there are significant differences as well between DG and FDV. For instance, DG-based methods incorporate the features of both the Finite-Element Method (FEM) and the Finite-Volume Method (FVM) [11]. Like FEM, DG can attain high-order spatial accuracy locally through the use of higher order polynomial representation of the conserved variables. And, like FVM, DG does not inherently ensure flux continuity at elemental interfaces. Consequently, the solution approximation will typically be double-valued at cell interfaces, and flux continuity needs to be explicitly

enforced. In contrast, FDV is amenable to either FVM- or FEM-based spatial discretization, but the implementation in this study is based on FEM. Due to the basis in FEM, the current form of FDV facilitates access to the flux contour integrals, which automatically cancel each other along the inter-element faces insuring flux conservation.

However, the most significant difference between DG and FDV is perhaps related to the solution stabilization technique adopted in either method, especially for problems involving shock capture. Due to DG's FVM-like treatment of fluxes at cell interfaces, Total Variational Diminishing (TVD) schemes such as the Roe-MUSCL scheme are employed for the convective fluxes. The Roe-MUSCL scheme may be interpreted as an upwind flux formulation that ensures solution stability, but whose excessive diffusivity is moderated with an anti-diffusive flux that is controlled by a flux limiter. On the other hand, the FDV method is basically a variant of the Lax-Wendroff scheme (LWS), and achieves stability by imparting implicitness to LWS. This involves replacing the purely explicit first and second time derivatives in LWS with a weighted combination of explicit and implicit time derivatives. The weighting factors are designed such that the implicitness of the second time derivative varies from Crank-Nicholson-like to fully implicit; whereas that of the first derivative may vary between weighted implicit-explicit and fully explicit. Implicitness increases as the local gradients in the variables of interest increase. However, the second derivative is always treated implicitly (at least Crank-Nicholson) and this is, in fact, the most novel feature of FDV. The FDV method is a multi-speed numerical scheme that can be applied to flows with speeds ranging from very low Mach numbers ($\ll 1$) to high Mach numbers [12].

Prior applications of FDV method include: simulations of heat transfer and fluid dynamics problems [13], computation of non-ideal relativistic astrophysics and hydrodynamic flows [5, 6], prediction of ignition over-pressure in launch vehicle acoustics [14], and recently, the numerical simulations of low- to high-Mach number laminar flows [12]. None of the previous studies addressed the numerical characteristics of the FDV method. An important aspect in using a given numerical scheme for a particular application is the knowledge of its accuracy, dispersion and intrinsic numerical dissipation. Thus, the present study is motivated by the need to provide a better understanding of the numerical characteristics of the FDV scheme vis-à-vis its spatial order-of-accuracy, numerical stability, dispersion, intrinsic numerical dissipation, and applicability to large-eddy simulation of turbulent flows.

1.2 Background of Large-Eddy Simulation

Large-Eddy Simulation (LES) is a modeling approach for computation of turbulent flows where the large-scale structures, which contain most of the turbulent kinetic energy, are resolved and directly computed by the computational method, and the small-scale structures and their effect on the large scales are modeled by explicit subgrid-scale (SGS) models. LES has emerged as a viable modeling technique to simulate unsteady turbulent flows with large coherent structures in real engineering applications. This trend has been driven by the need to balance two competing requirements: finer resolution of flow physics and moderation of computational cost.

Large-eddy simulation is a compromise between Direct Numerical Simulation (DNS), which involves resolving all turbulent scales, and Reynolds-Averaged Navier-

Stokes (RANS) simulation, which consists of modeling the effects of all scales. Thus, LES is superior to RANS in providing insights into the underlying turbulence. It is also computationally less expensive than DNS, with the added advantage of overcoming the Reynolds numbers restriction on DNS. Therefore, LES is considered to be a suitable approach for three-dimensional (3-D) unsteady simulations of turbulent flows of practical engineering relevance [15]. The governing equations for LES consist of 3-D filtered Navier-Stokes equations. The filtered equations contain unclosed terms that represent the effects of the unresolved SGS eddies, which are typically closed through explicit SGS models. However, an alternative approach involves the use of dissipation inherent to the numerical scheme to emulate the role of the SGS models, commonly referred to as Implicit Large-Eddy Simulation (ILES).

In large-eddy simulation, a low-pass spatial filtering operation is applied to the instantaneous turbulent fields to remove turbulent motions of length scales smaller than the filter size Δ. For instance, the instantaneous velocity field $u(x,t)$ is decomposed into the sum of a filtered component $\bar{u}(x,t)$ and residual component $u'(x,t)$. Then, the filtered governing equations are solved numerically for $\bar{u}(x,t)$, which represents the motion of the large eddies and provides an approximation to the large-scale motions in one realization of the turbulent flow [16].

Large-eddy simulation has found applications in a variety of multi-scale problems such as: simulations of turbulent reacting flows including aircraft engine combustion [17], reciprocating engine combustion [18], solid rocket motor combustion [19], power-generating gas turbine combustors [20], and acoustic combustion instabilities [21];

predictions of jet noise [22], and pollutants formation [23]; meteorological flows, and atmospheric boundary layers computations [24]; etc.

Over the past five decades, research efforts have been devoted to LES beginning with Smagorinsky [25] and Lilly [26] who adopted LES to predict flows in the field of meteorology. In general, large-eddy simulations are carried out using finite-difference or finite-volume methods. Recently, LES in conjunction with the Finite-Element Method (FEM) has received some attention. The use of unstructured-grid FEM for LES was pioneered by Jansen [27] who studied flow over a NACA 4412 airfoil. The use of FEM for LES enables the simulation of flows within or around complex geometries normally found in engineering applications, and also reduction in computational effort required in such simulation through the use of unstructured adaptive grids locally in a region with fine-scale flow structures while the other regions with large flow structures remain coarse. Jansen [28] presented two FEM-based approaches, namely Galerkin/Least-Squares (GLS) and Streamline Upwind/Petrov-Galerkin (SUPG) methods, which are suitable for LES applications on unstructured grids. Chalot *et al.* [29] studied the use of GLS/FEM to perform LES of compressible flows, and found that the least-squares operator inherent to the GLS method is incapable of acting as a proper SGS model for decaying inviscid isotropic turbulence. Tejada-Martínez and Jansen [30] used SUPG/FEM formulation to simulate incompressible decaying isotropic turbulence with a dynamic Smagorinsky SGS model. Their work showed that the filter width ratio had a significant influence on LES predictions, while the type of test filter did not strongly impact the results. Levasseur *et al.* [31] used GLS/FEM formulation for simulating compressible decaying isotropic turbulence at infinite Reynolds numbers using the standard Smagorinsky, dynamic Smagorinsky, and

Variational Multiscale (VMS) SGS models. They showed that the least-squares stabilization is unsuitable for ILES calculations, and that the VMS SGS model performs favorably well compared to dynamic Smagorinsky SGS model.

1.3 Objectives of the Present Study

The principal objectives of this research study are to: (1) establish the spatial order of accuracy of the FDV scheme for both inviscid Euler and laminar Navier-Stokes equations; (2) characterize FDV numerical stability and dispersion (3) develop a new formulation for quantifying the numerical viscosity and dissipation rate inherent to the FDV scheme; (4) investigate the applicability of the FDV scheme to large-eddy simulation of turbulent flows; (5) establish that FDV's intrinsic numerical viscosity coupled with the scheme's implicitness are sufficient to maintain monotonicity and stability when simulating turbulent flows; (6) investigate the effects of including SGS models in LES predictions through the comparison of the conventional LES (based on explicit SGS models) to the implicit LES approach (based on intrinsic numerical viscosity of FDV).

This research study entails the development, verification and validation of an LES code with some benchmark problems. The code development involves the implementation of two explicit SGS closures, the standard Smagorinsky and dynamic Smagorinsky SGS models, as well as the implicit LES approach, in an in-house-developed, high-order compressible Navier-Stokes solver.

1.4 Dissertation Layout

The organization of this dissertation is presented in this section. The governing equations describing a compressible, viscous fluid flow are introduced in Chapter 2. These transport equations consist of the filtered Navier-Stokes equations based on grid- and test-filtering operations. Two subgrid-scale closures, namely the standard Smagorinsky and dynamic Smagorinsky models, and the SGS dissipation rate are also reviewed. A brief description of the test-filtering technique appropriate on finite element topology is presented in the last section of Chapter 2.

Chapter 3 gives a detailed description of the Flowfield Dependent Variation (FDV) method. Starting from the conservative form of the filtered Navier-Stokes equations, to the replacement of the explicit time derivatives of Lax-Wendroff scheme (LWS) with a weighted combination of explicit-implicit time derivatives, a step-wise derivation of the FDV method is presented. Introduction of the FDV parameters and their physical interpretations are briefly discussed. The latter sections of Chapter 3 describe the finite element formulation of the FDV method obtained by applying the standard Galerkin method to the residual form of the scheme. Expressions for numerical viscosities of SUPG and FDV methods, as well as the FDV dissipation rate are also presented.

The order-of-accuracy analysis of the FDV/FEM-based, high-order compressible Navier-Stokes solver is presented in Chapter 4. The Method of Manufactured Solutions (MMS) is briefly introduced, and the results from spatial order-of-accuracy test involving inviscid Euler and laminar Navier-Stokes equations, spanning both subsonic and supersonic flow regimes, are presented and analyzed.

The von Neumann stability analysis is conducted to assess FDV numerical stability in Chapter 5. Comparisons of the numerical stability and dispersion errors of FDV method to those of Lax-Wendroff scheme (LWS) are also presented and discussed.

Chapter 6 presents the quantification of the numerical dissipation inherent to the FDV method. The Euler form of decaying isotropic turbulence is commonly used when one is isolating and quantifying numerical dissipation. The numerical viscosity and dissipation rate inherent to the FDV scheme are quantified and compared with the corresponding quantities for the standard Smagorinsky and dynamic Smagorinsky SGS models. Also presented are comparisons of the FDV numerical viscosity and SGS eddy-viscosities with the SUPG numerical viscosity both in physical and spectral spaces.

In Chapter 7, the numerical validation tests involving freely decaying inviscid and viscous isotropic turbulence, spanning both incompressible and compressible flow regimes, are presented and analyzed.

Finally, conclusions of the research work and recommendations for future research are presented in Chapter 8.

CHAPTER 2

GOVERNING EQUATIONS

This chapter presents the governing equations describing a compressible, viscous fluid flow that are appropriate for simulations of turbulent flows. The basic Navier-Stokes equations are presented in Section 2.1, while the filtered Navier-Stokes equations suitable for large-eddy simulations are described in Section 2.2. Section 2.3 gives a brief description of the two subgrid-scale models employed. Discussion of the test-filtering techniques appropriate for finite element topology is presented in Section 2.4.

2.1 Navier-Stokes Equations

The governing equations describing a compressible viscous fluid flow are the conservation statements for mass, momentum and energy. The conservative formulation is necessary for capturing possible discontinuities in the flow at the correct velocity in numerical simulations [15]. Using the conservative form, the Navier-Stokes equations can be written as

$$\frac{\partial \rho}{\partial t} + \frac{\partial (\rho u_i)}{\partial x_i} = 0, \tag{2.1}$$

$$\frac{\partial (\rho u_j)}{\partial t} + \frac{\partial (\rho u_i u_j + p\delta_{ij})}{\partial x_i} = \frac{\partial (\sigma_{ij})}{\partial x_i}, \tag{2.2}$$

$$\frac{\partial (\rho e_t)}{\partial t} + \frac{\partial [(\rho e_t + p) u_i]}{\partial x_i} = -\frac{\partial q_i}{\partial x_i} + \frac{\partial (\sigma_{ij} u_j)}{\partial x_i}, \tag{2.3}$$

where ρ, u_i and p are the fluid density, fluid velocity vector and pressure, respectively. The total energy, viscous stress tensor and conductive heat flux vector are, respectively, given by

$$\rho e_t = \frac{p}{\gamma-1} + \frac{1}{2}\rho u_k u_k \,, \tag{2.4}$$

$$\sigma_{ij} = \mu(T)\left(\frac{\partial u_i}{\partial x_j} + \frac{\partial u_j}{\partial x_i} - \frac{2}{3}\frac{\partial u_k}{\partial x_k}\delta_{ij}\right), \tag{2.5}$$

$$q_i = -k(T)\frac{\partial T}{\partial x_i}, \tag{2.6}$$

where the dynamic viscosity $\mu(T)$ and thermal conductivity $k(T)$ are functions of temperature, and are accounted for by Sutherland's law given as

$$\mu(T) = \frac{C_1 T^{1.5}}{C_2+T}, \quad \text{and} \quad k(T) = \frac{C_3 T^{1.5}}{C_4+T}. \tag{2.7}$$

For air at moderate temperatures, the Sutherland's coefficients are: $C_1 = 1.458 \times 10^{-6}$ kg/(msK$^{1/2}$), $C_2 = 110.4$ K, $C_3 = 2.495 \times 10^{-3}$ kgm/(s^{3}K$^{3/2}$) and $C_4 = 194$ K [9]. The ideal-gas equation of state is used to close the transport equations and is given by

$$p = \rho R T, \tag{2.8}$$

where T is the temperature and R is the specific gas constant ($R = 287.058$ J/kgK for air).

Concisely, the governing equations for fluid mass, momentum and energy balance may be written in a conservative form as

$$\frac{\partial \boldsymbol{U}}{\partial t} + \frac{\partial \boldsymbol{F}_i}{\partial x_i} + \frac{\partial \boldsymbol{G}_i}{\partial x_i} = 0, \tag{2.9}$$

where

$$\boldsymbol{U} = \begin{bmatrix} \rho \\ \rho u_j \\ \rho e_t \end{bmatrix}, \boldsymbol{F}_i = \begin{bmatrix} \rho u_i \\ \rho u_i u_j + p\delta_{ij} \\ (\rho e_t + p)u_i \end{bmatrix}, \quad \boldsymbol{G}_i = \begin{bmatrix} 0 \\ -\sigma_{ij} \\ q_i - u_j \sigma_{ij} \end{bmatrix}. \tag{2.10}$$

Here, $\boldsymbol{U}$, $\boldsymbol{F}_i$ and $\boldsymbol{G}_i$ are the vectors of conserved variables, convective fluxes and diffusive fluxes, respectively.

2.2 Filtered Navier-Stokes Equations

This section presents the filtered Navier-Stokes equations suitable for large-eddy simulation (LES) of turbulent flows. Formally, these equations are obtained by applying "grid filter" operation to the Navier-Stokes equations thereby smoothing out the small fluctuations of the flowfield. Thus, by applying a spatial low-pass (in frequency domain) convolution filter to the Navier-Stokes equations, the scales of turbulence are separated to large-scale and small-scale structures.

The filtering operation (denoted by overbar) maintains only the large scales and can be written in physical space in terms of a convolution integral as [32]

$$\bar{f}(\boldsymbol{x}, t) = \int_D G(\boldsymbol{x} - \boldsymbol{x}') f(\boldsymbol{x}', t) d\boldsymbol{x}' \tag{2.11}$$

where $G(\boldsymbol{x})$ is the filter kernel satisfying the normalization condition, f is the turbulent field, D is the entire flow domain.

The turbulent field f is decomposed into large-scale ($\tilde{f}$) and small-scale (f') components based on filtering operation as

$$f = \tilde{f} + f', \tag{2.12}$$

where the Favre (density-weighted) filtering operation, typical of LES of compressible turbulence (denoted by tilde) and introduced by Favre [33] to avoid subgrid-scale terms in the continuity equation, is defined as

$$\tilde{f} = \frac{\overline{\rho f}}{\bar{\rho}}. \tag{2.13}$$

The conservative form of the filtered Navier-Stokes equations may then be written as [15]

$$\frac{\partial \bar{\rho}}{\partial t} + \frac{\partial (\bar{\rho}\tilde{u}_i)}{\partial x_i} = 0, \tag{2.14}$$

$$\frac{\partial (\bar{\rho}\tilde{u}_j)}{\partial t} + \frac{\partial [(\bar{\rho}\tilde{u}_i\tilde{u}_j) + \bar{p}\delta_{ij})}{\partial x_i} = \frac{\partial (\tilde{\sigma}_{ij})}{\partial x_i} - \frac{\partial \left(\tau_{ij}^{\mathrm{sgs}}\right)}{\partial x_i} + \frac{\partial (\bar{\sigma}_{ij} - \tilde{\sigma}_{ij})}{\partial x_i}, \tag{2.15}$$

$$\frac{\partial (\bar{\rho}\tilde{e}_t)}{\partial t} + \frac{\partial [(\bar{\rho}\tilde{e}_t + \bar{p})\tilde{u}_i]}{\partial x_i} = -\frac{\partial \tilde{q}_i}{\partial x_i} + \frac{\partial \left(\tilde{\sigma}_{ij}\tilde{u}_j\right)}{\partial x_i} - \frac{\partial [c_p q_i^{\mathrm{sgs}} + J_i - D_i - (\bar{q}_i - \tilde{q}_i)]}{\partial x_i}, \tag{2.16}$$

where the SGS turbulent diffusion and SGS viscous diffusion are expressed as

$$J_i = \frac{1}{2}\bar{\rho}(\widetilde{u_i u_k u_k} - \tilde{u}_i \widetilde{u_k u_k}), \tag{2.17}$$

$$D_i = \overline{\sigma_{ij} u_i} - \tilde{\sigma}_{ij}\tilde{u}_i \ . \tag{2.18}$$

Here, the filtered form of total energy, viscous stress tensor and conductive heat flux vector are, respectively, given by

$$\bar{\rho}\tilde{e}_t = \frac{\bar{p}}{\gamma - 1} + \frac{1}{2}\bar{\rho}\tilde{u}_k \tilde{u}_k \ , \tag{2.19}$$

$$\tilde{\sigma}_{ij} = \mu(\tilde{T})\left(\frac{\partial \tilde{u}_i}{\partial x_j} + \frac{\partial \tilde{u}_j}{\partial x_i} - \frac{2}{3}\frac{\partial \tilde{u}_k}{\partial x_k}\delta_{ij}\right), \tag{2.20}$$

$$\tilde{q}_i = -k(\tilde{T})\frac{\partial \tilde{T}}{\partial x_i}, \tag{2.21}$$

where T is the temperature, k is the thermal conductivity and c_p is the specific heat at constant pressure.

The resolved (large-scale) pressure is obtained from the filtered equation of state as

$$\bar{p} = \bar{\rho} R \tilde{T}. \tag{2.22}$$

The variations of dynamic viscosity and thermal conductivity with temperature are accounted for by the Sutherland's law, which are given by

$$\mu(\tilde{T}) = \frac{C_1 \tilde{T}^{1.5}}{C_2 + \tilde{T}}, \quad \text{and} \quad k(\tilde{T}) = \frac{C_3 \tilde{T}^{1.5}}{C_4 + \tilde{T}}. \tag{2.23}$$

The filtering operation leads to some extra terms in equations (2.15) and (2.16) that require closure. The SGS terms physically represent the effect of the unresolved scales on the resolved scales. Vreman *et al.* [34, 35] performed *a priori* tests using DNS data obtained from the calculation of a mixing layer at Mach numbers in the range of 0.2 and 0.6, and concluded that neglecting the SGS terms resulting from the non-linearities of the diffusive terms in the momentum and energy equations is acceptable especially at low Mach numbers. Therefore $\partial(\bar{\sigma}_{ij} - \tilde{\sigma}_{ij})/\partial x_i$ in the momentum equation, J_i, D_i and $\partial(\bar{q}_i - \tilde{q}_i)/\partial x_i$ in the energy equation are neglected in this study.

The SGS stress tensor and the SGS heat flux that both require modeling are defined as

$$\tau_{ij}^{\text{sgs}} = \bar{\rho}(\widetilde{u_i u_j} - \tilde{u}_i \tilde{u}_j), \tag{2.24}$$

$$q_i^{\text{sgs}} = \bar{\rho}(\widetilde{u_i T} - \tilde{u}_i \tilde{T}). \tag{2.25}$$

Concisely, the filtered Navier-Stokes equations suitable for LES may be written as

$$\frac{\partial \boldsymbol{U}}{\partial t} + \frac{\partial \boldsymbol{F}_i}{\partial x_i} + \frac{\partial \boldsymbol{G}_i}{\partial x_i} = 0, \tag{2.26}$$

where

$$\boldsymbol{U} = \begin{bmatrix} \bar{\rho} \\ \bar{\rho}\tilde{u}_j \\ \bar{\rho}\tilde{e}_t \end{bmatrix}, \boldsymbol{F}_i = \begin{bmatrix} \bar{\rho}\tilde{u}_i \\ \bar{\rho}\tilde{u}_i\tilde{u}_j + \bar{p}\delta_{ij} \\ (\bar{\rho}\tilde{e}_t + \bar{p})\tilde{u}_i \end{bmatrix}, \quad \boldsymbol{G}_i = \begin{bmatrix} 0 \\ -\tilde{\sigma}_{ij} + \tau_{ij}^{\text{sgs}} \\ \tilde{q}_i - \tilde{u}_j\tilde{\sigma}_{ij} + c_p q_i^{\text{sgs}} \end{bmatrix}. \tag{2.27}$$

Here, $\boldsymbol{U}$ is the vector of filtered conserved variables, $\boldsymbol{F}_i$ and $\boldsymbol{G}_i$ are the vectors of filtered convective fluxes and filtered diffusive fluxes in the x_i direction, respectively.

2.3 Subgrid-scale Closures

The two subgrid-scale (SGS) closures employed in this study are described in this section. These are the standard Smagorinsky and dynamic Smagorinsky SGS models. Though these SGS models are quite common, they have not been investigated using the FDV method implemented in a finite element framework. Section 2.3.1 gives a brief description of the standard Smagorinsky model, while the dynamic Smagorinsky model is reviewed in Section 2.3.2.

2.3.1 Smagorinsky Model

The first SGS model was developed for incompressible flows by Smagorinsky [25] based on an eddy-viscosity assumption, which implies that the turbulent kinetic energy production of the small-scale structures is balanced by the SGS dissipation. The model relates the turbulent eddy-viscosity as a function of resolved velocity field as

$$\nu_{\text{sgs}} = (C_{\text{s}}\bar{\Delta})^2 |\tilde{S}| \,, \tag{2.28}$$

where C_{s} is the Smagorinsky constant that takes the value ranging from 0.1 to 0.2 depending on the flow, the norm of the filtered strain-rate tensor is defined as

$$\left|\tilde{S}\right| = (2\tilde{S}_{ij}\tilde{S}_{ij})^{1/2} \,, \tag{2.29}$$

and the filtered strain rate-tensor is written as

$$\tilde{S}_{ij} = \frac{1}{2}\left(\frac{\partial \tilde{u}_i}{\partial x_j} + \frac{\partial \tilde{u}_j}{\partial x_i}\right). \tag{2.30}$$

The eddy-viscosity length scale or the grid filter width is calculated as

$$\bar{\Delta} = (\bar{\Delta}_x \bar{\Delta}_y \bar{\Delta}_z)^{1/3}, \tag{2.31}$$

where $\bar{\Delta}_x, \bar{\Delta}_y$, and $\bar{\Delta}_z$ are the grid sizes in the x-, y- and z-directions, respectively. This model is valid only if the filter width is in the inertial subrange. Scales in the inertial subrange are larger than the smallest or Kolmogorov universal scales yet smaller than the scales which contain most of the turbulent kinetic energy.

The standard Smagorinsky model is very popular and most widely used in LES calculations due to its simplicity. Its main drawbacks include: the flow dependency of its optimal value; incorrect asymptotic behavior near walls; over-dissipativeness in transition region between laminar and turbulent flows; inability to account for backscatter of energy from small scales to large scales; and exclusion of compressibility effects in the model [36].

The SGS stress tensor in equation (2.24) is modeled for compressible flows using the modification proposed by Moin *et al.* [36] to dynamic eddy-viscosity model of Germano *et al.* [37] for incompressible flows, and it is given by

$$\tau_{ij}^{\text{sgs}} - \tfrac{1}{3}\tau_{kk}^{\text{sgs}}\delta_{ij} = -2\bar{\rho}\nu_{\text{sgs}}\left(\tilde{S}_{ij} - \tfrac{1}{3}\tilde{S}_{kk}\delta_{ij}\right). \tag{2.32}$$

The isotropic part of the SGS stress tensor τ_{kk}^{sgs} is commonly neglected in low Mach number flows, and the model degenerates to the original Smagorinsky form.

For compressible applications, the trace of the SGS stress tensor is usually accounted for according to Yoshizawa [38] as

$$\tau_{kk}^{\mathrm{sgs}} = 2C_{\mathrm{I}}\bar{\rho}\bar{\Delta}^2\left|\tilde{S}\right|^2. \tag{2.33}$$

In the current study, the trace of the SGS stress tensor τ_{kk}^{sgs} is neglected as proposed by Erlebacher *et al.* [39]. They conjected that for turbulent Mach number $M_t < 0.4$, the effect of τ_{kk}^{sgs} is negligible; their DNS of isotropic turbulence confirmed this conjecture. Zang *et al*. [40] confirmed these results *a posteriori* by performing calculations with C_{I} ranging from 0 to theoretical value of 0.0066, and observed little difference in the LES results of compressible isotropic turbulence at low Mach number when τ_{kk}^{sgs} is neglected. Vreman *et al.* [35] confirmed the above findings with their simulation of 3-D compressible mixing layers at a mean convective Mach number of 0.2. In their *a priori* test, the SGS model that neglects τ_{kk}^{sgs} was found to be in better agreement with DNS results. Moreover, simulations conducted with a dynamic model for τ_{kk}^{sgs}were often unstable for the cases studied by Vreman *et al.* [35]. Therefore, neglecting the trace of SGS stress tensor in this work, which involves LES of low Mach number flows, will not introduce any appreciable errors.

To complete the closure of this model, the SGS heat flux vector given in equation (2.25) is modeled using the eddy-diffusivity model and a constant turbulent Prandtl number as

$$q_i^{\text{sgs}} = -\bar{\rho}\frac{\nu_{\text{sgs}}}{Pr_t}\frac{\partial \tilde{T}}{\partial x_i}\,. \tag{2.34}$$

2.3.2 Dynamic Smagorinsky Model

In order to adapt the Smagorinsky constant to local structure of the flow, Germano *et al*. [37] proposed an algorithm that enables the computation of a time- and space-dependent coefficient. Their original proposal for incompressible flows was later extended by Moin *et al*. [36] for compressible applications. The dynamic model is based on self-similarity of the inertial range of the kinetic energy spectrum at different length scales. Therefore, the same functional form for the subgrid-scale quantities can be assumed at the grid length scale $\bar{\Delta}$ representative of the computational grid and at a larger test filter length scale $\hat{\Delta}$. Details of the derivation can be found in Germano *et al.* [37] for incompressible flows and Moin *et al.* for the extension to compressible flows [36]. The residual stress at the test filter level T_{ij} appears when the test filter is applied to the grid-filtered Navier-Stokes equations. An identity due to Germano *et al*. [37] is then obtained by applying the test filter on the residual stresses at the grid filter level τ_{ij}^{sgs} and subtracting the resulting expression from T_{ij} thus

$$\mathcal{L}_{ij} = T_{ij} - \tau_{ij}^{\text{sgs}} = \widehat{\bar{\rho}\tilde{u}_i\tilde{u}_j} - (1/\hat{\bar{\rho}})\widehat{\bar{\rho}\tilde{u}_i}\widehat{\bar{\rho}\tilde{u}_j}\,. \tag{2.35}$$

Assuming that the same functional form, as in Smagorinsky model, could be used for the residual stresses at both levels, the modeled forms are:

$$\tau_{ij}^{\mathrm{sgs}} - \tfrac{1}{3}\tau_{kk}^{\mathrm{sgs}}\delta_{ij} = -2C_d\bar{\Delta}^2\bar{\rho}\left|\tilde{S}\right|\left(\tilde{S}_{ij} - \tfrac{1}{3}\tilde{S}_{kk}\delta_{ij}\right), \tag{2.36}$$

$$T_{ij} - \tfrac{1}{3}T_{kk}\delta_{ij} = -2C_{\mathrm{d}}\hat{\bar{\Delta}}^2\hat{\bar{\rho}}\left|\hat{\tilde{S}}\right|(\hat{\tilde{S}}_{ij} - \tfrac{1}{3}\hat{\tilde{S}}_{kk}\delta_{ij}). \tag{2.37}$$

Substituting equations (2.36) and (2.37) into equation (2.35), the modeled expression for deviatoric part of Leonard stress tensor $\boldsymbol{\mathcal{L}}_{ij}^{\mathrm{d}}$ is obtained as:

$$\boldsymbol{\mathcal{L}}_{ij}^{\mathrm{d}} = \boldsymbol{\mathcal{L}}_{ij} - \tfrac{1}{3}\boldsymbol{\mathcal{L}}_{kk}\delta_{ij} = C_{\mathrm{d}}\bar{\Delta}^2 M_{ij}\,, \tag{2.38}$$

where M_{ij} is defined as

$$M_{ij} = 2\overbrace{\bar{\rho}\left|\tilde{S}\right|(\tilde{S}_{ij} - \tfrac{1}{3}\tilde{S}_{kk}\delta_{ij})} - 2\left(\frac{\hat{\bar{\Delta}}}{\bar{\Delta}}\right)^2\hat{\bar{\rho}}\left|\hat{\tilde{S}}\right|\left(\hat{\tilde{S}}_{ij} - \tfrac{1}{3}\hat{\tilde{S}}_{kk}\delta_{ij}\right). \tag{2.39}$$

Finally, using a least-squares minimization procedure due to Lilly [41], one obtains:

$$C_{\mathrm{d}}\bar{\Delta}^2 = \frac{\langle(\boldsymbol{\mathcal{L}}_{ij} - \frac{1}{3}\boldsymbol{\mathcal{L}}_{kk}\delta_{ij})M_{ij}\rangle}{\langle M_{kl}M_{kl}\rangle}\,. \tag{2.40}$$

This procedure gives a local time-dependent estimate of the model coefficient $C_{\mathrm{d}}\bar{\Delta}^2$, which is updated at each time iteration. The quantities enclosed by angled bracket $\langle\cdot\rangle$ indicate that spatial averaging is to be performed over homogeneous directions. This is done to prevent numerical instabilities due to potential negative values of C_{d} or certain quantities from vanishing which could invalidate the evaluation of the model coefficient.

The turbulent Prandtl number in equation (2.34) is evaluated using a dynamic procedure similar to that described above. An expression similar to Germano's identity in equation (2.35) is obtained by subtracting the test filtered subgrid-scale heat flux q_i^{sgs} from the heat flux defined at the test filter level Q_i:

$$K_i = Q_i - q_i^{\mathrm{sgs}} = \widehat{\bar{\rho}\tilde{u}_\iota\tilde{T}} - (1/\hat{\bar{\rho}})\widehat{\bar{\rho}\tilde{u}_\iota}\widehat{\bar{\rho}\tilde{T}}. \tag{2.41}$$

The same eddy-diffusivity model is used for the heat flux at the test filter level as

$$Q_i = -\frac{C_{\mathrm{d}}\bar{\Delta}^2\hat{\bar{\rho}}|\hat{\tilde{S}}|}{Pr_{\mathrm{t}}}\frac{\partial\hat{\tilde{T}}}{\partial x_i}. \tag{2.42}$$

Therefore, substituting equations (2.34) and (2.42) into equation (2.41), the modeled form for K_i is obtained as

$$K_i = \frac{C_{\mathrm{d}}\bar{\Delta}^2}{Pr_{\mathrm{t}}}\left[\bar{\rho}\widehat{|\tilde{S}|\frac{\partial\tilde{T}}{\partial x_\iota}} - \hat{\bar{\rho}}\left(\frac{\hat{\bar{\Delta}}}{\bar{\Delta}}\right)^2|\tilde{S}|\frac{\partial\hat{\tilde{T}}}{\partial x_i}\right]. \tag{2.43}$$

Finally, following the procedure for computing the turbulent eddy-viscosity, a least-squares minimization technique [41] is used for evaluating the turbulent Prandtl number as

$$Pr_{\mathrm{t}} = C_{\mathrm{d}}\bar{\Delta}^2\frac{\langle N_i N_i\rangle}{\langle -K_j N_j\rangle}, \tag{2.44}$$

where N_i is given by

$$N_i = \left(\frac{\hat{\bar{\Delta}}}{\bar{\Delta}}\right)^2 \hat{\bar{\rho}} \left|\hat{\tilde{S}}\right| \frac{\partial \hat{\tilde{T}}}{\partial x_i} - \bar{\rho}\widehat{\left|\tilde{S}\right|} \frac{\partial \tilde{T}}{\partial x_i}. \tag{2.45}$$

The only adjustable parameter inherent to the dynamic model is the filter width ratio $\hat{\bar{\Delta}}/\bar{\Delta}$ taken as 2 in this study.

2.3.3 Subgrid-scale Dissipation Rate

Garnier *et al.* [42] proposed an expression for estimating the SGS dissipation rate as

$$\varepsilon_{\text{sgs}} = \langle \tilde{u}_i \partial_j \tau_{ij}^{\text{sgs}} \rangle, \tag{2.46}$$

where the SGS stress tensor τ_{ij}^{sgs} is given in equation (2.32) for compressible flow. Its incompressible flow version reduces to

$$\tau_{ij}^{\text{sgs}} = -2\bar{\rho}\nu_{\text{sgs}}\tilde{S}_{ij} \tag{2.47}$$

2.4. Element Level Filtering

The dynamic procedure requires the definition of an explicit, low-pass spatial filter for the test-filtering operation. Finite element filtering techniques suitable for unstructured grids have been studied by Jansen [28]. In his work, he proposed four different finite element-based filtering operators namely, the face-based filter, function-based filter, derivative-based filter, and generalized top hat (or box) filters. Some of these filters were implemented in a highly-parallelized code using SUPG/FEM formulation to perform LES of incompressible flows involving freely decaying isotropic turbulence and turbulent channel flow. Jansen [28] showed that the generalized top hat filter is not only the cheapest and the simplest to implement, but it is also the most successful filtering operator for finite element applications. Tejada-Martínez and Jansen [30] developed and tested two classes of finite element-based generalized top hat filters, the standard test filters (S1 and S2) and the wide test filters (W1 and W2), arising from Gaussian quadrature rule approximations on different finite element topologies (i.e., hexahedral, tetrahedral, and wedge elements). Here, S1/W1 and S2/W2 stand for standard/wide filters with one-point and two-point quadrature, respectively. Their work on incompressible decaying isotropic turbulence with a dynamic Smagorinsky SGS model showed that the type of test filter did not strongly impact the results as long as the filter width is consistently computed.

Based on the foregoing, a brief description of the finite element-based standard test filter employed for the current study is presented.

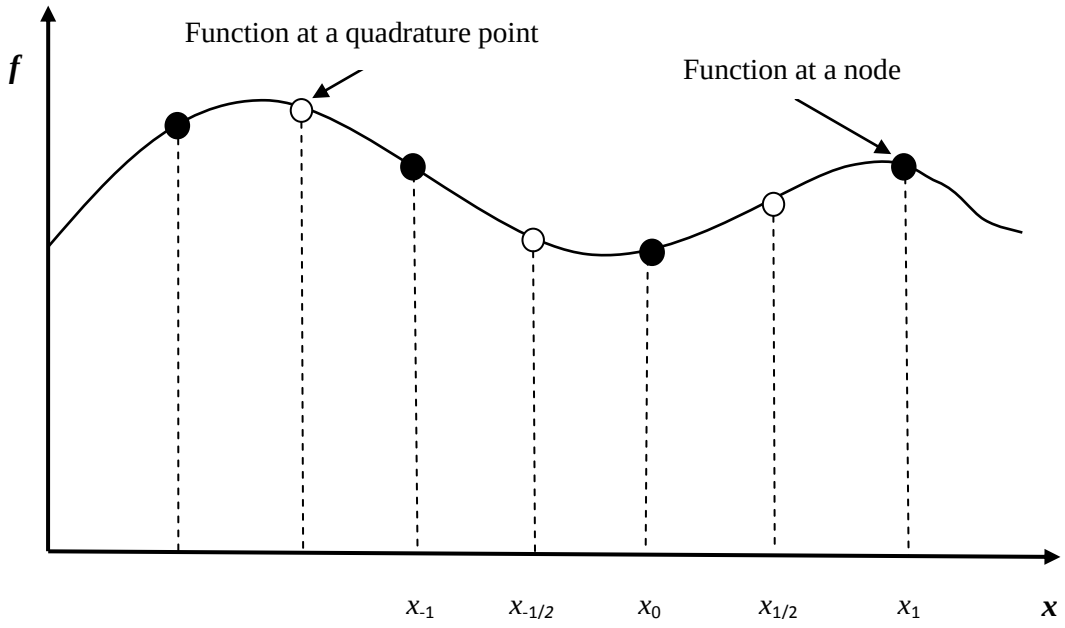

Figure 2.1 Sketch of function evaluation for finite element-based standard test filter.

Within the finite element framework, a generalized top hat filtered function at a node 0 located at x_0 on any grid topology, as shown in Figure 2.1, is written as [30]

$$\hat{f}(x_0) = \int_R G(x_0, \boldsymbol{y}) f(\boldsymbol{y}) d\boldsymbol{y}, \tag{2.48}$$

where integration is carried out over the entire real space. The region of integration is reduced to the union of elements which share node 0, denoted by Ω_o. The generalized top hat filter kernel at the vertex can be written as [30]

$$G(x_0, \boldsymbol{y}) = \begin{cases} \frac{1}{\text{volume}(\Omega_0)} & \text{if } \boldsymbol{y} \text{ is in } \Omega_0, \\ 0 & \text{otherwise.} \end{cases} \tag{2.49}$$

Using one-point quadrature (i.e., one function evaluation in the middle of an element, which is a line in one-dimensional case) to evaluate the filtering operation in equation (2.48), one obtains the filtered function at node 0, located at $x = x_0$, which is written as

$$\frac{1}{2h}\int_{x_{-1}}^{x_1} f(y)dy \approx \hat{f}\,(x_0) = \tfrac{1}{2}[f(x_{-1/2}) + f(x_{1/2})], \tag{2.50}$$

where h is the grid spacing between nodes used for the discretization.

The finite element-based standard test filters on regularly-connected quadrilateral (2-D) or hexahedral (3-D) elements reduce to products of their one-dimensional counterparts in x, y and/or z-directions. Therefore, any finite element-based test filtered function at nodal location $x = x_0$, on two- or three-dimensional regularly-connected topologies takes the form [30]:

$$\hat{f}(x_0) = \sum_{i=-J}^{J} W_i f(x_i), \tag{2.51}$$

where the number of function evaluations J is determined by the quadrature rule, $f(x_i)$ is the $f(x)$ evaluated at the i^{th} quadrature point symmetrically located about node x_0, and the filter weights W_i sums to one.

A general definition for the filter width on structured (i.e., regularly-connected) hexahedral elements is written as [43]

$$\hat{\Delta} = h(12\sum_{i=-J}^{J} W_i \lambda_i^2)^{1/2}, \tag{2.52}$$

where h is the grid spacing, and the coefficients λ_i, which define the function evaluation locations, are determined by the quadrature rule $(0 < \lambda_i < 1)$.

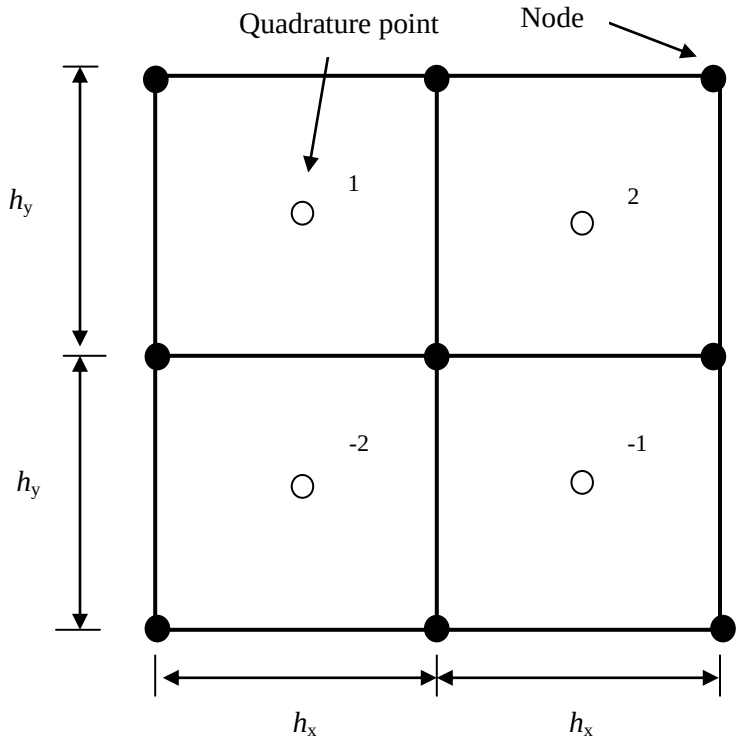

Figure 2.2 Sketch of regularly-connected rectangular grids.

As an illustration of a finite element-based standard test filter in two dimensions, one may consider test-filtering a function on the regularly-connected quadrilateral grids shown in Figure 2.2 using one-point quadrature. Such approximation leads to standard test filter on quadrilaterals and its filtered function can be determined using equation (2.51) with $J = 2$ and $W_i = 1/4$ for all i.

$$\hat{f}(x_0) = \sum_{i=-2}^{2} W_i f(x_i), \tag{2.53}$$

More detailed description of discrete test filters implemented on finite element topology can be found in Tejada-Martínez and Jansen [30, 43].

CHAPTER 3

METHOD OF SOLUTION

This chapter presents a detailed description of the Flowfield Dependent Variation (FDV) method implemented in a Taylor-Galerkin-based finite element framework. Section 3.1 details the derivation of the FDV method, while its residual form is presented in Section 3.2. The finite element formulation of FDV scheme is discussed in Section 3.3. A new formulation for quantifying FDV numerical viscosity is derived in Section 3.4. The numerical viscosity inherent to the Streamline Upwind Petrov/Galerkin (SUPG) finite element method and FDV dissipation rate are presented in Sections 3.5 and 3.6, respectively.

3.1 Flowfield Dependent Variation (FDV) Method

A conservative form of the filtered mass, momentum and energy equations describing a compressible flow may be written as

$$\frac{\partial \boldsymbol{U}}{\partial t} + \frac{\partial \boldsymbol{F}_i}{\partial x_i} + \frac{\partial \boldsymbol{G}_i}{\partial x_i} = 0, \tag{3.1}$$

where

$$\boldsymbol{U} = \begin{bmatrix} \bar{\rho} \\ \bar{\rho}\tilde{u}_j \\ \bar{\rho}\tilde{e}_t \end{bmatrix}, \quad \boldsymbol{F}_i = \begin{bmatrix} \bar{\rho}\tilde{u}_i \\ \bar{\rho}\tilde{u}_i\tilde{u}_j + \bar{p}\delta_{ij} \\ (\bar{\rho}\tilde{e}_t + \bar{p})\tilde{u}_i \end{bmatrix}, \quad \boldsymbol{G}_i = \begin{bmatrix} 0 \\ -\tilde{\sigma}_{ij} + \tau_{ij}^{\text{sgs}} \\ \tilde{q}_i - \tilde{u}_j\tilde{\sigma}_{ij} + c_p q_i^{\text{sgs}} \end{bmatrix}. \tag{3.2}$$

Here, $\boldsymbol{U}$ is the vector of filtered conserved variables, $\boldsymbol{F}_i$ and $\boldsymbol{G}_i$ are the vectors of filtered convective fluxes and filtered diffusive fluxes in the x_i direction, respectively.

Fundamentally, the FDV method may be considered as a variant of the Lax-Wendroff Scheme (LWS) that is obtained by replacing the explicit time derivatives in LWS with a weighted combination of explicit and implicit time derivatives. The increased implicitness and the inherent numerical dissipation of FDV contribute to the scheme's numerical stability, as well as monotonicity [12].

Lax-Wendroff scheme was originally developed for the numerical solution of linear, hyperbolic partial differential equations e.g., the one-dimensional linear wave advection equation expressed as:

$$f_t + cf_x = 0. \tag{3.3}$$

Here, c is the wave speed, and the subscripts t and x denote temporal and spatial derivatives, respectively. For this wave equation, LWS consists of the following time-explicit Taylor series expansion:

$$f^{n+1} = f^n + \Delta t f_t^n + \frac{\Delta t^2}{2} f_{tt}^n + O(\Delta t^3), \tag{3.4}$$

where the superscripts $n+1$ and n represent the current and previous time step levels, respectively, and Δt is the time step.

From equation (3.3), one obtains $f_t = -cf_x$ and $f_{tt} = c^2 f_{xx}$, which upon substitution into equation (3.4) gives

$$f^{n+1} = f^n - \Delta t c f_x^n + \frac{\Delta t^2}{2} c^2 f_{xx}^n + O(\Delta t^3) \quad (3.5)$$

The spatial derivatives f_x and f_{xx} are replaced by their respective second-order accurate central differencing approximations to yield the final finite-difference form of the LWS. It is a well-known fact that LWS provides barely minimum amount of dissipation that ensures solution stability, but not solution monotonicity.

In FDV method, the explicit time derivatives f_t^n and f_{tt}^n in equation (3.4) are replaced by a weighted combination of explicit-implicit time derivatives as follows:

$$f^{n+1} = f^n + \Delta t[(1 - s_a) f_t^n + s_a f_t^{n+1}] + \frac{\Delta t^2}{2}[(1 - s_b) f_{tt}^n + s_b f_{tt}^{n+1}] + O(\Delta t^3), \quad (3.6)$$

where the weighting factors s_a and s_b are referred to as the first- and second-order FDV parameters, respectively.

Applying the above weighted explicit-implicit method to equation (3.1) yields

$$\boldsymbol{U}^{n+1} = \boldsymbol{U}^n + \Delta t\left[(1 - \mathrm{s_a})\frac{\partial \boldsymbol{U}^n}{\partial t} + s_a \frac{\partial \boldsymbol{U}^{n+1}}{\partial t}\right] + \frac{\Delta t^2}{2}\left[(1 - \mathrm{s_b})\frac{\partial^2 \boldsymbol{U}^n}{\partial t^2} + s_b \frac{\partial^2 \boldsymbol{U}^{n+1}}{\partial t^2}\right] + O(\Delta t^3), \quad (3.7)$$

where $0 \leq \mathrm{s_a} \leq 1$ and $0 \leq \mathrm{s_b} \leq 1$. These FDV parameters, $\mathrm{s_a}$ and $\mathrm{s_b}$, act as weighting functions between explicit and implicit methods. If $\mathrm{s_a} = \mathrm{s_b} = 0$ (e.g., in the region of zero gradients in a flowfield), the method is fully explicit as in LWS; whereas if $\mathrm{s_a} = \mathrm{s_b} = 1$ (e.g., in the region of high gradients in flow variables), the method becomes fully implicit.

Rearranging equation (3.1) by separating the time and the spatial derivatives, one obtains

$$\frac{\partial \boldsymbol{U}}{\partial t} = -\frac{\partial \boldsymbol{F}_i}{\partial x_i} - \frac{\partial \boldsymbol{G}_i}{\partial x_i} \ . \tag{3.8}$$

Taking a time derivative of equation (3.8), interchanging spatial and time derivatives, and recognizing that $\boldsymbol{F}_i = \boldsymbol{F}_i(\boldsymbol{U})$, and $\boldsymbol{G}_i = \boldsymbol{G}_i(\boldsymbol{U}, \boldsymbol{U}_{,j})$, where $\boldsymbol{U}_{,j} = \partial \boldsymbol{U}/\partial x_j$, yields

$$\frac{\partial^2 \boldsymbol{U}}{\partial t^2} = \frac{\partial}{\partial x_i}\left[(\boldsymbol{a}_i + \boldsymbol{b}_i)\left\{\frac{\partial \boldsymbol{F}_j}{\partial x_j} + \frac{\partial \boldsymbol{G}_j}{\partial x_j}\right\}\right] + \frac{\partial^2}{\partial x_i \partial x_j}\left[\boldsymbol{c}_{ij}\left\{\frac{\partial \boldsymbol{F}_k}{\partial x_k} + \frac{\partial \boldsymbol{G}_k}{\partial x_k}\right\}\right]. \tag{3.9}$$

Here,
$$\boldsymbol{a}_i = \frac{\partial \boldsymbol{F}_i}{\partial \boldsymbol{U}} \ , \ \boldsymbol{b}_i = \frac{\partial \boldsymbol{G}_i}{\partial \boldsymbol{U}} \ , \ \boldsymbol{c}_{ij} = \frac{\partial \boldsymbol{G}_i}{\partial \boldsymbol{U}_{,j}} , \tag{3.10}$$

where $\boldsymbol{a}_i$, $\boldsymbol{b}_i$ and $\boldsymbol{c}_{ij}$ are the Jacobians of convection, diffusion and diffusion gradient, respectively.

Substituting equations (3.8) and (3.9) into equation (3.7), and neglecting the product of $\boldsymbol{c}_{ij}$ with the third-order spatial derivatives of $\boldsymbol{F}_k$ and $\boldsymbol{G}_k$ gives

$$\begin{aligned}\Delta \boldsymbol{U}^{n+1} = \Delta t &\left[\left\{-\frac{\partial \boldsymbol{F}_i^n}{\partial x_i} - \frac{\partial \boldsymbol{G}_i^n}{\partial x_i}\right\} + \mathrm{s_a}\left\{-\frac{\partial \Delta \boldsymbol{F}_i^{n+1}}{\partial x_i} - \frac{\partial \Delta \boldsymbol{G}_i^{n+1}}{\partial x_i}\right\}\right] \\ &+ \frac{\Delta t^2}{2}\frac{\partial}{\partial x_i}\left[(\boldsymbol{a}_i + \boldsymbol{b}_i)\left\{\frac{\partial \boldsymbol{F}_j^n}{\partial x_j} + \frac{\partial \boldsymbol{G}_j^n}{\partial x_j}\right\}\right] \\ &+ \frac{\Delta t^2}{2}\mathrm{s_b}\frac{\partial}{\partial x_i}\left[(\boldsymbol{a}_i + \boldsymbol{b}_i)\left\{\frac{\partial \Delta \boldsymbol{F}_j^{n+1}}{\partial x_j} + \frac{\partial \Delta \boldsymbol{G}_j^{n+1}}{\partial x_j}\right\}\right],\end{aligned} \tag{3.11}$$

where $\Delta \boldsymbol{U}^{n+1} = \boldsymbol{U}^{n+1} - \boldsymbol{U}^n$, $\Delta \boldsymbol{F}^{n+1} = \boldsymbol{F}^{n+1} - \boldsymbol{F}^n$ and $\Delta \boldsymbol{G}^{n+1} = \boldsymbol{G}^{n+1} - \boldsymbol{G}^n$.

Both qualitative and quantitative justification for neglecting the $\boldsymbol{c}_{ij}$ term in equation (3.9) is provided in Appendix A3.

In order to treat the effects of the FDV parameters on convection and diffusion terms separately, s_a and s_b are split into $s_{a,conv}/s_{a,diff}$ and $s_{b,conv}/s_{b,diff}$, respectively and reassigned as follow:

$$s_a \Delta \boldsymbol{F}_i \Rightarrow s_{a,conv} \Delta \boldsymbol{F}_i, \quad s_a \Delta \boldsymbol{G}_i \Rightarrow s_{a,diff} \Delta \boldsymbol{G}_i \,, \tag{3.12}$$

$$s_b \Delta \boldsymbol{F}_i \Rightarrow s_{b,conv} \Delta \boldsymbol{F}_i, \quad s_b \Delta \boldsymbol{G}_i \Rightarrow s_{b,diff} \Delta \boldsymbol{G}_i \,. \tag{3.13}$$

Physical roles are assigned to these implicitness parameters when their values are calculated from appropriate flow quantities such as Mach number (M) for convection and Reynolds number (Re) for diffusion. The first-order FDV parameters, $s_{a,conv}$ and $s_{a,diff}$, are flowfield-dependent, while the second-order parameters, $s_{b,conv}$ and $s_{b,diff}$, are assumed to have a power-law dependence on the first-order parameters as follow:

$$s_{a,conv} = \begin{cases} \min(r, 1) & r > \alpha \\ 0 \quad r > \alpha, & M_{min} \neq 0 \\ 1 & M_{min} = 0 \end{cases} \tag{3.14}$$

$$s_{b,conv} = \frac{1}{2}\left[1 + \left(s_{a,conv}\right)^{\eta}\right], \tag{3.15}$$

where $r = \frac{\sqrt{M_{max}^2 - M_{min}^2}}{M_{min}}$.

$$s_{a,diff} = \begin{cases} \min(r, 1) & r > \alpha \\ 0 \quad r < \alpha, & Re_{\min} \neq 0 \\ 1 & Re_{\min} = 0 \end{cases} \tag{3.16}$$

$$s_{b,diff} = \frac{1}{2}\left[1 + \left(s_{a,diff}\right)^{\eta}\right], \tag{3.17}$$

where $r = \frac{\sqrt{Re_{\max}^2 - Re_{\min}^2}}{Re_{\min}}$.

The maximum and minimum values of M and Re are calculated from the nodal values within the element. The η parameter impacts the stability (through implicitness) and monotonicity (through numerical viscosity) by controlling the values taken by $s_{b,conv}$ and $s_{b,diff}$. In previous studies on the FDV method [5, 8, 13], it was found that the parameter $\alpha = 0.001$ and $0.01 \leq \eta \leq 0.25$ provided good convergence behavior. Accordingly, the parameters $\alpha = 0.001$ and $\eta = 0.1$ are used in this study. The modification to the variation parameters, s_a and s_b, assists in maintaining the second-order temporal accuracy of the method and in adding stability to flows with stronger shocks [6]. All the *s*-parameters are updated at each time step. It is evident from equations (3.14) and (3.16) that in regions of zero or extremely small gradients in the flow variables (i.e., $r \sim \alpha = 0.01$), FDV becomes either fully or nearly explicit in the first derivative $\partial \boldsymbol{U}/\partial t$; simultaneously, it can be seen from equations (3.15) and (3.17) that FDV becomes Crank-Nicolson-like in terms of the second derivative $\partial \boldsymbol{U^2}/\partial t^2$. In regions of high gradients and discontinuities, $s_{a,conv}$ and $s_{b,diff}$ as well as $s_{b,conv}$ and $s_{b,diff}$ may approach unity, so that FDV becomes fully

implicit in both the first and second time derivatives. It is this implicitness that imparts both numerical stability and monotonicity to FDV when compared to LWS [12].

Rewriting equation (3.11) in terms of FDV parameters $s_{a,conv}$, $s_{a,diff}$ and $s_{b,diff}$, $s_{b,diff}$ yields

$$\Delta \boldsymbol{U}^{n+1} = -\Delta t \left[\left\{ \frac{\partial \boldsymbol{F}_i^n}{\partial x_i} + \frac{\partial \boldsymbol{G}_i^n}{\partial x_i} \right\} + \left\{ s_{a,conv} \frac{\partial \Delta \boldsymbol{F}_i^{n+1}}{\partial x_i} + s_{a,diff} \frac{\partial \Delta \boldsymbol{G}_i^{n+1}}{\partial x_i} \right\} \right] + \frac{\Delta t^2}{2} \frac{\partial}{\partial x_i} \left[(\boldsymbol{a}_i + \boldsymbol{b}_i) \left\{ \frac{\partial \boldsymbol{F}_j^n}{\partial x_j} + \frac{\partial \boldsymbol{G}_j^n}{\partial x_j} \right\} \right] + \frac{\Delta t^2}{2} \frac{\partial}{\partial x_i} \left[(\boldsymbol{a}_i + \boldsymbol{b}_i) \left\{ s_{b,conv} \frac{\partial \Delta \boldsymbol{F}_j^{n+1}}{\partial x_j} + s_{b,diff} \frac{\partial \Delta \boldsymbol{G}_j^{n+1}}{\partial x_j} \right\} \right]. \quad (3.18)$$

3.2 Residual Form

Replacing $\Delta \boldsymbol{F}_j^{n+1}$ and $\Delta \boldsymbol{G}_j^{n+1}$ with their respective Jacobians given in equation (3.10), then equation (3.18) can be written as

$$\left[\boldsymbol{I} + \boldsymbol{D}_i \frac{\partial}{\partial x_i} + \boldsymbol{E}_{ij} \frac{\partial^2}{\partial x_i \partial x_j} \right] \Delta \boldsymbol{U}^{n+1} = \boldsymbol{Q}^n , \quad (3.19)$$

where $\boldsymbol{I}$ is the identity matrix.

Finally, writing equation (3.19) in residual form gives the following expression:

$$\boldsymbol{R} = \Delta \boldsymbol{U}^{n+1} + \boldsymbol{D}_i^n \Delta \boldsymbol{U}_{,i}^{n+1} + \boldsymbol{E}_{ij}^n \Delta \boldsymbol{U}_{,ij}^{n+1} - \boldsymbol{Q}^n = O(\Delta t^3) , \quad (3.20)$$

such that

$$\boldsymbol{D}_i^n = \Delta t \left(s_{a,conv} \boldsymbol{a}_i + s_{a,diff} \boldsymbol{b}_i \right) , \quad (3.21)$$

$$\boldsymbol{E}_{ij}^{n} = \Delta t \mathrm{s}_{\mathrm{a,diff}} \boldsymbol{c}_{ij} - \frac{\Delta t^2}{2}\left[(\boldsymbol{a}_i + \boldsymbol{b}_i)(\mathrm{s}_{\mathrm{b,conv}} \boldsymbol{a}_j + \mathrm{s}_{\mathrm{b,diff}} \boldsymbol{b}_j)\right], \tag{3.22}$$

$$\boldsymbol{Q}^{n} = \Delta t\left(\boldsymbol{F}_{i,i}^{n} + \boldsymbol{G}_{i,i}^{n}\right) - \frac{\Delta t^2}{2}(\boldsymbol{a}_i + \boldsymbol{b}_i)\left(\boldsymbol{F}_{j,ji}^{n} + \boldsymbol{G}_{j,ji}^{n}\right). \tag{3.23}$$

The FDV method was first introduced by Yoon and Chung [7] and put in its final form by Chung [9]. Appendices A.1 and A.2 present the listing of filtered flow variables, the gradients and the Jacobians of the extra SGS terms that appear in the diffusive fluxes given in equation (3.2).

3.3 Finite Element Formulation

The choice of finite element formulation for the discretization of the FDV scheme is motivated by its ability to support unstructured grids on arbitrary complex geometry; its capability to exactly enforce Neumann boundary conditions without the use of any phantom nodes or other approximation; and its suitability for higher-order spatial accuracy [6]. Spatial resolution can be conveniently altered either by increasing the number of elements (h-refinement) or by increasing the order of shape function polynomial of the elements (p-refinement).

Evaluating the spatial derivatives $\Delta \boldsymbol{U}_{,i}^{n+1}$ and $\Delta \boldsymbol{U}_{,ij}^{n+1}$ in equation (3.20) would involve the conserved variables in terms of shape functions Φ_β as follows:

$$\boldsymbol{U}(x,t) = \Phi_\beta(x)\boldsymbol{U}_\beta(t) \text{ or } \boldsymbol{U}_{\boldsymbol{s}}(x,t) = \Phi_\beta(x)\boldsymbol{U}_{\beta s}(t), \tag{3.24}$$

where Φ_β is the shape function corresponding to the node with global index β; $s = 1,2,\ldots,5$ is the index for the five conserved variables; and the repeated Greek index β denotes summation over the nodes in an element.

Substituting equation (3.24) into equation (3.20), then applying the standard Galerkin method yields

$$\int_\Omega \Phi_\alpha \boldsymbol{R}(\boldsymbol{U}, \boldsymbol{F}_i, \boldsymbol{G}_i) d\Omega = 0, \tag{3.25}$$

where Φ_α is a shape function corresponding to the node with global index α. Here, the Langrange family of shape functions is employed for the polynomial representation of the conserved variables.

Integrating by parts of equation (3.25), and arranging in a compact form, the global form of the assembled element equations are given by

$$\left(A^n_{\alpha\beta rs} + B^n_{\alpha\beta rs}\right)\Delta U^{n+1}_{\beta s} = H^n_{\alpha r} + N^n_{\alpha r} \tag{3.26}$$

where

$$A^n_{\alpha\beta rs} = \int_\Omega \left(\Phi_\alpha \Phi_\beta \delta_{rs} - \Phi_{\alpha,i}\Phi_\beta D^n_{irs} - \Phi_{\alpha,i}\Phi_{\beta,j}E^n_{ijrs}\right) d\Omega \tag{3.27}$$

$$B^n_{\alpha\beta rs} = \int_\Gamma \left(\overset{*}{\Phi}_\alpha \overset{*}{\Phi}_\beta \overset{*}{D}{}^n_{irs} + \overset{*}{\Phi}_\alpha \overset{*}{\Phi}_{\beta,j} \overset{*}{E}{}^n_{ijrs}\right) n_i d\Gamma \tag{3.28}$$

$$H^n_{\alpha r} = \int_\Omega \left(\Delta t \Phi_{\alpha,i}(F^n_{ir} + G^n_{ir}) - \frac{\Delta t^2}{2}\Phi_{\alpha,i}(a_{irs} + b_{irs})\left(F^n_{js,j} + G^n_{js,j}\right)\right) d\Omega \tag{3.29}$$

$$N_{\alpha r}^{n} = \int_{\Gamma} \left(-\Delta t \overset{*}{\Phi}_{\alpha} \left(\overset{*}{F}_{ir}^{n} + \overset{*}{G}_{ir}^{n} \right) + \frac{\Delta t^2}{2} \overset{*}{\Phi}_{\alpha} (a_{irs} + b_{irs}) \left(\overset{*}{F}_{js,j}^{n} + \overset{*}{G}_{js,j}^{n} \right) \right) n_i d\Gamma \quad (3.30)$$

In equations (3.27)-(3.30), α and β denote the global nodal indices; $r, s = 1, 2, \ldots, 5$ are the indices for the five conserved variables; $i, j = 1, 2, 3$ are the physical coordinate indices; δ_{rs} represents the Kronecker delta; the superscript * represents the variable along the inter-element contour; the integral over Ω and Γ denote the element and contour integral, respectively; and n_i is the normal to the element surface. One very distinct feature of finite element methods, in general, is the automatic continuity of fluxes along the interfaces of any kind of elements. This is achieved by simply neglecting all contour integrals in the element equations, which is believed to include all the numerical treatments necessary to handle different flow situations spanning the low- and the high-Mach number spectrum. The contour integrals of equations (3.28) and (3.30) cancel each other along inter-element boundaries thereby ensuring flux conservation. Neumann boundary conditions can be imposed through these contour integrals, while Dirichlet boundary conditions can be enforced through element-by-element discretization approach.

Upon assembling equation (3.26) for all elements, the global linear system will be of the form:

$$\mathbf{AX} = \mathbf{F}, \quad (3.31)$$

where **A** is the global stiffness matrix of size $n_t \times n_t$, **F** is the right hand side vector of length n_t, and **X** is the vector of unknowns of length n_t. By definition

$$n_t = \sum_{i=1}^{NN} NEQ_i \ , \tag{3.32}$$

where NEQ_i is the number of unknowns at the i^{th} node and NN is the total number of nodes in the grid. Rewriting equation (3.31) in the EBE format gives [9]:

$$\bigcup_{e=1}^{NE} A_{\alpha\beta}^{(e)} X_{\beta}^{(e)} \hat{\Delta}_{\alpha i}^{(e)} = \bigcup_{e=1}^{NE} F_{\alpha}^{(e)} \hat{\Delta}_{\alpha i}^{(e)}, \tag{3.33}$$

where NE is the total number of elements in the grid, and $\hat{\Delta}_{\alpha i}^{(e)}$ is a Boolean matrix derived from the grid connectivity matrix with nonzero values only if local unknown α in element $E^{(e)}$ corresponds to global unknown i.

3.4 Numerical Viscosity of the FDV Method

In this section, a new expression for the numerical viscosity inherent to the FDV method is derived. Since the numerical dissipation primarily arises from the convective terms, only the Euler form of the governing equations is considered for the derivation. Considering the Euler form of the filtered momentum equation given by

$$\frac{\partial(\bar{\rho}\tilde{u}_i)}{\partial t} + \frac{\partial(\bar{\rho}\tilde{u}_i\tilde{u}_j)}{\partial x_j} = 0 \tag{3.34}$$

Rearranging equation (3.34) by separating the time and the spatial derivatives gives

$$\frac{\partial(\bar{\rho}\tilde{u}_i)}{\partial t} = -\frac{\partial(\bar{\rho}\tilde{u}_i\tilde{u}_j)}{\partial x_j} \tag{3.35}$$

Taking a time derivative of equation (3.35), one obtains

$$\frac{\partial^2(\bar{\rho}\tilde{u}_i)}{\partial t^2} = \frac{\partial}{\partial t}\left[-\frac{\partial(\bar{\rho}\tilde{u}_i\tilde{u}_j)}{\partial x_j}\right] = -\frac{\partial}{\partial x_j}\left[\frac{\partial(\bar{\rho}\tilde{u}_i\tilde{u}_j)}{\partial t}\right] \tag{3.36}$$

Differentiating equation (3.36) by product rule, substituting equation (3.35) and changing the repeated indices yields

$$\frac{\partial^2(\bar{\rho}\tilde{u}_i)}{\partial t^2} = \frac{\partial}{\partial x_j}\left[\tilde{u}_j\left\{\frac{\partial(\bar{\rho}\tilde{u}_i\tilde{u}_k)}{\partial x_k}\right\} - \bar{\rho}\tilde{u}_i\frac{\partial\tilde{u}_j}{\partial t}\right] \tag{3.37}$$

Taking a product rule differentiation of equation (3.37) and neglecting the time derivative term gives

$$\frac{\partial^2(\bar{\rho}\tilde{u}_i)}{\partial t^2} = \frac{\partial}{\partial x_j}\left[\tilde{u}_j\left\{\bar{\rho}\tilde{u}_i\frac{\partial\tilde{u}_k}{\partial x_k} + \tilde{u}_k\frac{\partial(\bar{\rho}\tilde{u}_i)}{\partial x_k}\right\}\right] \tag{3.38}$$

Expanding equation (3.38) about its second-order spatial derivatives yields

$$\frac{\partial^2(\bar{\rho}\tilde{u}_i)}{\partial t^2} = \frac{\partial}{\partial x_j}\left[\bar{\rho}\tilde{u}_j\tilde{u}_i\frac{\partial\tilde{u}_k}{\partial x_k}\right] + \frac{\partial}{\partial x_j}\left[\tilde{u}_j\tilde{u}_k\frac{\partial(\bar{\rho}\tilde{u}_i)}{\partial x_k}\right] \tag{3.39}$$

Re-writing equation (3.39) in tensorial form gives

$$\frac{\partial^2(\bar{\rho}\tilde{u}_i)}{\partial t^2} = \nabla \cdot \left[(\bar{\rho}\tilde{u}_j\tilde{u}_i)\{\nabla \cdot \tilde{\boldsymbol{u}}\}\right] + \nabla \cdot \left[\tilde{u}_j\tilde{u}_k \cdot \nabla(\bar{\rho}\tilde{\boldsymbol{u}})\right] \tag{3.40}$$

Recalling that the numerical diffusion term may be expressed in tensorial form as $[\nabla \cdot (\boldsymbol{D} \cdot \nabla(\bar{\rho}\tilde{\boldsymbol{u}}))]$, it can be recognized that the first term on the right-hand side of equation (3.40) is not a diffusion term, and the second term provides the numerical diffusion in the FDV method. Equation (3.40) can be approximated by

$$\frac{\partial^2(\bar{\rho}\tilde{u}_i)}{\partial t^2} \approx \nabla \cdot [(\tilde{\boldsymbol{u}}\tilde{\boldsymbol{u}}) \cdot \nabla(\bar{\rho}\tilde{\boldsymbol{u}})] = \frac{\partial}{\partial x_j}\left[\tilde{u}_j\tilde{u}_k \frac{\partial(\bar{\rho}\tilde{u}_i)}{\partial x_k}\right] \tag{3.41}$$

Performing a Taylor series expansion of $(\bar{\rho}\tilde{u}_i)^{n+1}$ about $(\bar{\rho}\tilde{u}_i)^n$ gives

$$(\bar{\rho}\tilde{u}_i)^{n+1} = (\bar{\rho}\tilde{u}_i)^n + \Delta t \frac{\partial(\bar{\rho}\tilde{u}_i)^n}{\partial t} + \frac{\Delta t^2}{2}\frac{\partial^2(\bar{\rho}\tilde{u}_i)^n}{\partial t^2} + O(\Delta t^3) \tag{3.42}$$

Replacing the explicit time derivatives in equation (3.42) by a weighted explicit-implicit combination using the convective FDV parameters, $s_{\mathrm{a,conv}}$ and $s_{\mathrm{b,conv}}$, and taking $\Delta(\bar{\rho}\tilde{u}_i)^{n+1} = (\bar{\rho}\tilde{u}_i)^{n+1} - (\bar{\rho}\tilde{u}_i)^n$ yields

$$\begin{aligned}\Delta(\bar{\rho}\tilde{u}_i)^{n+1} = \Delta t &\left[\left(1 - \mathrm{s}_{\mathrm{a,conv}}\right)\frac{\partial(\bar{\rho}\tilde{u}_i)^n}{\partial t} + \mathrm{s}_{\mathrm{a,conv}}\frac{\partial(\bar{\rho}\tilde{u}_i)^{n+1}}{\partial t}\right] \\ &+ \frac{\Delta t^2}{2}\left[\left(1 - \mathrm{s}_{\mathrm{b,conv}}\right)\frac{\partial^2(\bar{\rho}\tilde{u}_i)^n}{\partial t^2} + \mathrm{s}_{\mathrm{b,conv}}\frac{\partial^2(\bar{\rho}\tilde{u}_i)^{n+1}}{\partial t^2}\right]\end{aligned} \tag{3.43}$$

Substituting equations (3.35) and (3.41) into equation (3.43), and recognizing that the second-order time derivatives contain the numerical diffusion terms, one obtains

$$\frac{\Delta(\bar{\rho}\tilde{u}_i)^{n+1}}{\Delta t} \approx \frac{\Delta t}{2}\left[\left(1-\mathrm{s_{b,conv}}\right)\left\{\frac{\partial}{\partial x_j}\left[\tilde{u}_j\tilde{u}_k\,\frac{\partial(\bar{\rho}\tilde{u}_i)}{\partial x_k}\right]\right\}^{n}+\mathrm{s_{b,conv}}\left\{\frac{\partial}{\partial x_j}\left[\tilde{u}_j\tilde{u}_k\,\frac{\partial(\bar{\rho}\tilde{u}_i)}{\partial x_k}\right]\right\}^{n+1}\right] \qquad (3.44)$$

The numerical viscosity tensor can be quantified from the coefficients of the second-order spatial derivatives given in equation (3.44) and is expressed as

$$\nu_{\mathrm{FDV},jk} = \frac{\Delta t}{2}\left[\tilde{u}_j\tilde{u}_k\right] = \frac{1}{2}C\Delta x|\tilde{\boldsymbol{u}}|\tilde{u}_j^*\tilde{u}_k^*\,, \qquad (3.45)$$

where the Courant number $C = \Delta t|\tilde{\boldsymbol{u}}|/\Delta x$, $|\tilde{\boldsymbol{u}}|$ is the magnitude of the velocity vector, and $\tilde{u}_j^* = \tilde{u}_j/|\tilde{\boldsymbol{u}}|$ is a scaled velocity. It should be noted that the numerical viscosity $\boldsymbol{\nu}_{\mathrm{FDV}}$ is a second order tensor. One can use a lower dimensional quantification of $\boldsymbol{\nu}_{\mathrm{FDV}}$ by considering its Frobenius norm given by

$$\|\boldsymbol{\nu}_{\mathrm{FDV}}\|_F = \sqrt{\sum_{j=1}^{3}\sum_{k=1}^{3}{\nu_{\mathrm{FDV},jk}}^2}\,. \qquad (3.46)$$

3.5 Numerical Viscosity of the SUPG Method

In this section, an expression for the numerical viscosity inherent to the Streamline Upwind Petrov/Galerkin (SUPG) finite element method is presented. This is necessary for

comparative study between the numerical viscosity of FDV and that of SUPG finite element method reported in Chapter 6.

In the seminal SUPG study of Brooks and Hughes [44], the following form was provided for the added numerical viscosity on a uniform hexahedral grid:

$$\nu_{\mathrm{SUPG},jk} = \frac{1}{\sqrt{15}}\Delta x\left(\bar{\xi}\tilde{u}_1 + \bar{\eta}\tilde{u}_2 + \bar{\zeta}\tilde{u}_3\right)\tilde{u}_j^*\tilde{u}_k^*\,, \tag{3.47}$$

where the parameters $\bar{\xi}, \bar{\eta}$, and $\bar{\zeta}$ are based on the cell Peclet or Reynolds number; $\tilde{u}_1 = \tilde{\boldsymbol{u}}\cdot e_1$, $\tilde{u}_2 = \tilde{\boldsymbol{u}}\cdot e_2$, and $\tilde{u}_3 = \tilde{\boldsymbol{u}}\cdot e_3$ are designed so that the numerical viscosity is only active along the principal flow direction (hence, streamline upwind). When solving Euler equations, as in the current study, the cell Reynolds number $Re \to \infty$, for which the parameters $\bar{\xi}, \bar{\eta}$, and $\bar{\zeta}$ are all unity. Therefore, one obtains

$$\nu_{\mathrm{SUPG},jk} = \frac{1}{\sqrt{15}}\Delta x|\tilde{u}_1 + \tilde{u}_2 + \tilde{u}_3|\tilde{u}_j^*\tilde{u}_k^*\,, \tag{3.48}$$

where $|\tilde{u}_1 + \tilde{u}_2 + \tilde{u}_3|$ is considered to ensure positive numerical viscosity [44]. One can notice a striking similarity between the FDV and SUPG formulations for the numerical viscosity. For instance, when Courant number $C = 2|\tilde{u}_1 + \tilde{u}_2 + \tilde{u}_3|/\left(\sqrt{15}|\tilde{\boldsymbol{u}}|\right)$, the two methods would provide identical diffusion. It should be noted that the numerical viscosity $\boldsymbol{\nu}_{\mathrm{SUPG}}$ is a second order tensor. One can use a lower dimensional quantification of $\boldsymbol{\nu}_{\mathrm{SUPG}}$ by considering its Frobenius norm given by

$$\|\boldsymbol{\nu}_{\mathrm{SUPG}}\|_F = \sqrt{\sum_{j=1}^{3}\sum_{k=1}^{3} {\nu_{\mathrm{SUPG},jk}}^2}\,. \tag{3.49}$$

3.6 Numerical Dissipation Rate of the FDV Method

The numerical dissipation rate in the filtered momentum equation can be estimated as [42]

$$\varepsilon_{\mathrm{num}} = \langle \tilde{u}_i \frac{\partial \mathcal{F}_{ij}^{\mathrm{FDV}}}{\partial x_j} \rangle, \tag{3.50}$$

where

$$\mathcal{F}_{ij}^{\mathrm{FDV}} = \left(\bar{\rho}\tilde{u}_i\tilde{u}_j + \delta_{ij}\bar{p}\right). \tag{3.51}$$

Here, $\mathcal{F}_{ij}^{\mathrm{FDV}}$is the filtered convective flux in the momentum equation. It may be noted that the FDV parameters act on the momentum equation as well as the continuity and energy equations. Nevertheless, only the contribution from the momentum equation is considered in the calculation of the numerical dissipation rate to enable direct comparison with the SGS dissipation rate given in equation (2.46).

CHAPTER 4

SPATIAL ACCURACY OF THE FDV METHOD

This chapter presents the results of the spatial order-of-accuracy test carried out with an in-house-developed, high-order, compressible Navier-Stokes solver. The Navier-Stokes solver employs a mixed explicit-implicit numerical scheme, namely the flowfield dependent variation method implemented in a finite element framework that supports arbitrarily high-order, unstructured, isoparametric elements in one-, two- and three-dimensional geometries. However, it should be noted that the grids used for all the flows under consideration consisted of Cartesian (orthogonal), hexahedral elements in three-dimension (3-D) and quadrilateral elements in two-dimension (2-D). The FDV method is second-order accurate in time but its spatial order-of-accuracy is dependent on the interpolation functions used to evaluate its spatial derivatives. Element-by-Element (EBE) data storage is used for the linear system storage and the Generalized Minimal RESidual (GMRES) iterative solver is employed for its solution. Domain decomposition and optimized load balancing are achieved through METIS software package [45]. A distributed memory model based on EBE data structure is developed with Message Passing Interface (MPI) library for parallel processing. Detailed documentation and parallel performance of the Navier-Stokes solver are reported in Girgis [46].

Section 4.1 gives a concise review of the order-of-accuracy analysis, followed by a brief description of the Method of Manufactured Solutions (MMS) in Section 4.2. Discussion of the spatial order-of-accuracy results obtained for both inviscid Euler and laminar Navier-Stokes equations is presented in Section 4.3.

4.1 Order-of-Accuracy Analysis

The most rigorous code verification test is the order-of-accuracy test [47, 48], which determines whether the observed order-of-accuracy of the discretized solutions asymptotically approaches the formal order-of-accuracy of the discretization method as the grid is refined [49, 50]. It is recognized that the theoretical order-of-accuracy may not be attained due to coding errors, defective numerical algorithms, insufficiently smooth solutions, subtleties in nonlinear problems, overly strong grid stretching, failure to attain the asymptotic grid convergence range, etc. [49, 51]. For the finite element method used in the current code, the formal order-of-accuracy is determined by the interpolation theory.

In general, commercially-licensed CFD codes employ low-order methods that are formally second-order accurate in space, and require very large grids to resolve complex problems. In a bid to reduce computational time (i.e., through lesser number of iterations towards steady-state convergence) and memory requirements, the current in-house-developed research code utilizes high-order finite element method that can use much smaller grids to accurately capture complex physics such as laminar instabilities and turbulence.

In order to evaluate the observed order-of-accuracy, there is need to estimate the discretization errors in the simulation results. Discretization error is defined as a measure of the difference between the exact solution to the governing equations and the numerical solution to the discretized equations [49].

Consider a series expansion of the discretization error in terms of h_j, a measure of the element size on grid level j, then

$$\mathrm{DE}_j = \varphi_j - \varphi_{\mathrm{exact}} = \mathrm{C}h_j^{np} + \mathrm{HOT}, \tag{4.1}$$

where φ_j is the numerical solution on grid level j, φ_{exact} is the exact solution, C is the coefficient of the leading-error term and np is the observed order-of-accuracy. Here, it is assumed that the leading-order error term dominates the total discretization error. Thus, the grid spacing h is in the asymptotic range [47]. Therefore, the higher order terms (HOT) can be neglected. The discretization error equations for a fine and coarse grid levels k and $k+1$ can be written as

$$\mathrm{DE}_k = \varphi_k - \varphi_{\mathrm{exact}} = \mathrm{C}h_k^{np}, \tag{4.2}$$

$$\mathrm{DE}_{k+1} = \varphi_{k+1} - \varphi_{\mathrm{exact}} = \mathrm{C}h_{k+1}^{np}. \tag{4.3}$$

Since the exact solution φ_{exact} is known, equations (4.2) and (4.3) can be solved for the observed order-of-accuracy np. Let the grid refinement ratio, which is the ratio of coarse grid to fine grid spacing, be denoted by r (i.e., $r = h_{k+1}/h_k$), then the expression for the observed order-of-accuracy becomes:

$$np^k = \frac{In(\mathrm{DE}_{k+1}/\mathrm{DE}_k)}{In(r)}. \tag{4.4}$$

Theoretically, the formal order-of-accuracy, np, and the order of the shape function polynomial, p, are related by $np \approx p + 1$ [52]. The observed order-of-accuracy can be calculated either locally within the solution domain or globally by employing any appropriate error norms. In order to examine the behavior of global discretization error, both the discrete L_2 and L_∞ norms are used for the order-of-accuracy test. The discrete L_2 and L_∞ norms for grid level *k* are given by

$$L_{2,k} = \sqrt{\frac{\sum_{i=1}^{N} |\mathrm{DE}_{k,i}|^2}{N}}, \tag{4.5}$$

$$L_{\infty,k} = \max |\mathrm{DE}_{k,i}|, \tag{4.6}$$

where index i varies over all the grid nodes N in space (including both interior and boundary nodes) with exception of the Dirichlet boundary nodes where the discretization error is identically zero [53].

The observed order-of-accuracy can be adversely affected by computer round-off error and iterative convergence error. Round-off error develops with representation of floating point numbers on the computer and the accuracy at which the numbers are stored.

Iterative convergence error exists because the iterative method used in the simulation must have a stopping point eventually. This latter error scales to the variation in the solution at the completion of the simulations. In order to ensure that these error sources do not pollute the simulation results, both the round-off and iterative convergence errors should be at least 100 times smaller than the discretization error [49, 50]. For all the cases presented herein, double precision computations (64-bit) are used and the root-mean-square change in the iterative convergence error is driven to 10^{-10} by final iteration.

4.2 Method of Manufactured Solutions

A general and very powerful approach to order-of-accuracy test is the Method of Manufactured Solutions (MMS) [47, 48]. Instead of trying to find an exact solution to a system of partial differential equations, the basic idea is to "manufacture" an exact solution *a priori* without being concerned about its physical realism. It is necessary that the solution structure be sufficiently complex to exercise all the terms being tested in the governing equations [54]. The procedure involves operating the governing partial differential equations on the chosen manufactured solution to generate analytical source terms. The manufactured solution becomes the exact solution to the modified governing equations consisting of the original equations and the analytical source terms. These source terms are implemented in the code and the resulting modified equations are then discretized and solved numerically. The numerical solution obtained is then compared to the exact (manufactured) solution [53]. Hence, MMS involves solving the backward problem i.e., given the original governing equations and a chosen solution; find a modified set of equations that the chosen solution will satisfy [49]. The initial and the boundary conditions

are also determined from the manufactured solutions [50]. The method of manufactured solution procedure verifies, though for a narrow range of physical modeling, a large number of numerical aspects in the code, such as the numerical method, differencing technique, spatial transformation technique for grid generation, grid-spacing technique and algorithm coding correctness [55]. Thus, MMS is an interesting blend of glass-box testing and black-box analysis [47, 55].

Order-of-accuracy test is purely a mathematical test to ascertain that the numerical solution truly represents the solution to the continuum governing equations being solved [50]. The manufactured solutions used for this study are chosen with no requirement for physical realism, but the solution structures are sufficiently complex and smooth to exercise all the terms in the governing partial differential equations of interest. In accordance with the code verification test conducted by Roy and co-workers [53], the chosen manufactured solutions employed in this study take the following form:

$$\phi(x,y) = a_0 + a_1\theta_s\left(\frac{b_1\pi x}{L}\right) + a_2\theta_s\left(\frac{b_2\pi y}{L}\right) + a_3\theta_s\left(\frac{b_3\pi xy}{L^2}\right), \tag{4.7}$$

where $\phi = [\rho, u, v, p]^T$ represents any of the primitive variables, $\theta_s(\cdot)$ denotes the sine or cosine functions, L is the domain length, and a_i and b_i are constants. The specific form of the primitive variables for both Euler and Navier-Stokes equations are listed as follows:

$$\rho(x,y) = \rho_0 + \rho_1 \sin\left(\frac{b_1 \pi x}{L}\right) + \rho_2 \cos\left(\frac{b_2 \pi y}{L}\right) + \rho_3 \cos\left(\frac{b_3 \pi xy}{L^2}\right), \quad (4.8)$$

$$u(x,y) = u_0 + u_1 \sin\left(\frac{b_1 \pi x}{L}\right) + u_2 \cos\left(\frac{b_2 \pi y}{L}\right) + u_3 \cos\left(\frac{b_3 \pi xy}{L^2}\right), \quad (4.9)$$

$$v(x,y) = v_0 + v_1 \cos\left(\frac{b_1 \pi x}{L}\right) + v_2 \sin\left(\frac{b_2 \pi y}{L}\right) + v_3 \cos\left(\frac{b_3 \pi xy}{L^2}\right), \quad (4.10)$$

$$p(x,y) = p_0 + p_1 \cos\left(\frac{b_1 \pi x}{L}\right) + p_2 \sin\left(\frac{b_2 \pi y}{L}\right) + p_3 \sin\left(\frac{b_3 \pi xy}{L^2}\right). \quad (4.11)$$

4.3 Order-of-accuracy Results

The order-of-accuracy results for the 2-D Euler and Navier-Stokes equations, spanning both subsonic and supersonic flow regimes, are reported in this section. The test cases are chosen to investigate the effects of both h- and p-refinements, i.e., increasing the number of grids, h, and the order of polynomial, p, of shape function used. For the four test cases examined, the numerical solutions are obtained on the computational domain consisting of uniform Cartesian grids such that: $0 \leq x/L \leq 1$ and $0 \leq y/L \leq 1$ with $L = 1.0$ m. Five different computational grids with grid refinement ratio $r = 2$ are used for the grid convergence test, and the values of p are varied from 1 to 3. The grid sizes are listed in Table 4.1, and the grid spacing (h/h_{min}) is the ratio of element sizes at the *k*th grid level to the finest grid level.

Table 4.2 MMS grid and polynomial order refinements

Grid Level	h-refinements	h/h_{min}	p-refinements
1	129^2	1	1, 2, 3
2	65^2	2	1, 2, 3
3	33^2	4	1, 2, 3
4	17^2	8	1, 2, 3
5	9^2	16	1, 2, 3

4.3.1 Euler Equations

The MMS approach is applied to 2-D, steady-state, compressible Euler equations given by equations (2.1) to (2.3) with the diffusive terms (i.e., viscous stress tensor σ_{ij} and heat flux vector q_i) set to zero and a general source term added to the right-hand side of the equations. These equations constitute the conservation of mass, momentum and energy for an inviscid fluid, coupled with the auxiliary relations stated in equations (2.4) and (2.8). For subsonic and supersonic Euler cases, the exact Dirichlet values are prescribed for all primitive variables at both inflow and outflow boundaries based on the chosen manufactured solutions. The general form of the chosen manufactured solution is given in equation (4.7), while the specific form of the primitive variables for the test cases considered are listed in equations (4.8) to (4.11). The constants used in the simulations of the subsonic and supersonic Euler cases are presented in Tables B.1 and B.2 of Appendix B, respectively. The contour plots of the manufactured solutions for the conserved variables in subsonic Euler case are shown in Figure 4.1.

The Euler equations are applied to the chosen manufactured solutions using a code written in symbolic processing with MATLAB™, which sample script is presented in

Listing 4.1, to generate the analytical source terms that were later converted to a FORTRAN code. The contour plots of the generated source terms for mass, energy, x- and y-momentum equations in the subsonic Euler case are shown in Figure 4.2. These governing equations coupled with the analytical source terms are then discretized and solved numerically. The numerical solutions obtained are compared to the exact (manufactured) solution to determine the discretization error in the solutions. All the solutions presented herein are integrated in time until the L_2 norm of the iterative error approached the iterative convergence tolerance set to $1.0E-10$.

Listing 4.1 MATLAB script used to generate FORTRAN code for the MMS source terms for Euler and Navier-Stokes equations.

```
%  Differentiation of 2D Euler/Navier-Stokes system of equations
clear all
clc

syms  x   y   Rg gam   pii   nu    k     %  nu and k are omitted in Euler case
syms  r0   rx  ry   rxy   arx  ary   arxy
syms  u0  ux  uy  uxy  aux  auy  auxy
syms  v0  vx  vy  vxy  avx  avy  avxy
syms  p0  px  py  pxy  apx  apy  apxy

%  symbolic manipulation of primitive variables & auxiliary equations
r  =  r0+rx*sin (arx*pii*x)+ry*cos (ary*pii*y)+rxy*cos (arxy*pii*x*y);
u  =  u0+ux*sin (aux*pii*x)+uy*cos (auy*pii*y)+uxy*cos (auxy*pii*x*y);
v  =  v0+vx*cos (avx*pii*x)+vy*sin(avy*pii*y)+vxy*cos (avxy*pii*x*y);
p  =  p0+px*cos (apx*pii*x)+py*sin (apy*pii*y)+pxy*sin (apxy*pii*x*y);

t  =   p/(r*Rg);
e  =  (1.0/(gam-1.0))*Rg*t;
et  =  e+(u*u+v*v)/2.0;
tauxx  =  (2.0/3.0)*nu*(2.0*diff (u, x)-diff (v, y));  % omitted in Euler case
tauyy  =  (2.0/3.0)*nu*(2.0*diff (v, y)-diff (u, x));  % omitted in Euler case
tauxy  =  nu*(diff (u, y)+diff (v, x));  % omitted in Euler case
qx  =  -k*diff (t, x);  % omitted in Euler case
qy  =  -k*diff (t, y);  % omitted in Euler case

%  differentiation of source terms
 fm  =   diff (r*u, x)+diff (r*v, y);
 fx  =   diff (r*u*u+p-tauxx, x)+diff (r*u*v-tauxy, y);
 fy  =   diff (r*v*u-tauxy, x)+diff (r*v*v+p-tauyy, y);
 fe  =   diff (r*u*et+p*u-u*tauxx-v*tauxy+qx, x)+
         diff (r*v*et+p*v-u*tauxy-v*tauyy+qy, y);

%  conversion of source terms from MATLAB to FORTRAN code
 fmm =  fortran (fm)
 fxx  =  fortran (fx)
 fyy  =  fortran (fy)
 fee  =  fortran (fe)
```

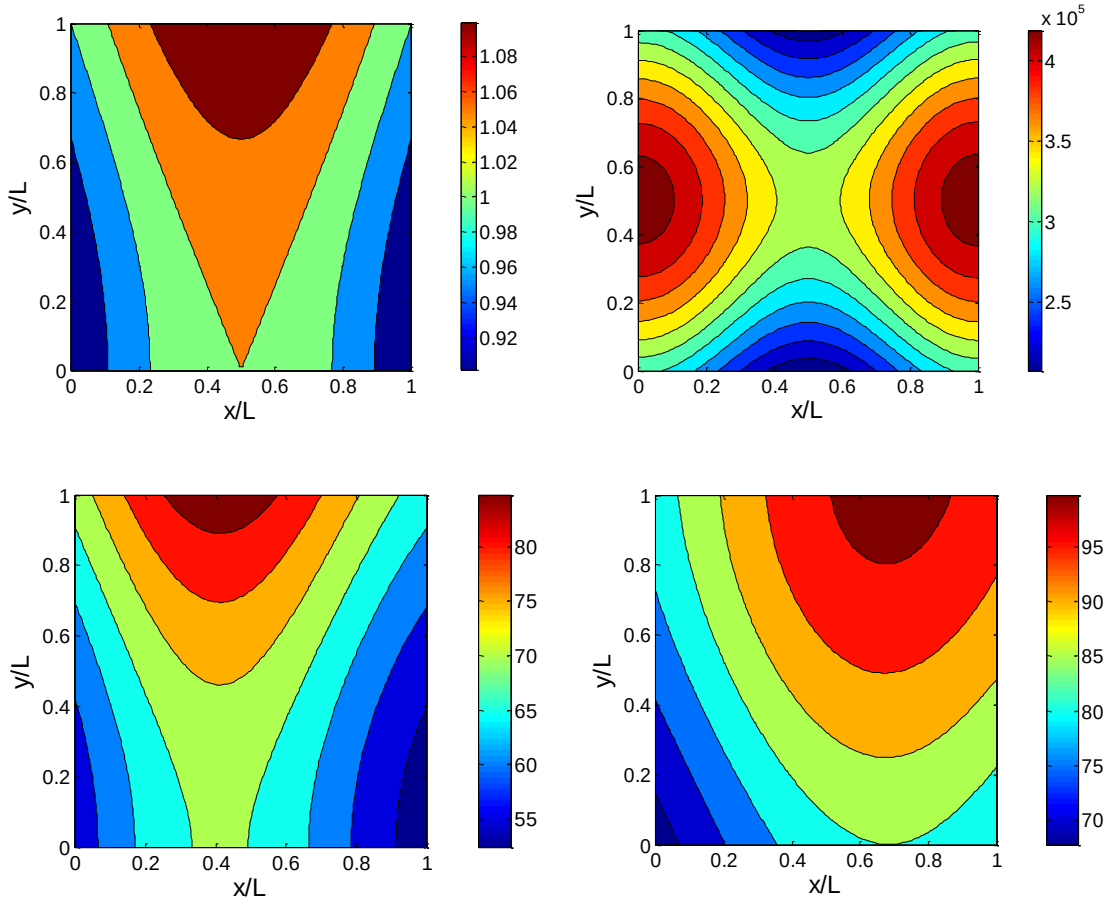

Figure 4.1 Subsonic Euler manufactured solutions for conserved variables:
ρ (top left), ρe_t (top right), ρu (bottom left), ρv (bottom right).

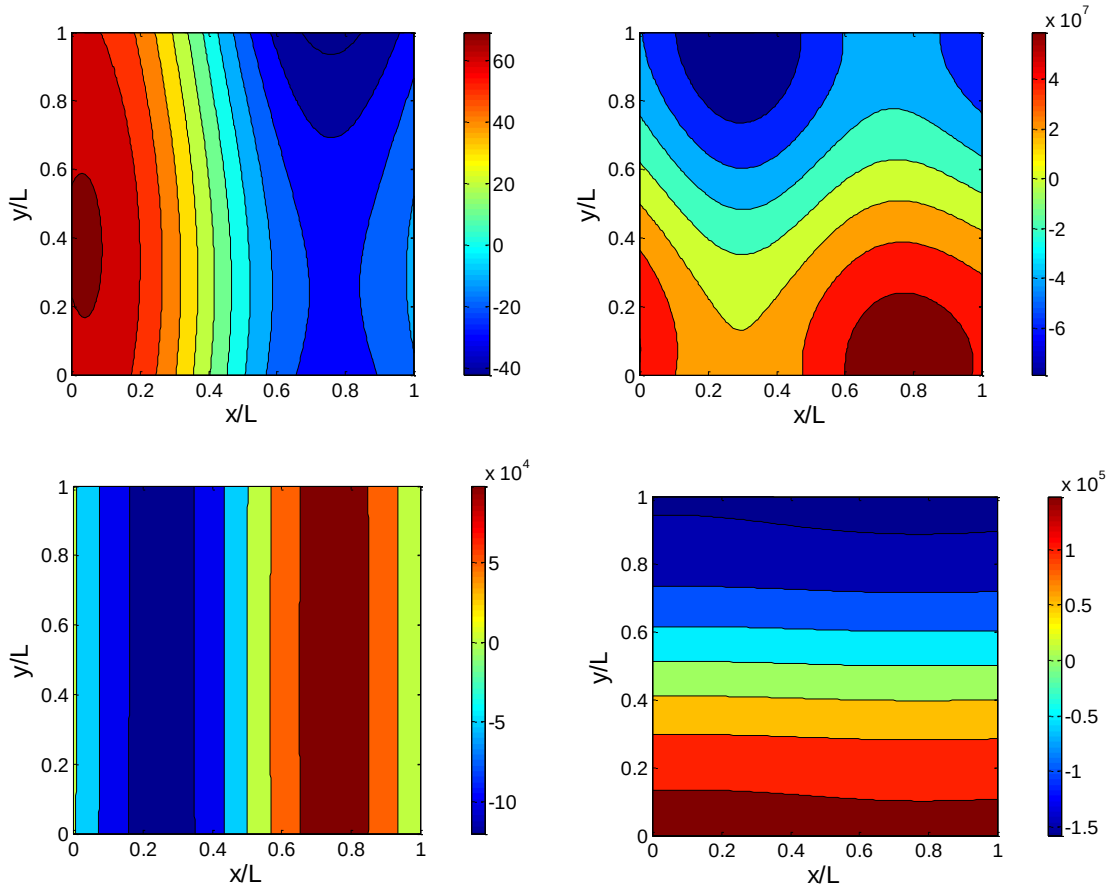

Figure 4.2 Generated source terms for subsonic Euler case: mass (top left), energy (top right), x-momentum (bottom left), y-momentum (bottom right).

For the subsonic Euler case, L_2 and L_∞ norms of the discretization error calculated from equations (4.5) and (4.6) are plotted in Figure 4.3 for $\boldsymbol{x}$-momentum (ρu). The plots show the trends of second-, third- and fourth-order slopes, respectively, for the linear, quadratic and cubic quadrilateral Lagrange elements used for the spatial discretization. Also shown on the figure are the plots of the second-order slope for easy comparison. The computed results from the observed order-of-accuracy expression given in equation (4.4) are plotted in Figure 4.4. These plots show that the formal order-of-accuracy of the numerical method for linear (second-order), quadratic (third-order) and cubic (fourth-order)

quadrilateral Lagrange elements is reproduced with corresponding h- and p-refinements. In fact, the observed order-of-accuracy of the quadratic finite elements appears to be slightly higher than third-order in this case. The observed order-of-accuracy and error norms of the other conserved variables show similar behavior as well.

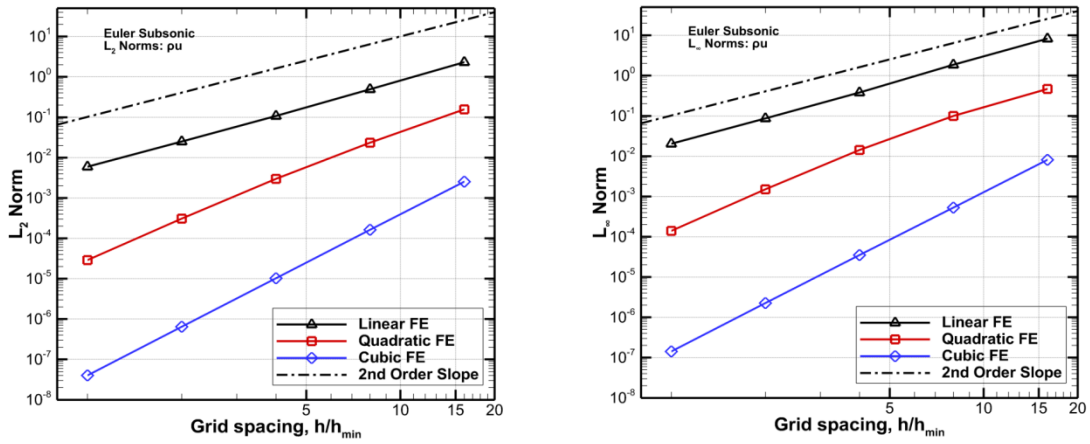

(a) (b)

Figure 4.3 Behavior of x-momentum (ρu) discretization error norms with h- and p-refinements for subsonic Euler case: (a) L_2 norm and (b) L_∞ norm.

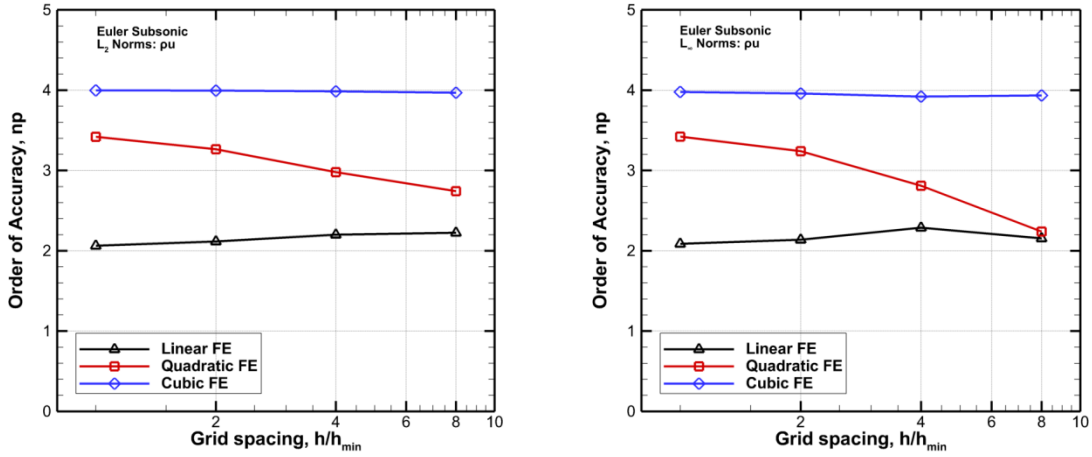

(a) (b)

Figure 4.4 Observed order-of-accuracy of x-momentum (ρu) discretization error norms with h- and p-refinements for subsonic Euler case: (a) L_2 norm and (b) L_∞ norm.

Figure 4.5 shows the behavior of L_2 and L_∞ norms for density (ρ) discretization error in the supersonic Euler case. Again, the plots of the computed error norms asymptotically approach the second-, third- and fourth-order slopes on all grid levels. The plots of the observed order-of-accuracy shown in Figure 4.6 confirm that the code is reproducing the formal spatial order-of-accuracy of the numerical method.

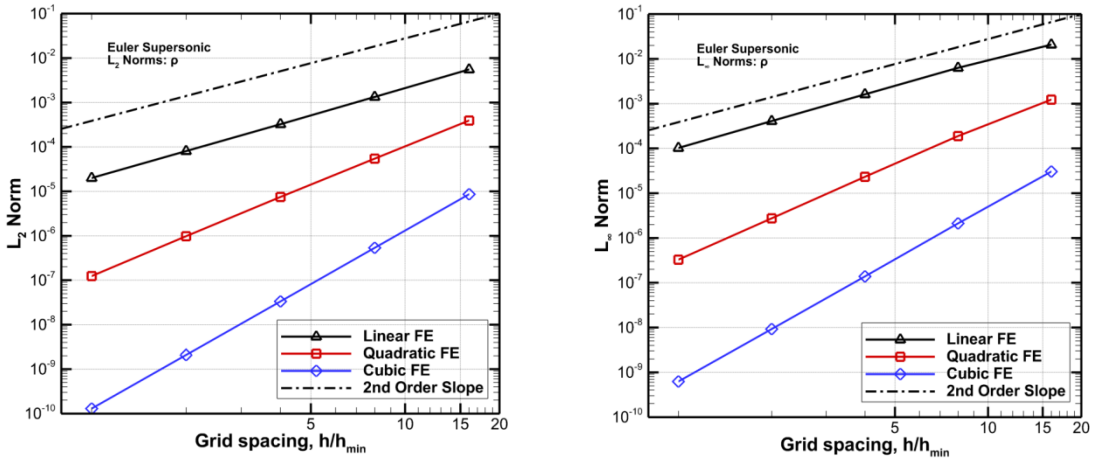

(a) (b)

Figure 4.5 Behavior of density (ρ) discretization error norms with h- and p-refinements for supersonic Euler case: (a) L_2 norm and (b) L_∞ norm.

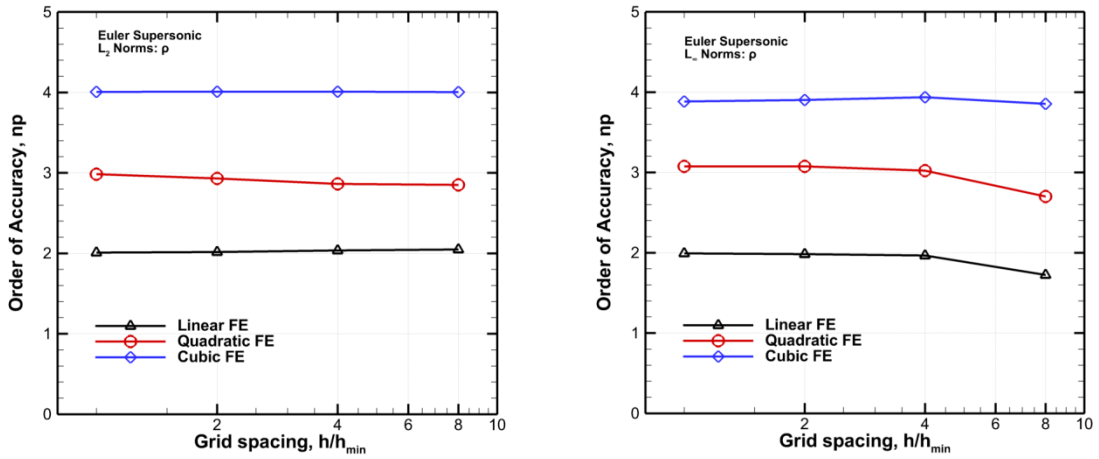

(a) (b)

Figure 4.6 Observed order-of-accuracy of the density (ρ) discretization error norms with h- and p-refinements for supersonic Euler case: a) L_2 norm and b) L_∞ norm.

4.3.2 Navier-Stokes Equations

The MMS approach is also applied to 2-D, steady-state, compressible Navier-Stokes equations given in equations (2.1) to (2.3), with general source terms added at the right-hand side, and coupled with the auxiliary relations given in equations (2.4) to (2.8). For subsonic and supersonic Navier-Stokes cases discussed in this section, the exact Dirichlet values are applied directly to both inflow and outflow boundaries for all primitive variables based on the chosen manufactured solutions. The constants used in the manufactured solutions for the test cases involving subsonic and supersonic flows are tabulated in Tables B.3 and B.4 of Appendix B, respectively.

In the case of supersonic Navier-Stokes calculations, the molecular viscosity is chosen to be $\mu = 20\ \mathrm{Ns/m^2}$ in a bid to ensure that the convective and diffusive terms balance each other. By balancing these two terms appearing in the momentum and energy

equations, the possibility of a "false positive" on the order-of-accuracy test is minimized [54, 55]. The contour plots of the manufactured solutions and the source terms for mass, energy, x- and y-momentum are shown in Figures 4.7 and 4.8, respectively.

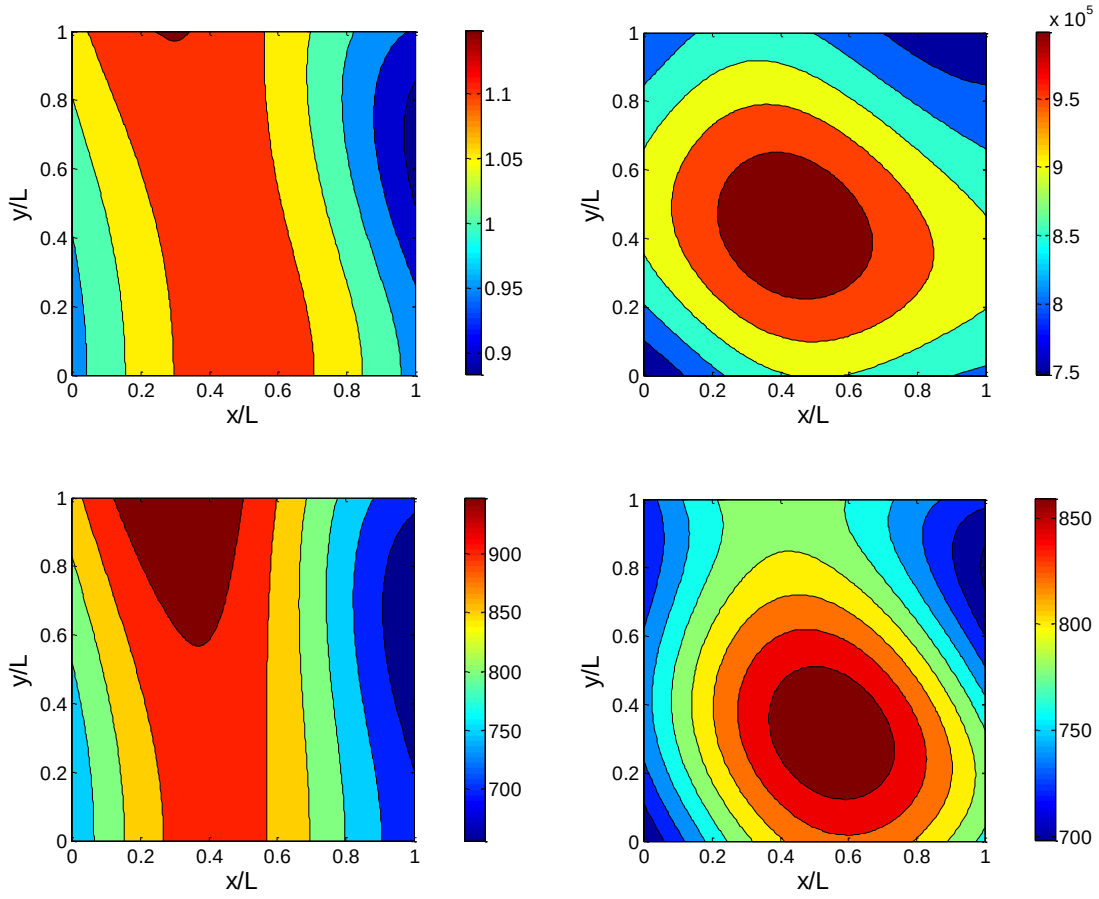

Figure 4.7 Supersonic Navier-Stokes manufactured solutions for conserved variables: ρ (top left), ρe_t (top right), ρu (bottom left), ρv (bottom right).

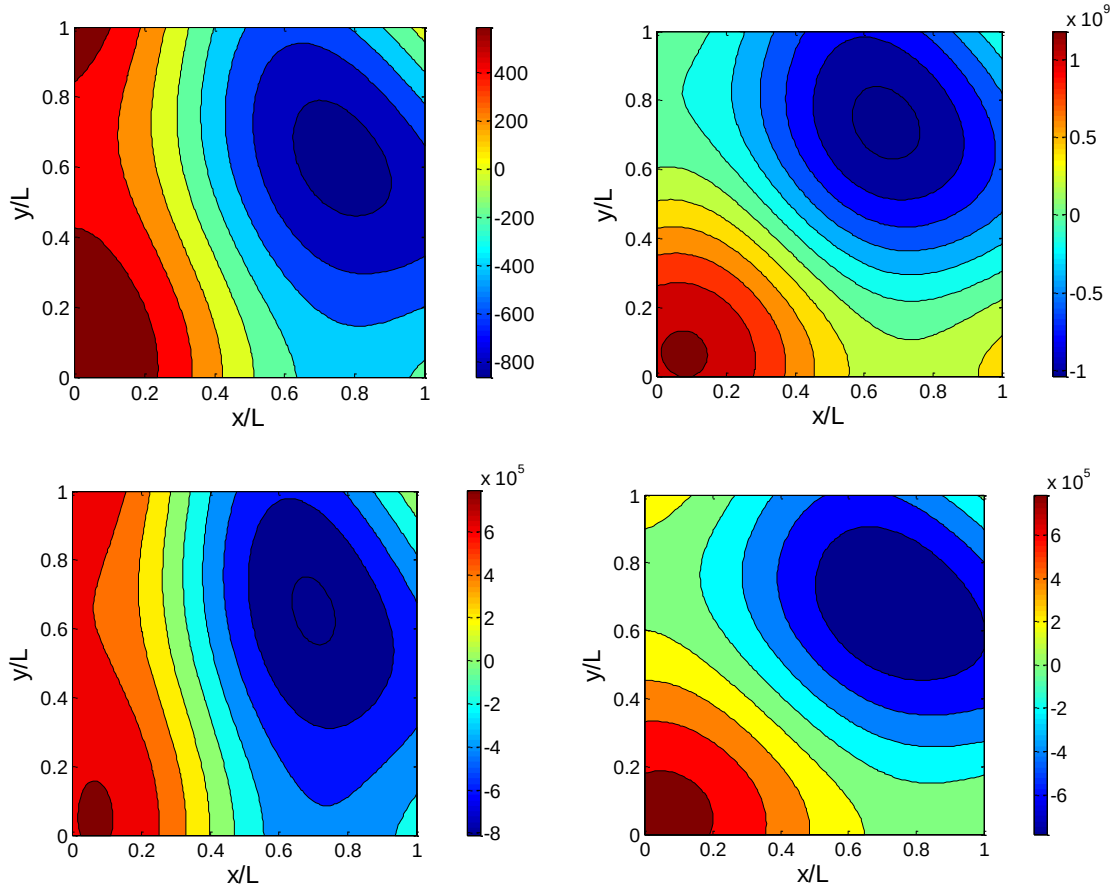

Figure 4.8 Generated source terms for supersonic Navier-Stokes case: mass (top left), energy (top right), x-momentum (bottom left), y-momentum (bottom right).

The behavior of L_2 and L_∞ norms for energy (ρe_t) discretization error in the supersonic Navier-Stokes case is shown in Figure 4.9. These plots show the trends of second-, third- and fourth-order slopes on all grid levels. The observed order-of-accuracy plots are presented in Figure 4.10. The entire plots asymptotically approach the formal order of accuracy for linear, quadratic and cubic quadrilateral Lagrange elements used for the discretization as the grid is refined. Similar behavior is observed for other conserved variables in terms of error norms and observed order-of-accuracy.

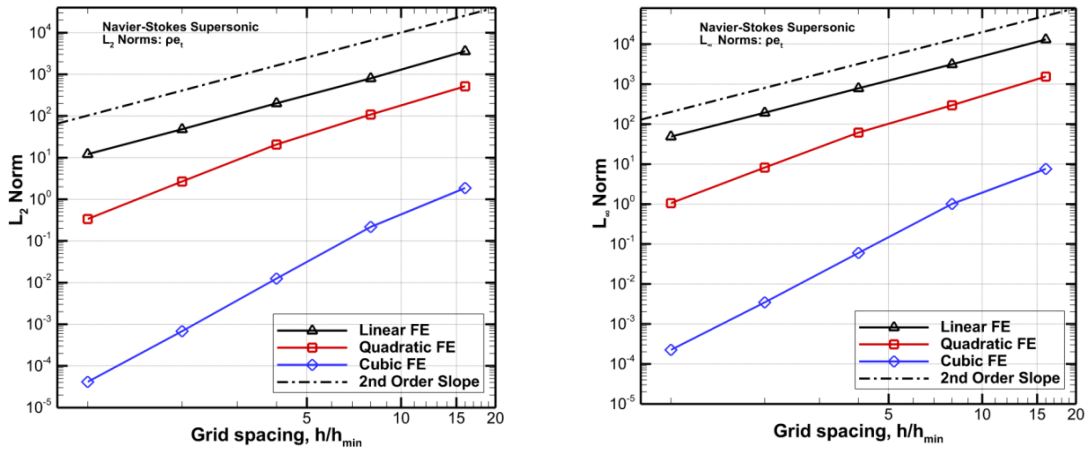

(a) (b)

Figure 4.9 Behavior of energy (ρe_t) discretization error norms with h- and p-refinements for supersonic Navier-Stokes case: (a) L_2 norm and (b) L_∞ norm.

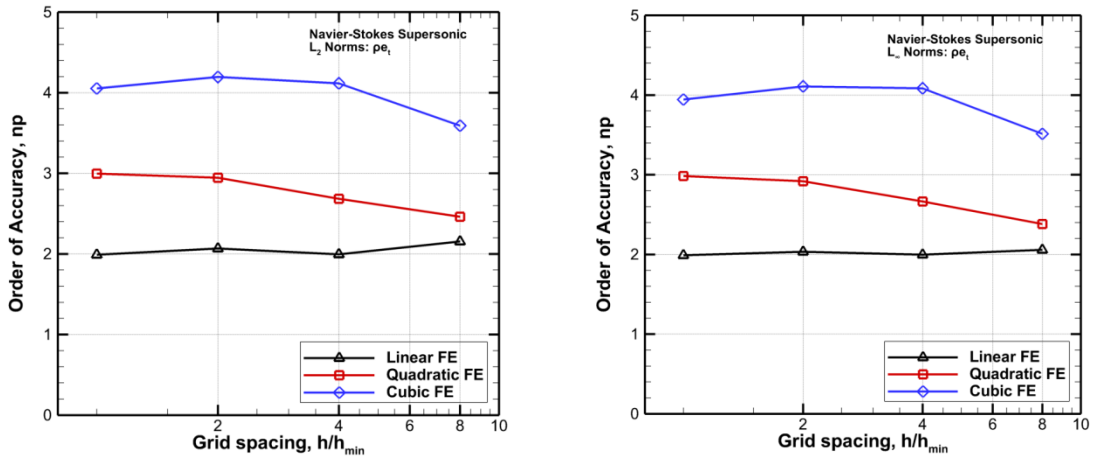

(a) (b)

Figure 4.10 Observed order-of-accuracy of energy (ρe_t) discretization error norms with h- and p-refinements for supersonic Navier-Stokes case: (a) L_2 norm and (b) L_∞ norm.

In the subsonic Navier-Stokes case, the molecular viscosity takes a smaller value of $\mu = 10\ \mathrm{Ns/m^2}$ to ensure that the viscous terms are of the same order of magnitude as the convective terms [53].

The L_2 and L_∞ norms for y-momentum discretization error (ρv) are plottted in Figure 4.11. These plots approach the second-, third- and fourth-order slopes, respectively, for the linear, quadratic and cubic quadrilateral Lagrange elements used for the discretization as the grid is refined.

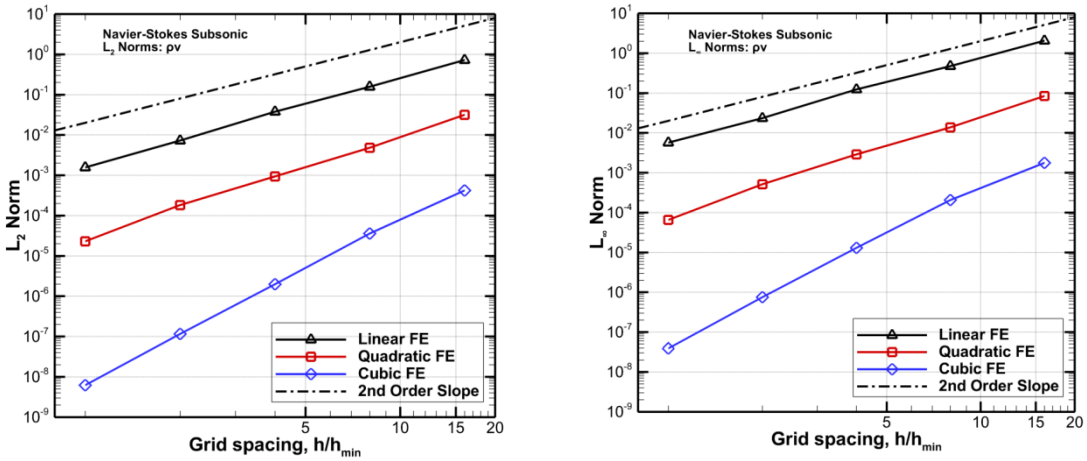

(a) (b)

Figure 4.11 Behavior of y-momentum (ρv) discretization error norms with h-and p-refinements for subsonic Navier-Stokes case: (a) L_2 norm and (b) L_∞ norm.

The spatial convergence of the computed solutions is confirmed by the trends of the observed order-of-accuracy plots shown in Figure 4.12. Other conserved variables show similar behavior of error norms and observed order-of-accuracy as well.

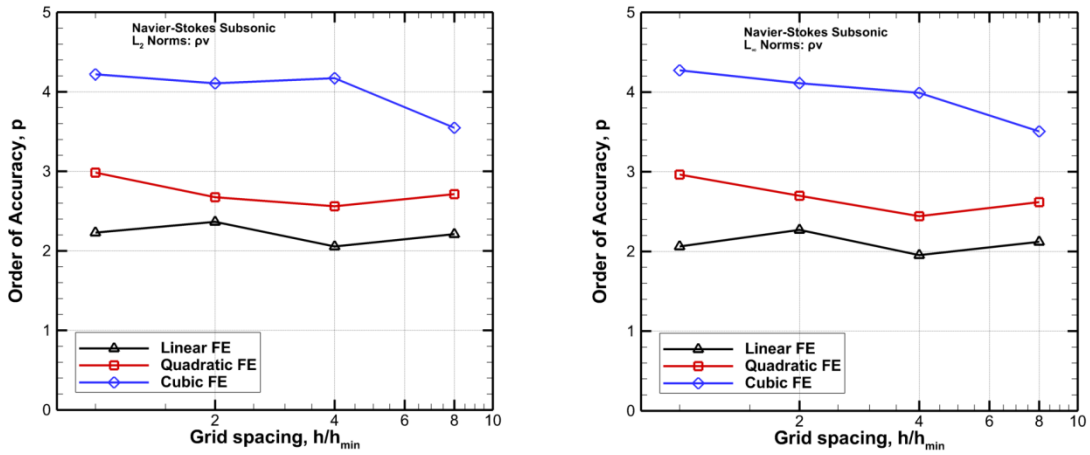

(a) (b)

Figure 4.12 Observed order-of-accuracy of y-momentum (ρv) discretization error norms with h-and p-refinements for subsonic Navier-Stokes case: (a) L_2 norm and (b) L_∞ norm.

In conclusion, the Method of Manufactured Solutions (MMS) has been applied to verify the spatial order-of-accuracy of the FDV method, implemented in a finite element framework, that supports high-order quadrilateral isoparametric Lagrange elements. The order-of-accuracy test was carried out by comparing the numerical solutions to the exact (manufactured) solutions on a series of five consistently-refined grid levels and three order of polynomial of shape functions. Four test cases were investigated; subsonic and supersonic flows governed by the 2-D Euler and Navier-Stokes equations, respectively. In all the test cases considered, the observed order-of-accuracy asymptotically approaches the formal order-of-accuracy with corresponding h- and p-refinements on uniform Cartesian grids. This order-of-accuracy test shows the wider applicability of the MMS in the verification of the theoretical order-of-accuracy of a known high-order CFD method. The procedure provides high level of confidence that there are no coding mistakes in the spatial discretization on uniform Cartesian grids considered. Some of the coding options verified

by the MMS in the current study include: inviscid Euler and viscous Navier-Stokes equations, FDV scheme and the boundary conditions for Dirichlet values in both subsonic and supersonic flow conditions. Options that are not verified include: solver efficiency, numerical stability, arbitrary or curvilinear grids, temporal accuracy, and variable transport properties (i.e., μ and k).

CHAPTER 5

STABILITY AND DISPERSION OF THE FDV METHOD

This chapter details the stability analysis and dispersion errors inherent to the FDV method. Von Neumann or Fourier analysis is conducted to assess FDV numerical stability in Section 5.1. Comparisons of numerical stability and dispersion errors of FDV method to those of Lax-Wendroff scheme (LWS) are presented and discussed in Sections 5.2 and 5.3, respectively.

5.1 Von Neumann Analysis of the FDV Method

In this section, expressions for the amplitude amplification factor, phase angle and relative phase errors of the FDV method are derived starting from one-dimensional (1-D) linear wave advection equation using the second-order accurate central finite difference approximations. These expressions show the connection between the FDV method and Lax-Wendroff Scheme (LWS), and are necessary for comparisons of FDV stability and dispersion errors with those of the LWS.

Applying the FDV method (by replacing the explicit time derivatives with a weighted combination of explicit-implicit time derivatives) to the Taylor expansion series of 1-D wave equation given in equations (3.3) (i.e., $f_t + cf_x = 0$), one obtains

$$f^{n+1} = f^n - \Delta t[(1 - s_a)f_t|^n + s_a f_t|^{n+1}] + \frac{\Delta t^2}{2}[(1 - s_b)f_{tt}|^n + s_b f_{tt}|^{n+1}] + O(\Delta t^3). \quad (5.1)$$

From equation (3.3), $f_t = -cf_x$ and $f_{tt} = c^2 f_{xx}$, using these expressions in equation (5.1) gives

$$f^{n+1} = f^n - c\Delta t[(1-s_a)f_x|^n + s_a f_x|^{n+1}] + c^2\frac{\Delta t^2}{2}[(1-s_b)f_{xx}|^n + s_b f_{xx}|^{n+1}] + O(\Delta t^3). \quad (5.2)$$

In a manner analogous to the LWS scheme, using second-order accurate central finite difference approximations for f_x and f_{xx} yields

$$f_i^{n+1} = f_i^n - \frac{\nu}{2}[(1-s_a)(f_{i+1}^n - f_{i-1}^n) + s_a(f_{i+1}^{n+1} - f_{i-1}^{n+1})] + \frac{\nu^2}{2}[(1-s_b)(f_{i+1}^n - 2f_i^n + f_{i-1}^n) + s_b(f_{i+1}^{n+1} - 2f_i^{n+1} + f_{i-1}^{n+1})], \quad (5.3)$$

where the Courant number $\nu = c\Delta t/\Delta x$, c is the wave speed, Δt is the time step and Δx is the uniform grid size in a finite-differenced spatial discretization. Lax-Wendroff scheme can be obtained from equation (5.3) by setting the implicitness parameters $s_a = s_b = 0$.

Applying the von Neumann stability analysis to equation (5.3) using the appropriate Fourier expression $f_i^n(x,t) = e^{at}e^{ik_m x}$, one obtains

$$\begin{aligned} e^{a(t+\Delta t)}e^{ik_m x} = e^{at}e^{ik_m x} &- \frac{\nu}{2}\left[(1-s_a)\left(e^{at}e^{ik_m(x+\Delta x)} - e^{at}e^{ik_m(x-\Delta x}\right)\right] \\ &+\frac{\nu}{2}\left[s_a\left(e^{a(t+\Delta t)}e^{ik_m(x+\Delta x)} - e^{a(t+\Delta t)}e^{ik_m(x-\Delta x}\right)\right] \\ &+\frac{\nu^2}{2}\left[(1-s_b)\left(e^{at}e^{ik_m(x+\Delta x)} - 2e^{at}e^{ik_m x} + e^{at}e^{ik_m(x-\Delta x}\right)\right] \\ &+\frac{\nu^2}{2}\left[s_b\left(e^{a(t+\Delta t)}e^{ik_m(x+\Delta x)} - 2e^{a(t+\Delta t)}e^{ik_m x} + e^{a(t+\Delta t)}e^{ik_m(x-\Delta x}\right)\right] \end{aligned} \quad (5.4)$$

Dividing equation (5.4) by $e^{at}e^{ik_m x}$ and utilizing the trigonometric relations: $e^{i\beta} + e^{-i\beta} = 2\cos\beta$ and $e^{i\beta} - e^{-i\beta} = i2\sin\beta$, where $\beta = k_m \Delta x$, gives

$$e^{a\Delta t}(1 + \nu^2 s_b(1 - \cos\beta) + i\nu s_a \sin\beta) = 1 - \nu^2(1 - s_b)(1 - \cos\beta) - i\nu(1 - s_a)\sin\beta \tag{5.5}$$

Rearranging equation (5.5) gives the final expression for the amplitude amplification factor of the FDV method, which is expressed as

$$e^{a\Delta t} = \xi_{\text{FDV}} = \frac{1-\nu^2(1-s_b)(1-\cos\beta)-i\nu(1-s_a)\sin\beta}{1+\nu^2 s_b(1-\cos\beta)+i\nu s_a \sin\beta}, \tag{5.6}$$

where ν is the Courant number and β is the frequency parameter.

If the FDV implicitness parameters $s_a = s_b = 0$, one obtains an expression for the amplitude amplification factor for the LWS given by [77]

$$\xi_{\text{LWS}} = 1 - \nu^2(1 - \cos\beta) - i\nu\sin\beta \tag{5.7}$$

The phase angle for the FDV method can be expressed as

$$\Phi_{\text{FDV}} = tan^{-1}\frac{\text{Im}(\xi_{\text{FDV}})}{\text{Re}(\xi_{\text{FDV}})} = \tan^{-1}\left\{\frac{-\nu(1-s_a)\sin\beta}{1-\nu^2(1-s_b)(1-\cos\beta)}\right\}, \tag{5.8}$$

and the relative phase error for the FDV method becomes

$$\frac{\Phi_{\mathrm{FDV}}}{\Phi_{\mathrm{EXACT}}} = \frac{\tan^{-1}\{-\nu(1-s_a)\sin\beta/[1-\nu^2(1-s_b)(1-\cos\beta)]\}}{-\beta\nu}. \tag{5.9}$$

If the FDV implicitness parameters $s_a = s_b = 0$, one obtains an expression for the phase angle for the LWS given by

$$\Phi_{\mathrm{LWS}} = tan^{-1}\frac{\mathrm{Im}(\xi_{\mathrm{LWS}})}{\mathrm{Re}(\xi_{\mathrm{LWS}})} = \tan^{-1}\left\{\frac{-\nu\sin\beta}{1-\nu^2(1-\cos\beta)}\right\}, \tag{5.10}$$

and the relative phase error for the LWS becomes [77]

$$\frac{\Phi_{\mathrm{LWS}}}{\Phi_{\mathrm{EXACT}}} = \frac{\tan^{-1}\{-\nu\sin\beta/[1-\nu^2(1-\cos\beta)]\}}{-\beta\nu}. \tag{5.11}$$

5.2 Numerical Stability of the FDV Method

In this section, the results from the von Neumann stability analysis are reported. Furthermore, the comparative study of the stability conditions of FDV and LWS are presented and analyzed using equations (5.6) and (5.7), respectively.

The stability conditions of FDV and LWS are compared in Figures 5.1 for two values of Courant number $\nu = 1$ and $= 5$. Figure 5.1 shows the plots of the amplitude amplification factor in the complex plane with the imaginary axis flipped. Whenever the amplitude amplification factor ξ exceeds the unit circle, the mode grows and the scheme tends towards an unstable condition. For Courant number $\nu = 1$, LWS (□ ($s_a = 0$, $s_b = 0$) symbol only) is marginally stable, i.e., $\xi_{\mathrm{LWS}} = 1$, but for $\nu = 5$, LWS (□ ($s_a = 0$, $s_b = 0$) symbol with line) is clearly unstable since $\xi_{\mathrm{LWS}} > 1$. This stability behavior of LWS is

well known. The stability of the FDV scheme are influenced by both the Courant number ν, and the implicitness parameters s_a and s_b. This is because s_a and s_b determine the implicitness of the first and second time derivatives in FDV. When $s_a = 0$ and $s_b = 0.5$, FDV has the least implicitness as the first derivative is fully explicit, while the second derivative is Crank-Nicolson-like. As the Courant number ν is increased from 1 to 5, the ξ_{FDV} increases and approaches unity for this semi-implicit scenario. In fact, when $s_a = 0$ and $s_b = 0.5$, $\xi_{FDV} \to 1$ as $\nu \to \infty$, suggesting that FDV is unconditionally stable at all Courant numbers. It is also interesting that ξ_{FDV} does not increase monotonically with ν for the fully-implicit scenario $s_a = s_b = 1$. When $s_a = s_b = 1$, both the derivatives are fully implicit. As expected, for any given Courant number, the FDV scheme is more stable when the implicit parameters $s_a = s_b = 1$.

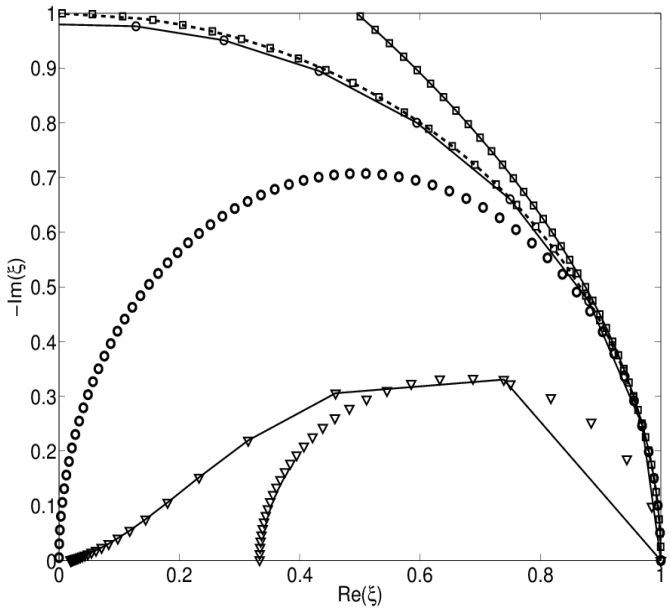

Figure 5.1 Comparison of stability of FDV and LWS. Symbol only (Courant number $\nu = 1$); symbol with line ($\nu = 5$); o ($s_a = 0$, $s_b = 0.5$); ∇ ($s_a = 1$, $s_b = 1$); □ (LWS or $s_a = 0$, $s_b = 0$). Here, ξ is the amplitude amplification factor.

5.3 Dispersion Errors of the FDV Method

In this section, the results from the dispersion error analysis are reported. Furthermore, the comparative study of the dispersion errors of FDV and LWS are presented and analyzed using equations (5.9) and (5.11), respectively.

Figure 5.2 compares the dispersion errors of FDV and LWS using the polar plots of their relative phase errors. If $\Phi/\Phi_{EXACT} > 1$ for a given value of frequency parameter β, the corresponding Fourier component of the numerical solution has a wave speed greater than the exact solution resulting in a leading phase error. Otherwise if $\Phi/\Phi_{EXACT} < 1$, the wave speed of the numerical solution is less than the exact wave speed resulting in a lagging phase error. From Figure 5.2, it can be seen that the LWS has predominantly lagging phase error, which magnitude tends to exceed the unit circle at Courant number is increased from 1 to 5. Hence, LWS is most dispersive at this relatively high Courant number compared to the semi-implicit and fully-implicit scenarios of the FDV scheme. It is interesting to note that the FDV scheme is least dispersive when $s_a = s_b = 1$ for Courant number $\nu = 5$. For this fully-implicit scenario, FDV dispersions errors do not grow monotonically with Courant number.

It can be rightly concluded that the FDV scheme is evidently more stable than the Lax-Wendroff scheme due to its greater implicitness, and is generally less dispersive compared to the Lax-Wendroff scheme.

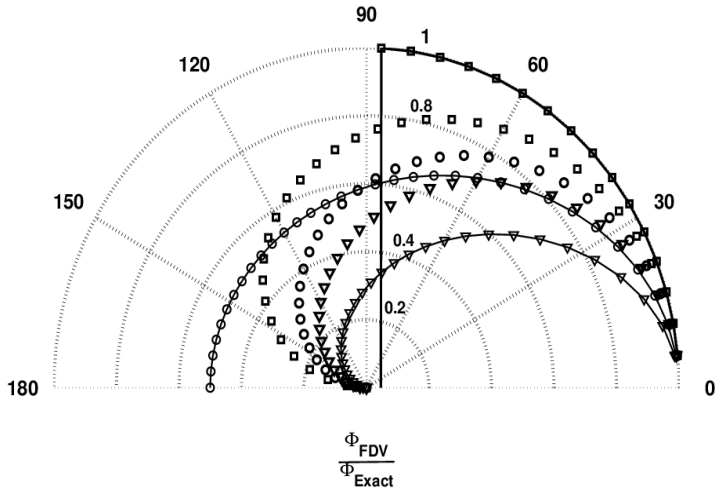

Figure 5.2 Comparison of dispersion errors of FDV and LWS. Symbol only (Courant number $\nu = 1$); symbol with line ($\nu = 5$); o ($s_a = 0$, $s_b = 0.5$); ∇ ($s_a = 1$, $s_b = 1$); □ (LWS or $s_a = 0$, $s_b = 0$). Here, Φ_{FDV}/Φ_{EXACT} is the relative phase error.

CHAPTER 6

NUMERICAL DISSIPATION OF THE FDV METHOD

In general, free-shear flows constitute the benchmark problems for verifying any numerical scheme in turbulent flow computations. Due to the fact that such flows are free from all complexities such as: shock discontinuities, wall effects, and directional inhomogenuity. This chapter presents the quantification of the numerical dissipation inherent to the FDV method. The Euler form of decaying isotropic turbulence is commonly used when one is isolating and quantifying numerical dissipation. The numerical viscosity and dissipation rate inherent to the FDV scheme are quantified and compared with the corresponding quantities from the explicit subgrid-scale (SGS) models. Also presented are comparisons of the FDV numerical and SGS eddy-viscosities with the SUPG numerical viscosity.

The newly-developed LES code, employed for the computations, is an extension of an existing compressible Navier-Stokes solver for performing large-eddy simulations of turbulent flows. The extension entails the implementation of two SGS closures, namely the standard Smagorinsky and dynamic Smagorinsky models, as well as the implicit LES approach based on the intrinsic numerical dissipation of the FDV method.

This chapter is organized as follows. Section 6.1 presents the flow statistics, while the flowfield initial and boundary conditions are briefly discussed in Section 6.2. In Section 6.3, the simulation results from the test cases involving incompressible decaying, inviscid isotropic turbulence, with and without the addition of explicit SGS models, are presented and analyzed.

6.1 Flow Statistics

The test cases involving freely decaying isotropic turbulence are normally initialized with a divergence-free velocity field, which simplifies the calculations of the velocity field statistics. Some important parameters that characterize the decaying isotropic turbulence are briefly defined in this section.

The turbulent fluctuating velocity is defined as

$$u' = (\langle u_i u_i \rangle / 3)^{1/2} , \tag{6.1}$$

where $\langle ... \rangle$ is an instantaneous volume average obtained by integrating over all the elements and the prime superscript denotes root-mean-square quantities.

The transverse Taylor microscale λ and the Taylor microscale Reynolds number Re_λ are defined as

$$\lambda^2 = \frac{3u'^2}{\langle (\partial u_i / \partial x_i)^2 \rangle} , \tag{6.2}$$

$$Re_\lambda = \frac{u' \lambda \langle \rho \rangle}{\langle \mu \rangle} . \tag{6.3}$$

where the longitudinal average gradient squared is averaged over the three spatial directions to improve its statistical estimate.

The turbulent Mach number M_t is given by

$$M_t = \frac{\sqrt{3}u'}{\langle c \rangle}, \tag{6.4}$$

where $\langle c \rangle$ is the mean speed of sound.

The turbulent kinetic energy TKE is defined as

$$\text{TKE} = \frac{3}{2}u'^2. \tag{6.5}$$

Skewness S_3 is a measure of vortex stretching or compression, which provides information on the magnitude of turbulence. Skewness is expressed as

$$S_3 = \frac{\langle (\partial u_1/\partial x_1)^3 \rangle}{\langle (\partial u_1/\partial x_1)^2 \rangle^{3/2}} \tag{6.6}$$

The enstrophy Ω is defined as the rate of dissipation of turbulent kinetic energy and is given by

$$\Omega = \frac{1}{2}\langle \boldsymbol{\omega} \cdot \boldsymbol{\omega} \rangle = \frac{1}{2}\langle |\nabla \times \boldsymbol{u}|^2 \rangle, \tag{6.7}$$

where ω_i is the flow vorticity vector expressed as

$$\omega_i = \epsilon_{ijk} u_{k,j}. \tag{6.8}$$

The Q-criterion used to visualize the coherent turbulent flow structures is given by

$$Q = \frac{1}{2}\left(\tilde{R}_{ij}\tilde{R}_{ij} - \tilde{S}_{ij}\tilde{S}_{ij}\right), \tag{6.9}$$

where $\tilde{S}_{ij}$ is the filtered strain-rate tensor and $\tilde{R}_{ij}$ is the filtered rotational-rate tensor given by

$$\tilde{R}_{ij} = \frac{1}{2}\left(\frac{\partial \tilde{v}_i}{\partial x_j} - \frac{\partial \tilde{v}_j}{\partial x_i}\right). \tag{6.10}$$

6.2 Flowfield Initialization

For all the test cases considered in this chapter, the flow domain is initialized with a random divergence-free velocity field, and constant density and temperature fields. The computational domain is a periodic cubic box of size 2π. The 3-D velocity field is initialized such that it satisfies the kinetic energy spectrum $E(k)$ given by [57]

$$E(k) = Ak^4 \exp\left[-2(k/k_p)^2\right], \tag{6.11}$$

where k is the wavenumber, k_p is the wavenumber at which the energy spectrum peaks $(k_p = 4)$, A is a constant set to obtain a specified initial turbulent Mach number, and the initial energy spectrum is applied within the prescribed wavenumber range $1 \leq k \leq 10$.

6.3 Freely Decaying Inviscid Isotropic Turbulence

For all the simulations reported in this section, it is considered that the Kolmogorov scale is significantly smaller than the grid size; hence the viscous effects are negligible.

Consequently, the Reynolds number, $Re \to \infty$ and the filtered Navier-Stokes equations in equations (3.1) and (3.2) reduce to filtered Euler equations. Therefore, this section presents the results from the simulations of freely decaying isotropic turbulence at zero molecular viscosity. The Euler form of decaying isotropic turbulence is commonly used when one is interested in isolating and quantifying numerical dissipation [42, 58-59]. The numerical viscosity and dissipation rate inherent to the FDV scheme are quantified and compared with the corresponding quantities for the standard Smagorinsky and dynamic Smagorinsky SGS models. Also presented are comparisons of the FDV numerical and SGS eddy-viscosities with the SUPG numerical viscosity.

The initial turbulent Mach number M_{t0} is set to 0.05 for all the cases reported in this section, so that flow may be considered essentially incompressible. A constant time step $\Delta t = 10^{-3}$ is used for the computations. Simulations were performed on three grid resolutions; 32^3, 64^3 and 128^3, and were run up to a normalized time $t^* = 10$, which corresponds to approximately three eddy-turnover times. Here, the normalized time $t^* = t/\tau$ with $\tau = k_0/\varepsilon_0$, where k_0 and ε_0 are turbulent kinetic energy and dissipation rate at the initial conditions, respectively.

Figure 6.1 depicts the *Q*-criterion iso-surfaces colored by vorticity magnitude at two computational times, $t^* = 0$ and $t^* = 1$ for the implicit LES case. The iso-surfaces are for the 128^3 grid with second-order accurate FDV scheme using the linear finite elements. It is evident from Figure 6.1(a) that the initial flowfield is characterized by eddies corresponding to low wavenumber modes. In Figure 6.1(b), the *Q*-criterion iso-surfaces are shown at $t^* = 1$. The multitude of scales, as well as the presence of worm-like vortex structures suggests that the turbulent kinetic energy has cascaded down to the high

wavenumber modes or the small-scale structures. At later computational times ($t^* > 1$), the small-scale vortices dissipate their energy, and in the process coalesce into a fewer number of large structures.

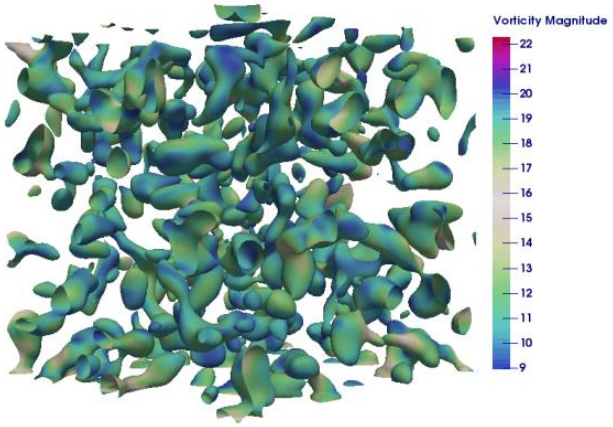

(a) $t^* = 0$

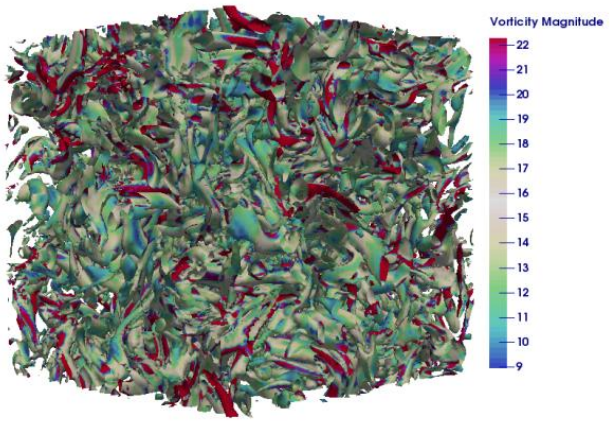

(b) $t^* = 1$

Figure 6.1 *Q*-criterion iso-surfaces colored by vorticity magnitude at different computational times on a 128^3 grid for the ILES case.

6.3.1. Implicit Large-Eddy Simulation Computations

The Implicit Large-Eddy Simulation (ILES) approach involves the use of dissipation inherent to a numerical scheme to mimic the role played by an explicit SGS model. The Euler form of decaying isotropic turbulence is commonly used when one is interested in isolating and quantifying dissipation inherent to the numerical scheme. Thus, the ILES computations are performed to enable the characterization of the intrinsic numerical dissipation of the FDV scheme. In this section, the temporal and spectral statistics of freely decaying inviscid isotropic turbulence obtained from the ILES runs are presented at three different grid resolutions; 32^3, 64^3 and 128^3. Second-order piecewise linear hexahedral elements are used for the spatial discretization (except for high-order accurate simulations), while the time integration is achieved through fully-implicit iterative time-marching procedure based on the Generalized Minimal RESidual (GMRES) algorithm.

Figures 6.2, 6.3, and 6.4 present a comparison of resolved kinetic energy spectra for the ILES case at different computational times on the 32^3, 64^3 and 128^3 grids, respectively. The resolved kinetic energy, initially confined to the prescribed $1 \leq k \leq 10$ wavenumber range, is transferred to higher wavenumbers due to the nonlinear energy cascade process. Ideally, the energy spectrum in the resolved inertial range should have a slope of $-5/3$ on log-log axes as predicted by Kolmogorov for very high Reynolds number flows when the viscous effects are negligible [61]. For all the grid resolutions considered, the energy spectra show reasonable agreement with the $k^{-5/3}$ scaling in the inertial range. Thus, the FDV/ILES framework tends to capture the Kolmogorov scaling; although an under-

dissipative behavior is observed at high wavenumbers close to the cut-off wavenumber $k_c = N/2$. Here, $N/2$ complex Fourier modes are sufficient to describe a real function of one space dimension defined on N grid points. It should be noted that as the grid resolution increases, the cut-off wavenumber increases and the energy build-up close to the cut-off wavenumber reduces. The spectral energy increases with grid resolution at all wavenumbers.

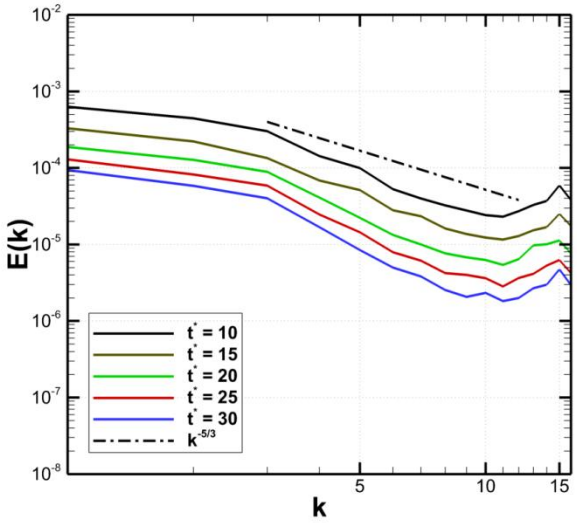

Figure 6.2 Comparison of resolved kinetic energy spectra with the Kolmogorov $-5/3$ power law at different computational times on a 32^3 grid for the ILES case.

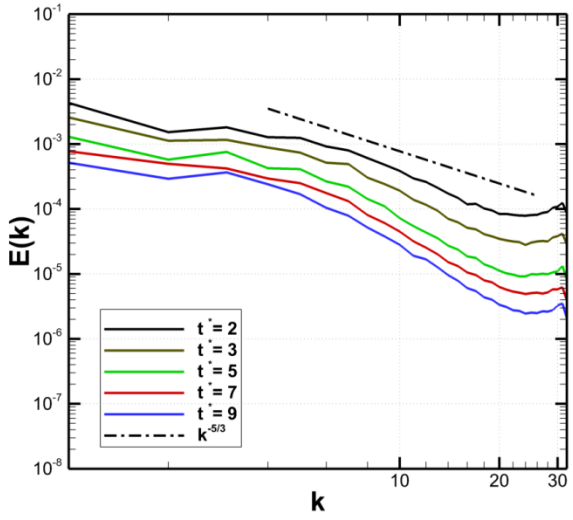

Figure 6.3 Comparison of resolved kinetic energy spectra with the Kolmogorov $-5/3$ power law at different computational times on a 64^3 grid for the ILES case.

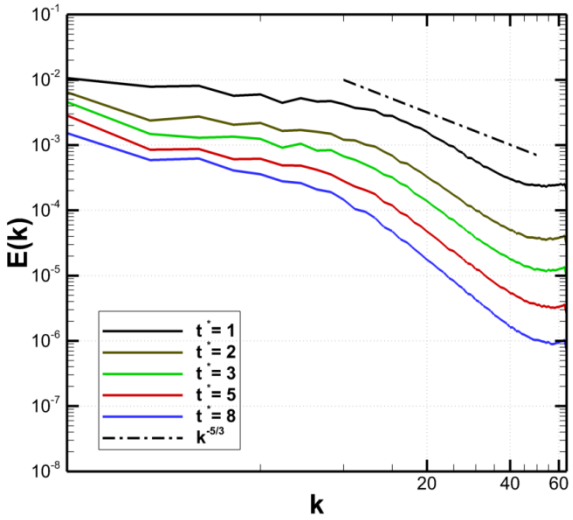

Figure 6.4 Comparison of resolved kinetic energy spectra with the Kolmogorov $-5/3$ power law at different computational times on a 128^3 grid for the ILES case.

Theoretically, the temporal decay rate of kinetic energy scales with time as $t^{*\,-n}$ [16]. In prior studies, decay exponent values ranging between $n = 1.2$ and $n = 1.43$ were reported [62-64]. Figure 6.5 shows the time history of resolved kinetic energy on the 32^3,

64^3 and 128^3 grids. During the initial transient stage, the kinetic energy is being transferred from low to high wavenumbers. Once the high wavenumbers are populated, the numerical dissipation increases until the values of the kinetic-energy decay exponents ranging between $n = 1.40$ (for 32^3 grid) and $n = 1.43$ (for 128^3 grid) are attained. Thus, the FDV/ILES framework is able to capture the $t^{*-1.43}$ kinetic-energy decay rate as predicted by Kolmogorov for inviscid isotropic turbulence [64], especially at the higher grid resolution of 128^3.

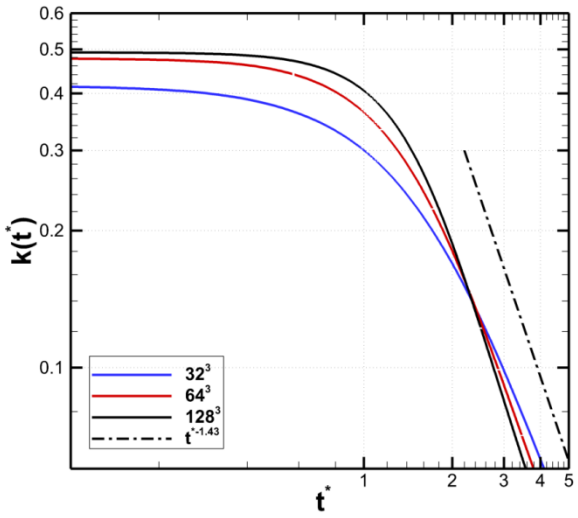

Figure 6.5 Time history of resolved kinetic energy at different grid resolutions for the ILES case. The Kolmogorov's $t^{*-1.43}$ kinetic-energy decay law is also indicated.

Figure 6.6 shows the time history of enstrophy on the 32^3, 64^3 and 128^3 grids. At $t^* > 0.1$, the enstrophy increases with time due to vortex stretching that transfers energy to the smaller vortices with higher velocity gradients. As the turbulent flowfield becomes fully developed, the enstrophy reaches its peak around time $t^* = 1.4$. Subsequently, enstrophy undergoes a monotonic decay with time, as numerical damping becomes significant enough to reduce the turbulent kinetic energy. It can be seen that increasing the

grid resolution leads to higher enstrophy peaks, indicating a decrease in numerical dissipation with an increase in grid resolution.

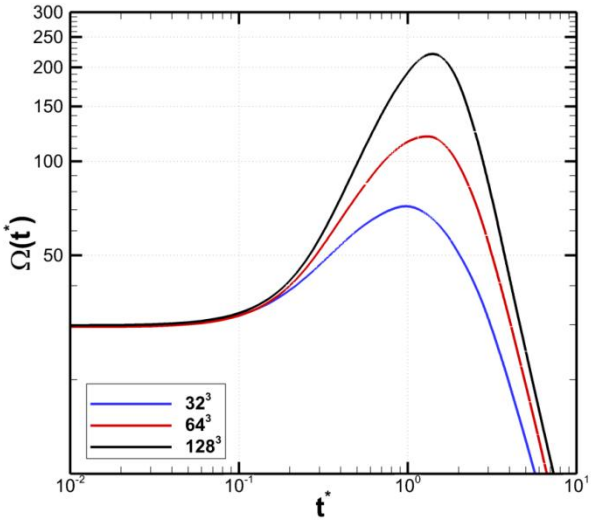

Figure 6.6 Time history of enstrophy at different grid resolutions for the ILES case.

Figures 6.7 and 6.8 present the time histories of resolved kinetic energy and enstrophy, respectively, on a 32^3 grid for the linear, quadratic and cubic shape functions. The plots correspond to the FDV/ILES case with no explicit SGS model. Figure 6.7 shows that the second-order accurate method, with linear finite elements, exhibits the highest kinetic-energy decay rate. This is followed by the third-order and fourth-order accurate methods, involving quadratic and cubic finite elements, respectively. The kinetic-energy decay exponents lie between $n = 1.40$ and $n = 1.41$ for all three polynomial orders, which is in good agreement with theoretical range published in Lesieur [65]. However, the best agreement is obtained for the cubic shape functions as shown in Figure 6.7. The enstrophy profiles of Figure 6.8 reveal that the higher the order of accuracy, the higher the enstrophy

peak. This trend indicates that the fourth-order accurate method is the least dissipative, followed by the third- and the second-order accurate methods.

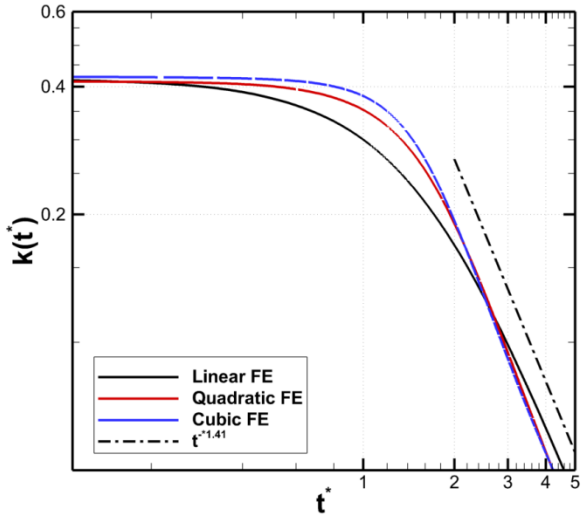

Figure 6.7 Effects of spatial order-of-accuracy on the temporal decay of resolved kinetic energy on a 32^3 grid for the ILES case. The $t^{*-1.41}$ kinetic-energy decay rate is also indicated.

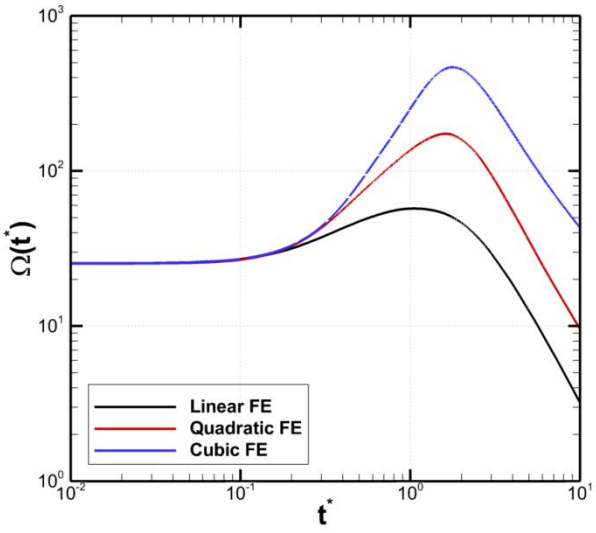

Figure 6.8 Effects of spatial order-of-accuracy on the temporal profiles of enstrophy on a 32^3 grid for the ILES case.

Figure 6.9 shows a comparison of the temporal profiles of enstrophy on different grid resolutions and spatial order-of-accuracy for the ILES case. The effect of higher order elements' modes is evident, where the simulation with quadratic elements (i.e., third-order accurate method) on a coarser 32^3 grid tends to exhibit modes and wavenumber span comparably closer to that obtained using linear elements (i.e., second-order accurate method) on a finer 128^3 grid. The relatively lower peak of the 32^3 quadratic elements' enstrophy profile confirms the fact that a lesser numerical dissipation is supplied by the FDV scheme when a higher-order accurate method is employed. Hence, simulations involving high-order accurate FDV scheme seems to provide grid compression, resulting in substantial savings in both computational time and memory requirement.

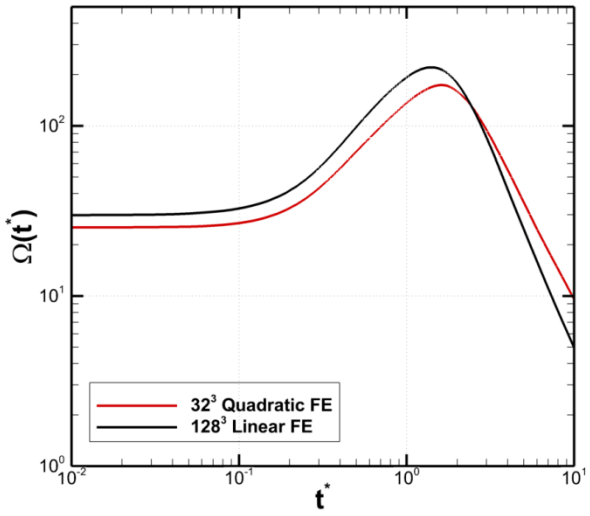

Figure 6.9 Effects of grid resolution and spatial order-of-accuracy on the temporal profiles of enstrophy for the ILES case.

Figure 6.10 shows a comparison of the temporal evolution of FDV numerical viscosity, calculated from equation (3.46), for the three different grid resolutions. During early computational times ($t^* < 0.9$), the numerical viscosity remains essentially constant,

indicating that the initial flowfield is dominated by vortices of low wavenumber modes. This suggests that the turbulent energy cascade has not yet developed so as to cause energy dissipation at high wavenumbers. Once the turbulent flowfield is fully developed and the higher wavenumber modes of the energy spectrum are populated for time $t^* > 1.0$, the magnitude of numerical viscosity decreases monotonically with time due to the dissipation of kinetic energy.

In Figure 6.11, the time history of numerical dissipation rate is shown for three different grid resolutions. Initially, the numerical dissipation rate increases with time, but only gradually, until it reaches a peak value around time $t^* \approx 0.9$. Subsequently, the dissipation rate decays monotonically due to the non-linear energy cascade process. Furthermore, Figures 6.10 and 6.11 show that as the grid is refined, the magnitudes of both numerical viscosity and dissipation rate decrease, as expected. At the grid resolution of 128^3, the numerical dissipation shows a prominent peak around $t^* \approx 1.0$, which is also the time at which enstrophy attains its peak in Figure 6.6.

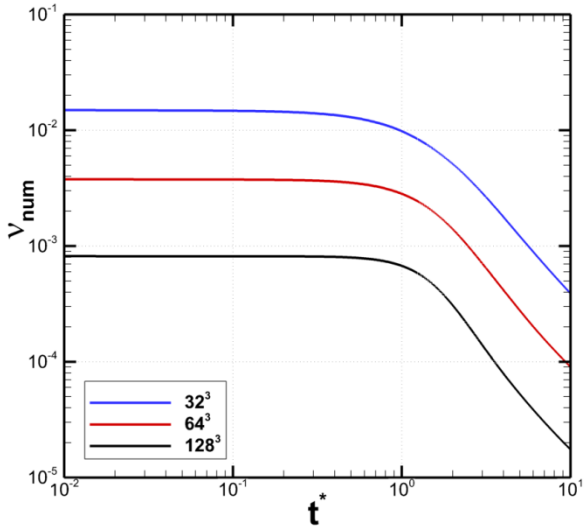

Figure 6.10 Effects of grid resolution on the temporal profiles of numerical viscosity inherent to the FDV/ILES case.

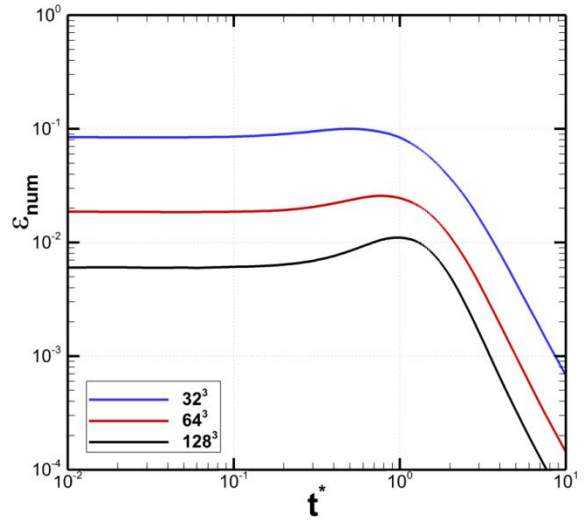

Figure 6.11 Effects of grid resolution on the temporal profiles of numerical dissipation rate inherent to the FDV/ILES case.

6.3.2. Computations with Subgrid-scale Closures

The discussion in Section 6.3.1 indicates that the FDV scheme provides adequate numerical dissipation to maintain stability when performing ILES of isotropic turbulence. The results obtained from large-eddy simulations with the inclusion of an explicit SGS model are presented in this section. Two SGS models, standard Smagorinsky and dynamic Smagorinsky, are considered. The Smagorinsky constant $C_s = 0.18$, which corresponds to its theoretical value for decaying, inviscid isotropic turbulence [51] and the turbulent Prandtl number $Pr_t = 0.6$.

Figures 6.12 and 6.13 present the time histories of resolved kinetic energy and enstrophy on a 32^3 grid. These figures show that the Smagorinsky model is the most dissipative, as reflected in the lowest magnitudes of both turbulent kinetic energy and enstrophy. In general, the dynamic Smagorinsky model is marginally less dissipative than the two other closures. It should be noted that the log-log plots in Figures 6.12 and 6.13 have been magnified in vertical axis to show the differences between the three LES closures. Figure 6.14 presents the energy spectra at time $t^* = 10$ for the three LES closures on the 32^3 grid. This figure shows that the Smagorinsky model is the most dissipative among the three closures, due to the lowest $E(k)$ plotted for this model. The dynamic Smagorinsky model tends to better capture the energy spectrum by accounting for the energy transfers within the inertial subrange through a more accurate estimation of turbulent eddy-viscosity. One also notices that for the 32^3 grid, all three closures are under-dissipative at wavenumbers close to the cut-off wavenumber.

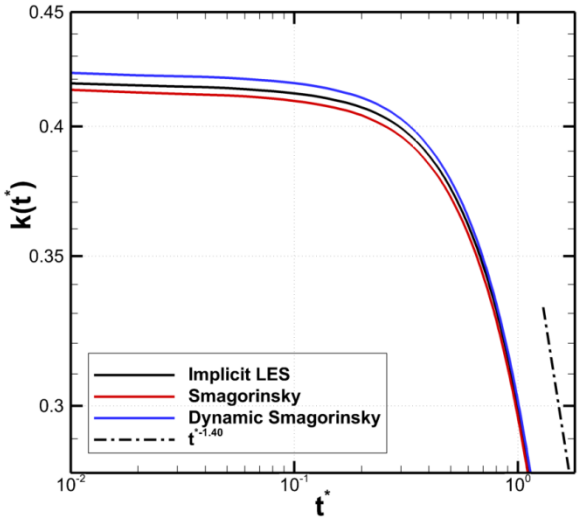

Figure 6.12 Comparison of time histories of resolved kinetic energy on a 32^3 grid for the three LES cases. The $t^{*-1.40}$ kinetic-energy decay rate is also indicated.

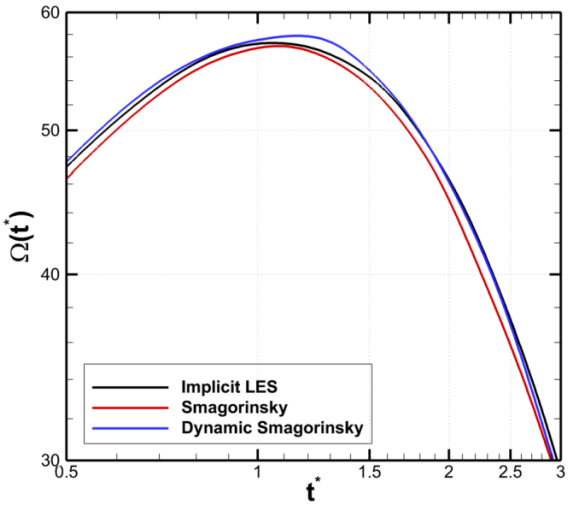

Figure 6.13 Comparison of time histories of enstrophy on a 32^3 grid for the three LES cases.

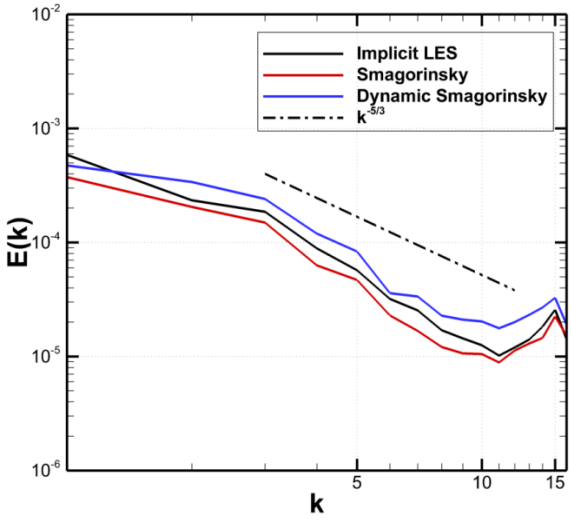

Figure 6.14 Comparison of energy spectra at time $t^* = 10$ on a 32^3 grid for the three LES cases.

Figures 6.15 and 6.16 present the time histories of resolved kinetic energy and enstrophy, respectively, on the 64^3grid for the three LES cases. The results for the 64^3 grid show similar trends as those for the 32^3 grid. In Figure 6.15, all the three LES cases show the $t^{*-1.40}$ kinetic-energy decay rate in the fully developed turbulence regime. It is evident from both kinetic energy and enstrophy plots that in the developed turbulence regime, all the three LES closures show similar dissipative behavior, although the standard Smagorinsky model case is marginally more dissipative that the others. In Figure 6.16, energy spectra at time $t^* = 7$ on the 64^3 grid are shown. When compared to the corresponding spectra for the 32^3 grid, these spectra show improved agreement with the Kolmogorov's $k^{-5/3}$ scaling within the inertial subrange. However, the smallest resolved scales still suffer from low numerical damping.

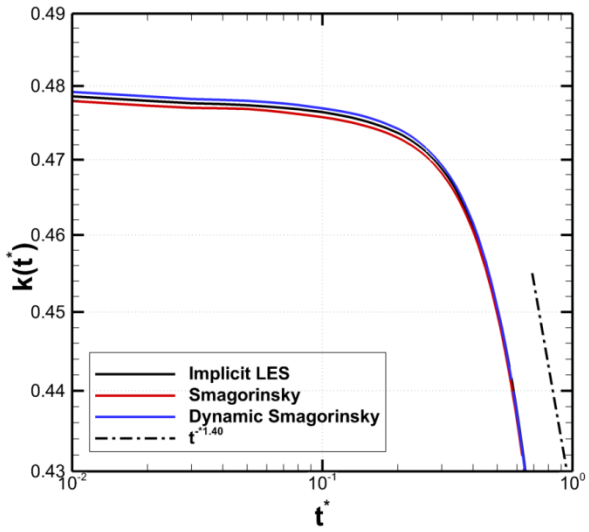

Figure 6.15 Comparison of time histories of resolved kinetic energy on a 64^3 grid for the three LES cases. The $t^{*-1.40}$ kinetic-energy decay rate is also indicated.

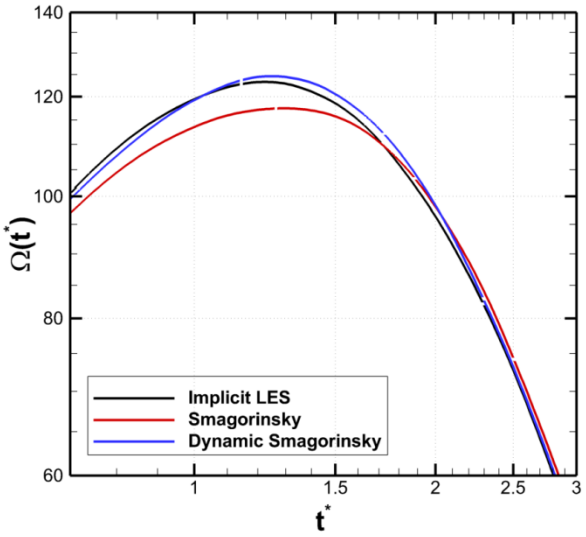

Figure 6.16 Comparison of time histories of enstrophy on a 64^3 grid for the three LES cases.

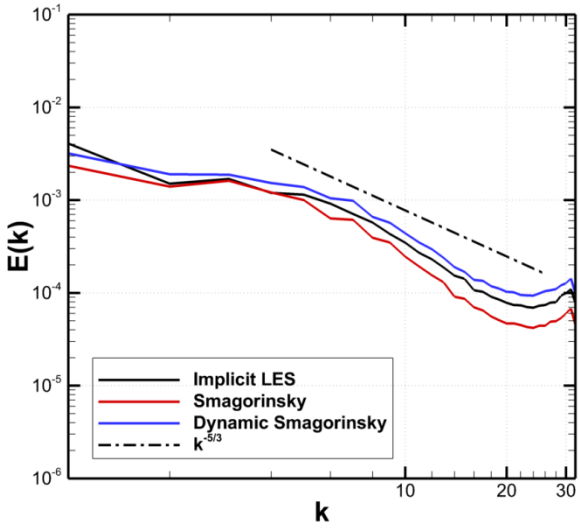

Figure 6.17 Comparison of energy spectra at time $t^* = 7$ on a 64^3 grid for the three LES cases.

Figures 6.18 and 6.19 present the time histories of resolved kinetic energy and enstrophy on the 128^3 grid. Trends similar to those seen for 32^3 and 64^3 grids are observed. In the developed turbulence regime, the $t^{*-1.43}$ kinetic-energy decay rate is recovered for the three LES cases, as shown in Figure 6.18. The plots of enstrophy in Figure 6.19 are consistent with the previous results, with the Smagorinsky model showing slightly greater dissipation than the others. The energy spectra at time $t^* = 5$ on the 128^3 grid are shown in Figure 6.20. It is evident that the Kolmogorov's $k^{-5/3}$ law in the inertial subrange is better recovered than for the two coarser grids.

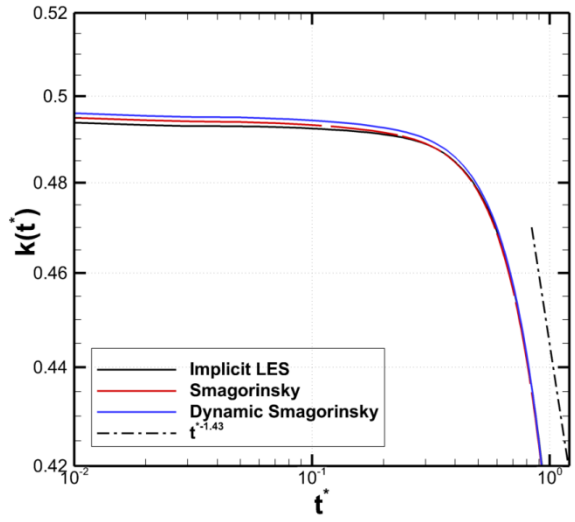

Figure 6.18 Comparison of time histories of resolved kinetic energy on a 128^3 grid for the three LES cases. The Kolmogorov's $t^{*-1.43}$ kinetic-energy decay rate is also indicated.

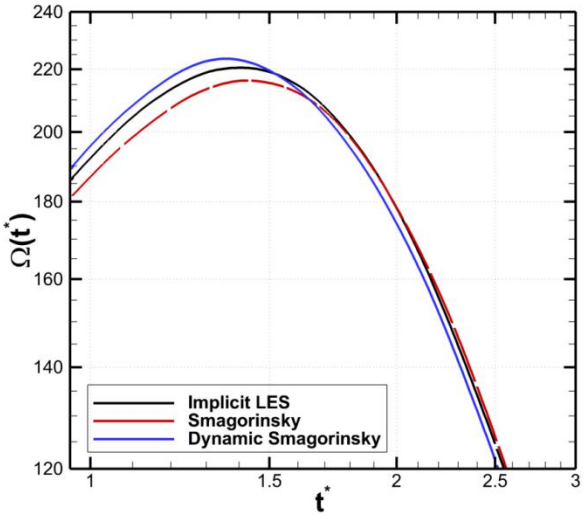

Figure 6.19 Comparison of time histories of enstrophy on a 128^3 grid for the three LES cases.

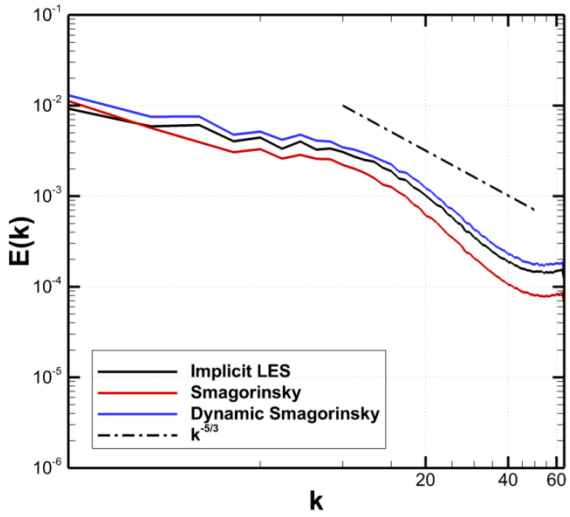

Figure 6.20 Comparison of energy spectra at time $t^* = 5$ f on a 128^3 grid for the three LES cases.

Figure 6.21 compares the temporal profile of numerical viscosity in the FDV/ILES simulation with the temporal profiles of eddy-viscosities in the standard Smagorinsky and dynamic Smagorinsky LES simulations on the 32^3 grid. The corresponding comparisons for the 64^3 and 128^3 grids are shown in Figures 6.22 and 6.23, respectively. Also shown in the figures is the numerical viscosity inherent to the SUPG finite element method for a finite number of flow realizations. It is to be noted that the SUPG numerical viscosity is computed using the FDV/ILES flowfield at the instances indicated in the figures. This approach facilitates a direct comparison of the numerical viscosities due to FDV and SUPG computed using equations (3.46) and (3.49), respectively.

Figure 6.21 shows that up to time $t^* < 0.2$, the numerical viscosity for FDV/ILES has a marginally higher magnitude than the viscosities for the two SGS cases. The slightly higher FDV viscosity is not a significant trend, since for $t^* < 0.2$ the turbulence has not yet fully developed. The two SGS viscosities increase marginally during the time period

$0.1 < t^* < 2.0$, but decrease monotonically with time subsequently. Additionally, for $t^* < 0.2$, the ILES, LES and SUPG viscosities remain nearly constant, suggesting that the turbulence has not yet attained a fully developed state characterized by non-linear energy cascade process. An important observation in Figure 6.21 is that the SUPG numerical viscosity is consistently higher than the other three viscosities. In fact, the SUPG viscosity is nearly an order of magnitude greater than the FDV viscosity at all the flow realizations shown. Similar trends are observed for 64^3 and 128^3 grids shown in Figures 6.22 and 6.23, respectively. It can be seen from Figures 6.21-6.23 that the viscosity magnitudes show an overall decrease with an increase in grid resolution. Further, grid refinement delays the time at which SGS viscosity profiles peak. For the three grids, the FDV/ILES viscosity is the lowest in the fully developed turbulence regime.

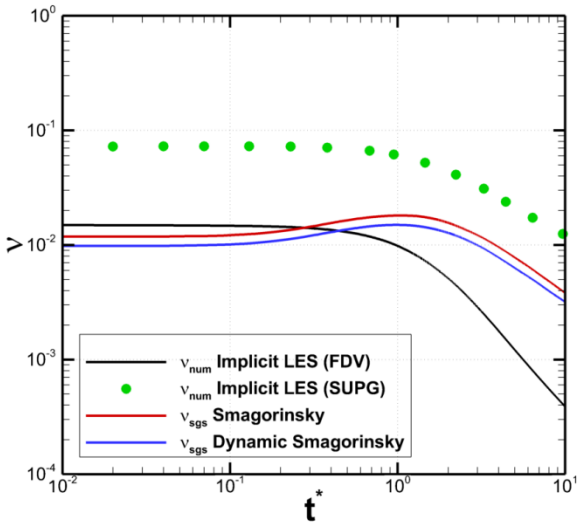

Figure 6.21 Comparison of temporal profiles of the FDV numerical viscosity, eddy viscosities of the two SGS/LES cases, and SUPG numerical viscosity on a 32^3grid.

.

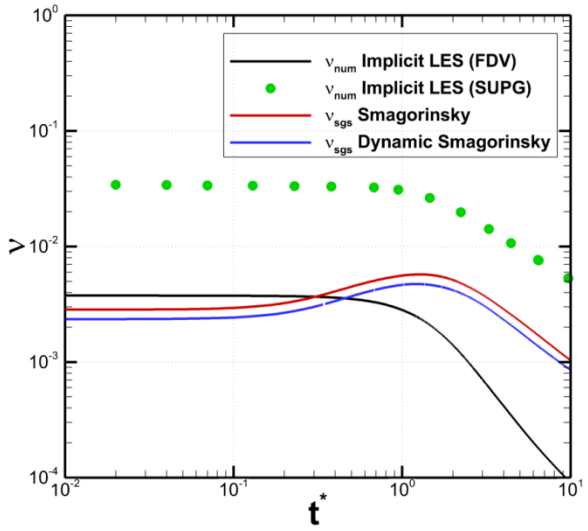

Figure 6.22 Comparison of temporal profiles of the FDV numerical viscosity, eddy viscosities of the two SGS/LES cases, and SUPG numerical viscosity on a 64^3grid.

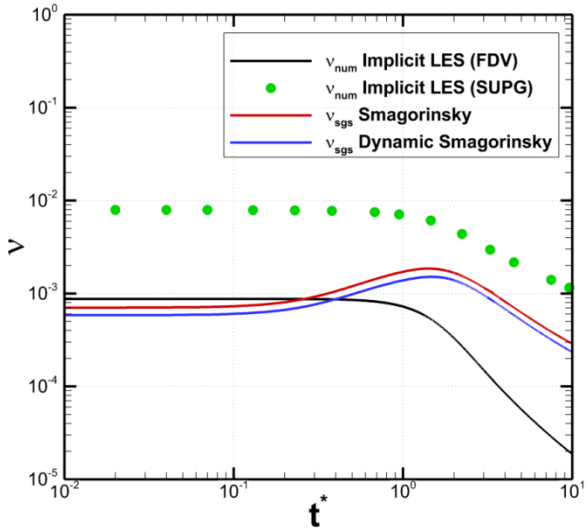

Figure 6.23 Comparison of temporal profiles of the FDV numerical viscosity, eddy viscosities of the two SGS/LES cases, and SUPG numerical viscosity on a 128^3grid.

Figures 6.24 shows a comparison of the time history of dissipation rates in the FDV/ILES and the two SGS/LES simulations on the 32^3grid. These comparisons on the 64^3 and 128^3 grids are shown in Figures 6.25 and 6.26, respectively. Figure 6.24 shows that

during initial times, the dissipation rates for all three cases are essentially constant. Subsequently for ($t^* > 0.2$), they undergo a marginal increase in time up to $t^* = 1$. At later computational times, the dissipation rates decay monotonically. The numerical dissipation rate in the FDV/ILES simulation has the marginally higher magnitude during the early stages, but undergoes a steeper decay at later computational times. Similar trends are observed for the 64^3 and 128^3 grids shown in Figures 6.25 and 6.26, except that the magnitudes of dissipation rates decrease as the grid is refined.

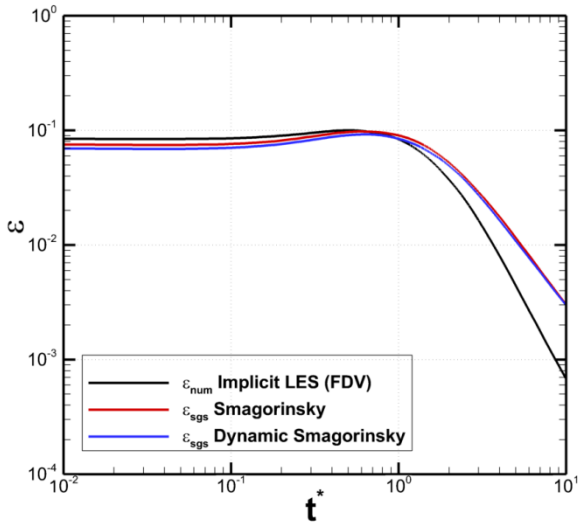

Figure 6.24 Comparison of temporal profiles of dissipation rates of the FDV/ILES case and the two SGS/LES cases on a 32^3 grid.

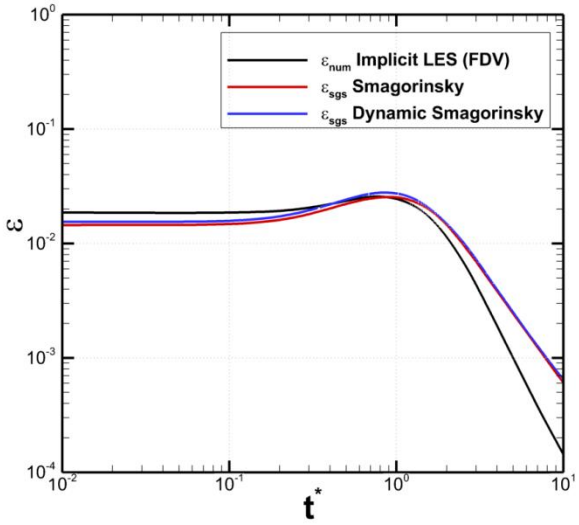

Figure 6.25 Comparison of temporal profiles of dissipation rates of the FDV/ILES case and the two SGS/LES cases on a 64^3 grid.

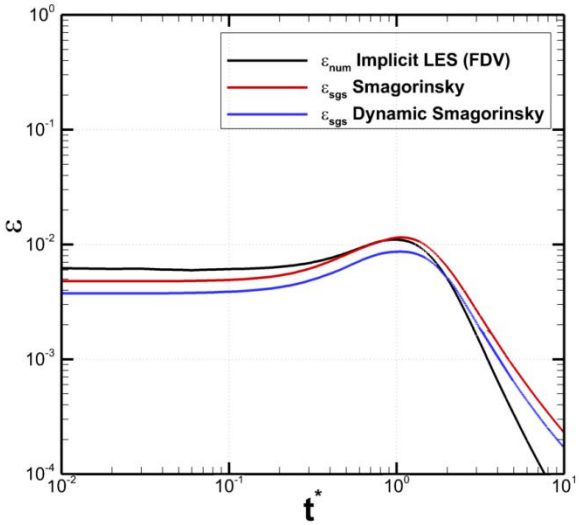

Figure 6.26 Comparison of temporal profiles of dissipation rates of the FDV/ILES case and the two SGS/LES cases on a 128^3 grid.

The effects of interactions between the FDV scheme and an explicit SGS model can be further assessed by monitoring the effective viscosity, which is defined as the equivalent

viscosity representing the energy cascade from the kth wavenumber mode and the modes located beyond the cut-off wavenumber k_c [60].

The effective numerical viscosity in the FDV/ILES simulation and the effective SGS eddy-viscosity for the two SGS/LES cases can be evaluated using the expressions given below [31, 66]:

$$\nu_{\text{eff}}^{\text{num}}(k) = \frac{\varepsilon_{\text{num}}(k)}{2k^2E(k)}, \tag{6.12}$$

$$\nu_{\text{eff}}^{\text{sgs}}(k) = \frac{\varepsilon_{\text{sgs}(k)}}{2k^2E(k)}, \tag{6.13}$$

$$\widehat{\nu}_{\text{SUPG}}(k) = \sqrt{\sum_{|\boldsymbol{k}'|=k} \widehat{\nu}_{\text{SUPG}}(k',t)\widehat{\nu}^*_{\text{SUPG}}(k',t)}\,, \tag{6.14}$$

where $\varepsilon_{\text{num}}(k)$ and $\varepsilon_{\text{sgs}}(k)$ are the numerical and SGS dissipation rates in wavenumber space, respectively and $\widehat{\nu}^*_{\text{SUPG}}(k',t)$ is the complex conjugate of the SUPG numerical viscosity in spectral space $\widehat{\nu}_{\text{SUPG}}(k',t)$.

Figure 6.27 shows a comparison of the spectra of effective viscosities for the FDV/ILES and the two SGS/LES runs on the 32^3 grid at the non-dimensional time $t^* = 3$. Figures 6.28 and 6.29 present these spectra for the 64^3 and 128^3 grids, respectively. Also presented are the numerical viscosity spectra of the SUPG method, which are computed for the same flow realization as the FDV/ILES run. The SUPG viscosity spectrum is computed from equation (6.14). As can be seen in Figure 6.27, the four viscosity spectra decrease up

to wavenumber $k \approx 5$, and then increase with wavenumber reaching a maximum near the cut-off wavenumber. The increase in effective viscosity at higher wavenumbers was also seen in the works of Thornber *et al.* [58] and Ciardi *et al.* [60]. The decrease in viscosity spectrum at low wavenumbers and the increase at high wavenumbers are desired trends, since the anticipation is for numerical viscosity to be active at high wavenumbers so as to account for the dynamics of scales smaller than the cut-off wavenumber. At all wavenumbers, the numerical viscosity spectrum of the SUPG method is substantially higher than that of FDV/ILES, as well as those of the two SGS/LES cases. This behavior is consistent with the higher viscosities seen for SUPG method in Figures 6.21-6.23. Similar trends are observed for the 64^3 and 128^3 grids, as shown in Figures 6.28 and 6.29, respectively.

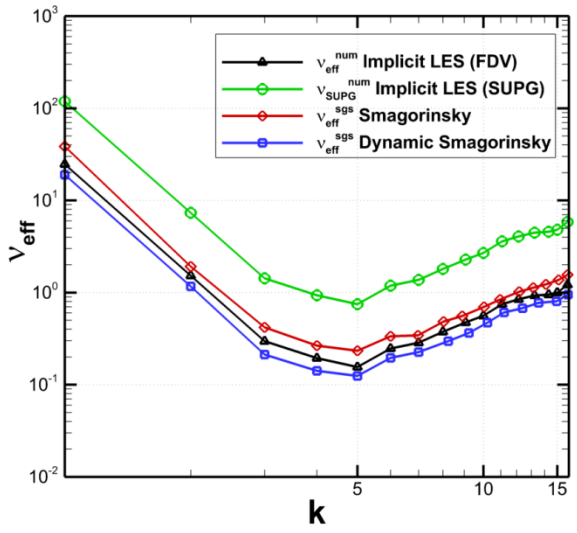

Figure 6.27 Comparison of spectra of effective viscosities of the three LES cases and the SUPG numerical viscosity at $t^* = 3$ on a 32^3grid.

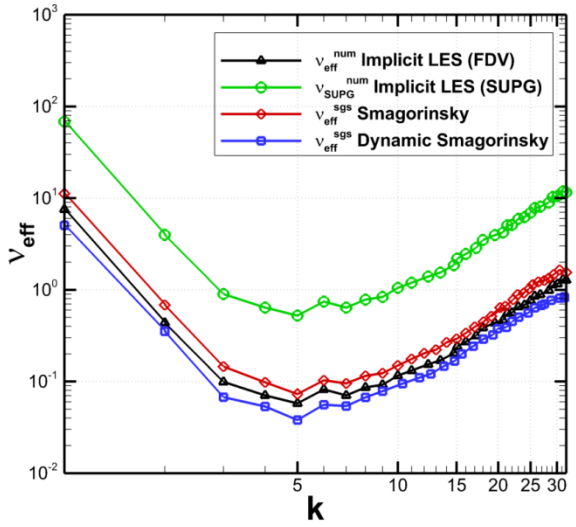

Figure 6.28 Comparison of spectra of effective viscosities of the three LES cases and the SUPG numerical viscosity at $t^* = 3$ on a 64^3grid.

.

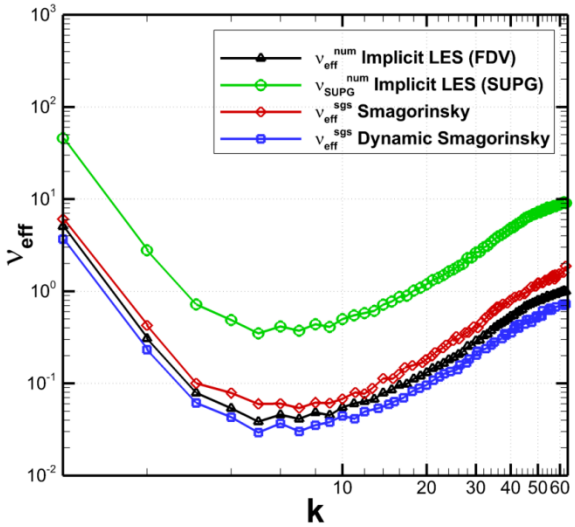

Figure 6.29 Comparison of spectra of effective viscosities of the three LES cases and the SUPG numerical viscosity at $t^* = 3$ on a 128^3grid.

CHAPTER 7

NUMERICAL VALIDATION TESTS

This chapter presents the numerical validation tests involving the simulations of freely decaying, inviscid and viscous isotropic turbulence. For the incompressible inviscid isotropic turbulence, the computed energy spectra from the dynamic Smagorinsky model-based Euler LES are compared with the experimental data of data of Comte-Bellot and Corrsin in Section 7.1. Comparisons of simulation results obtained from the Navier-Stokes LES and dynamic Smagorinsky model-based LES with the data from experiments and published literature are presented in Sections 7.2 and 7.3, respectively, for incompressible and compressible viscous isotropic turbulence.

7.1. Incompressible Inviscid Isotropic Turbulence

For the incompressible inviscid isotropic turbulence, the computed energy spectra obtained from the dynamic Smagorinsky model-based LES are compared with the experimental data of Comte-Bellot and Corrsin [67]. It should be noted that the Euler form of decaying isotropic turbulence is used to exclude the effects of physical molecular viscosity on the simulation results. The flow initialization conditions are the same as described in Section 6.2. The initial turbulent Mach number M_{t0} is set to 0.05 for the cases reported in this section, so that flow may be considered essentially incompressible. A constant time step $\Delta t = 10^{-3}$ is used for the computations. Simulations were performed on 64^3 and 128^3 grid resolutions.

Figures 7.1 and 7.2 present a comparison of the energy spectrum obtained from the dynamic Smagorinsky model-based Euler LES with the energy spectrum from the

experiment of Comte-Bellot and Corrsin on 64^3 and 128^3 grids, respectively. The spectra are shown at a dimensionless time of $tU_0/M = 98$ (where U_0 is the mean flow velocity, and M is the size of the turbulence-generating grid in the wind tunnel). Reasonable agreement is seen between the LES and experimental spectra on both grid resolutions, particularly at high wavenumbers.

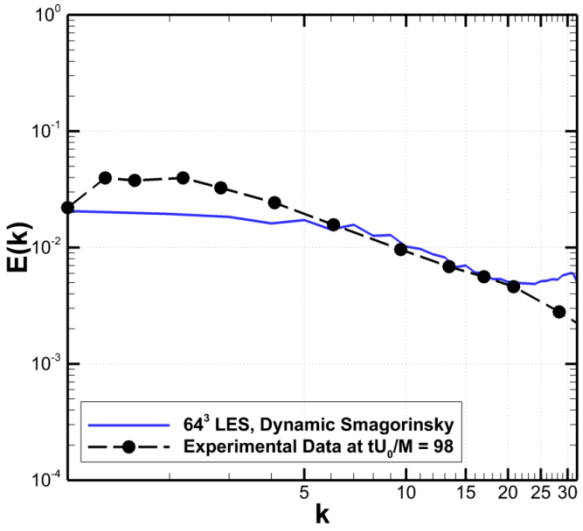

Figure 7.1 Comparison of computed Euler LES energy spectrum with experimental data of Comte-Bellot and Corrsin on a 64^3 grid.

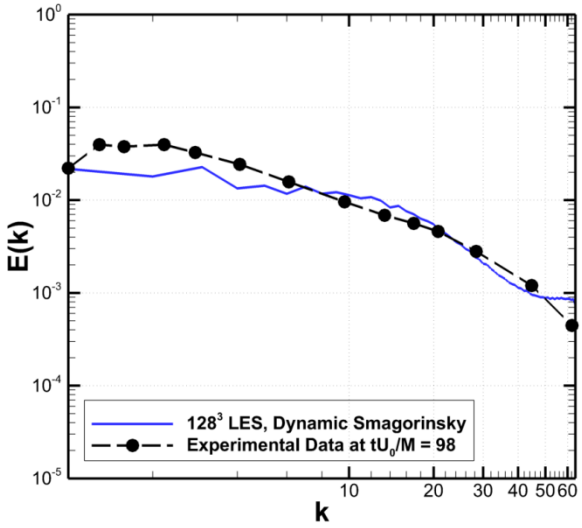

Figure 7.2 Comparison of computed Euler LES energy spectrum with experimental data of Comte-Bellot and Corrsin on a 128^3 grid.

7.2. Incompressible Viscous Isotropic Turbulence

For the incompressible simulations, freely decaying isotropic turbulence was performed with the conditions corresponding to the results of the experiment conducted by Comte-Bellot and Corrsin [67]. From their turbulence-generating grid in the wind tunnel, extensive experimental data were provided at three downstream locations, tU_0/M = 42, 98, and 171 (tU_0 is the downstream distance, U_0 is the mean flow velocity, and M is the grid size). The Taylor microscale Reynolds number in the experiment was $Re_\lambda = 72$ at the first station, $tU_0/M = 42$, and decreased to $Re_\lambda = 60$ at the last station, $tU_0/M = 171$. The present simulations were run with initial turbulent Mach number $M_{t0} = 0.1$ and the experimental spectrum at $tU_0/M = 42$ was used to initialize the flowfield using the method of Rogallo [68]. During the computations, the time step is constant, which corresponds to $CFL \approx 0.1$. Although the actual decay of experimental spectra is spatial,

Taylor's hypothesis can be used to compare the spatial decay with temporally decaying turbulence in a periodic box. To further assess the effects of grid refinement on the simulation results, two grid resolutions, 32^3 and 64^3, are used. Two different types of LES computations were performed; one with a dynamic Smagorinsky SGS model and the other without any explicit SGS model herein referred to as the Navier-Stokes ILES (i.e., Navier-Stokes simulations with no turbulence model).

Figures 7.3 and 7.4 compare the kinetic energy spectra obtained from the Navier-Stokes ILES and dynamic Smagorinsky model-based LES with experimental spectra of Comte-Bellot and Corrsin on 32^3 and 64^3 grids, respectively. Good agreement is seen between spectra of the dynamic Smagorinsky model-based LES and those of the experiment on both grid resolutions. From Figures 7.3 and 7.4, it is evident that the spectra obtained from the Navier-Stokes ILES case are inadequate to capture the actual decay of the experimental spectra for this value of $Re_\lambda = 72$. In fact, excessive energy build-up at high wavenumbers is seen in Figure 7.3. Thus, the need for an explicit SGS model is evident. The energy spectra obtained from the Navier-Stokes ILES case, performed on a 64^3 grid and shown in Figure 7.4, appear to be flatter, indicating that the numerical dissipation inherent to the FDV scheme does not dominate the SGS dissipation.

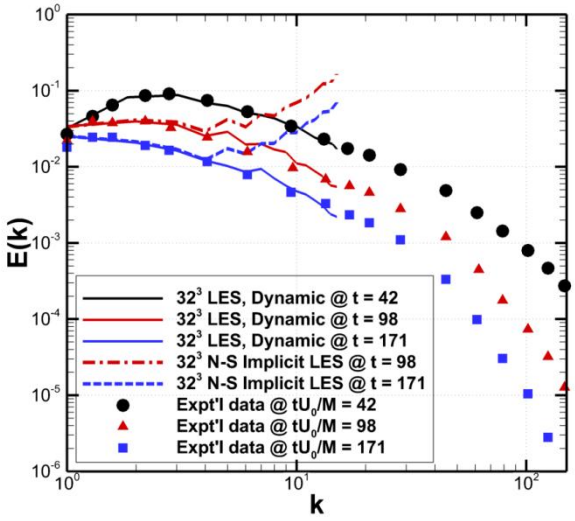

Figure 7.3 Comparison of computed Navier-Stokes LES energy spectra with experimental data of Comte-Bellot and Corrsin on a 32^3 grid.

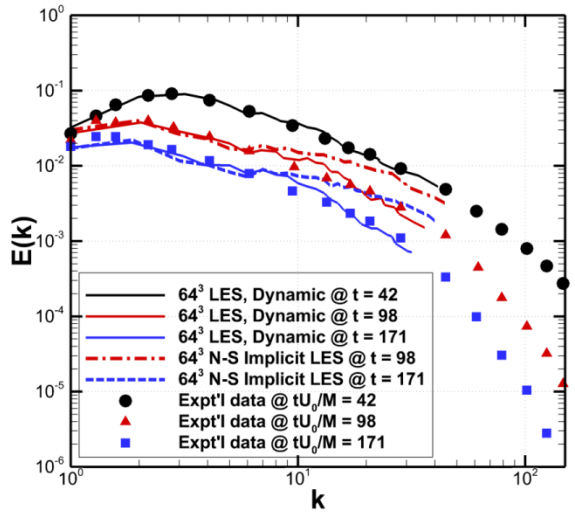

Figure 7.4 Comparison of computed Navier-Stokes LES energy spectra with experimental data of Comte-Bellot and Corrsin on a 64^3 grid.

The decay of resolved turbulent kinetic energy is compared with the filtered experimental data of Comte-Bellot and Corrsin in Figures 7.5 and 7.6 on 32^3 and 64^3 grids, respectively. The results obtained from the dynamic Smagorinsky model-based LES match

reasonably well with the experimental decay on both grid resolutions, although an over-prediction of the experimental decay is observed at measurement station tU_0/M = 98. Figures 7.5 and 7.6 show that the results obtained from the Navier-Stokes ILES case are incapable of accurately predicting the kinetic-energy decay obtained from the experiment. The resolved kinetic energy decay profile on a 64^3 grid appears to be flatter when compared to the corresponding profile for the 32^3 grid, suggesting lesser numerical dissipation as the grid is refined. The differences between the kinetic energy decay profiles obtained from the Navier-Stokes ILES case and dynamic Smagorinsky model-based LES case confirm that the numerical viscosity introduced by the FDV scheme is small compared to the SGS eddy-viscosity.

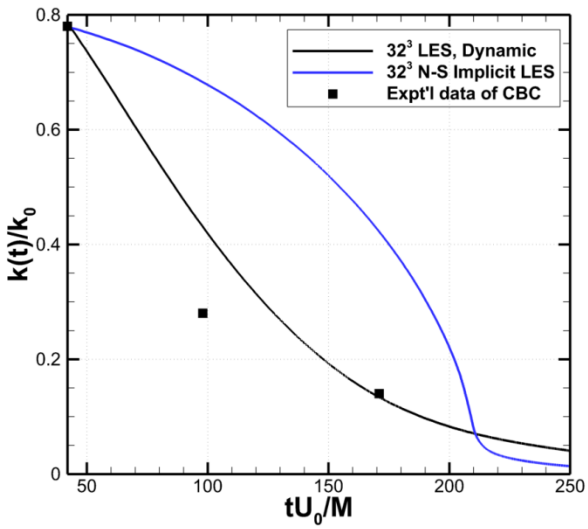

Figure 7.5 Comparison of decay of resolved kinetic energy from the Navier-Stokes LES with filtered experimental data of Comte-Bellot and Corrsin on a 32^3 grid.

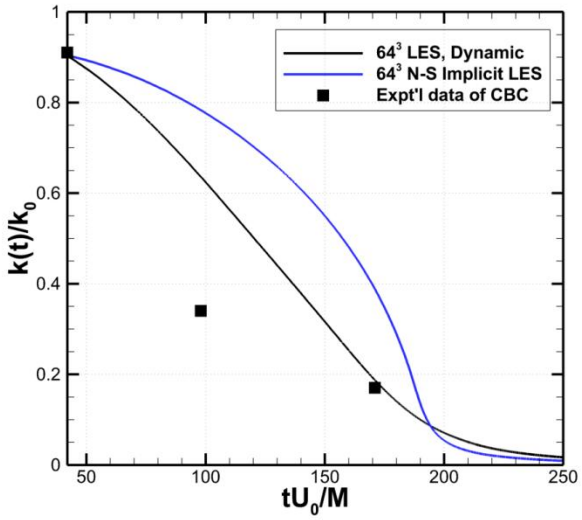

Figure 7.6 Comparison of decay of resolved kinetic energy from the Navier-Stokes LES with filtered experimental data of Comte-Bellot and Corrsin on a 64^3 grid.

7.3. Compressible Viscous Isotropic Turbulence

Simulations involving freely decaying compressible isotropic turbulence were performed with the initial conditions corresponding to case D4 of 128^3 DNS of Samtaney *et al* [57]. In their work, Samtaney and co-workers employed tenth-order compact finite difference scheme for the spatial discretization. The two types of LES computations namely, the Navier-Stokes ILES and dynamic Smagorinsky model-based LES were performed on a 64^3 grid resolution with the initial turbulent Mach number $M_{t0} = 0.30$ and the initial Taylor microscale Reynolds number $Re_\lambda = 72$. The initial flowfield was initialized as described in section 6.2. A constant time step $\Delta t = 10^{-3}$ is used for the computations. For freely decaying compressible turbulence, as time evolves both M_{t0} and Re_λ decrease with time. Therefore, there are essentially no shocks in these flows. The most

energetic wavenumber is set as $k_p = 4$. Direct numerical simulation (DNS) on a 128^3 grid resolution was also performed and plotted for comparison purposes.

Figure 7.7 presents a comparison of energy spectra from the Navier-Stokes ILES and dynamic Smagorinsky model-based LES with 128^3 DNS spectrum at $t/\tau = 2$. The spectrum from the Navier-Stokes ILES case (i.e., Navier-Stokes simulation with no turbulence model) shows an under-dissipative behavior at high wavenumbers when compared with the 128^3 DNS spectrum. There is an excellent agreement between the spectrum from the dynamic Smagorinsky model-based 64^3 LES and 128^3 DNS spectrum up to the cut-off wavenumber resolved by the LES.

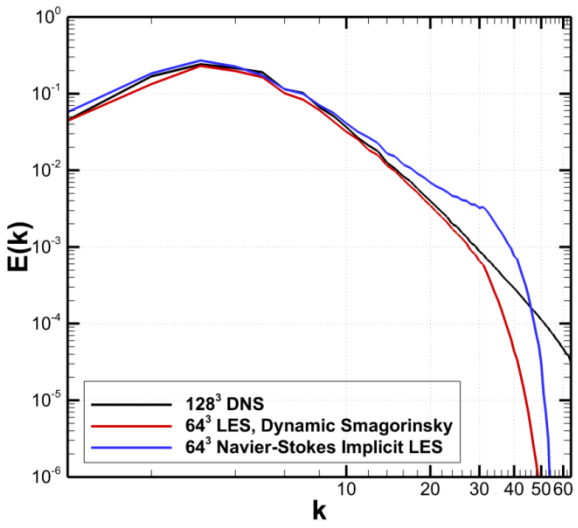

Figure 7.7 Comparison of LES energy spectra with 128^3 DNS spectrum at $t/\tau = 2$.

Figure 7.8 compares the temporal profiles of normalized kinetic energy from the Navier-Stokes ILES and dynamic Smagorinsky model-based LES with DNS of Samtaney *et al* [57]. The temporal profile of kinetic energy from the 64^3 Navier-Stokes ILES case

substantially over-predicts that of the 128^3 DNS result at most computational times. A good agreement is seen between the kinetic energy profile from the dynamic Smagorinsky model-based 64^3 LES case and that of 128^3 DNS of Samtaney *et al* [57]. These predictions justify the use of dynamic Smagorinsky SGS model in the compressible LES calculations using the FDV scheme.

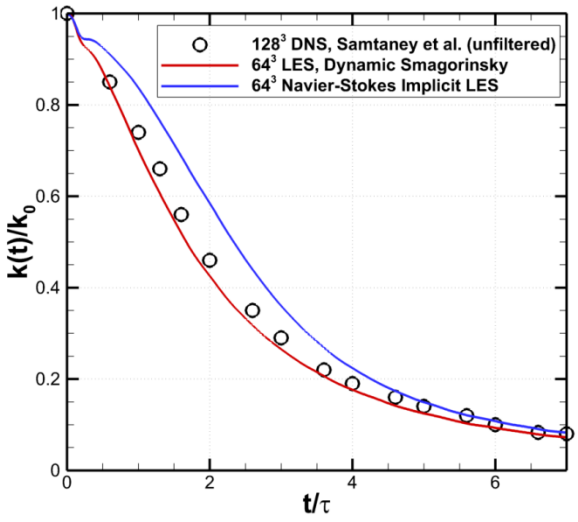

Figure 7.8 Comparison of temporal profiles of normalized kinetic energy from the Navier-Stokes LES with DNS of Samtaney *et al* [57]. The 128^3 DNS result is unfiltered.

Figure 7.9 shows a comparison of temporal profiles of normalized density fluctuations from the Navier-Stokes ILES and dynamic Smagorinsky model-based LES with DNS of Samtaney *et al* [57]. The density fluctuations in both LES cases initially grow with time as the energy is drained from the velocity field. After attaining their peaks at $t/\tau \approx 0.3$, the density fluctuations undergo unsteady decay with time. The unsteadiness in the rms density may be attributed to the compressibility effects in the flows. The decay rate

from the Navier-Stokes ILES has larger deviation from the reference DNS result. Thus, the 64^3 Navier-Stokes ILES case substantially over-predicts the 128^3 DNS result at most computational times. There is a good agreement between the rms density profile obtained from the dynamic Smagorinsky model-based 64^3 LES case and that of 128^3 DNS of Samtaney *et al* [57]. It should be noted that the DNS result is unfiltered and therefore contains some scales that are not resolved by the LES. Thus, a slight over-prediction of the rms density by the dynamic Smagorinsky model-based LES at early computational times is to be expected.

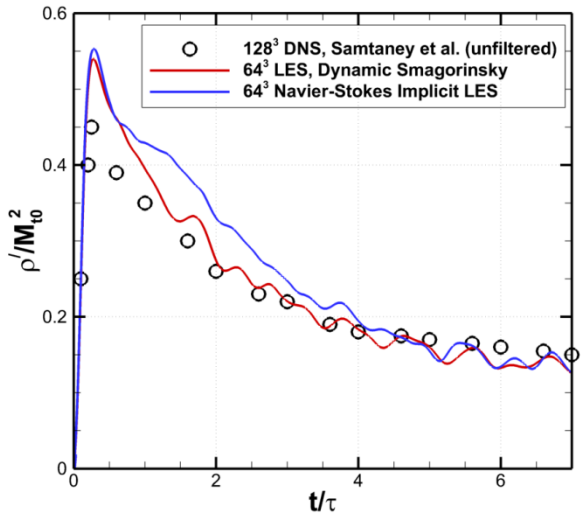

Figure 7.9 Comparison of temporal profiles of normalized density fluctuations from the Navier-Stokes LES with DNS of Samtaney *et al* [57]. The 128^3 DNS result is unfiltered.

Figure 7.10 presents a comparison of temporal profiles of skewness from the Navier-Stokes ILES and dynamic Smagorinsky model-based LES with DNS of Samtaney *et al* [57]. The temporal profile of skewness obtained from the 64^3 Navier-Stokes ILES case substantially over-predicts that of the 128^3 DNS at all computational times. The

skewness profile obtained from the dynamic Smagorinsky model-based 64^3 LES case shows good agreement with that of 128^3 DNS of Samtaney *et al* [57], despite the fact that the DNS result is unfiltered and contains some scales that are not resolved by the LES. These LES predictions further justify the use of dynamic Smagorinsky SGS model in the compressible LES calculations using the FDV scheme.

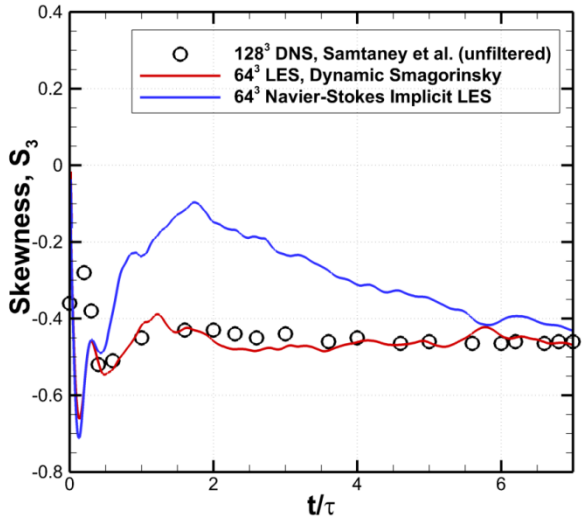

Figure 7.10 Comparison of temporal profiles of skewness from the Navier-Stokes LES with DNS of Samtaney *et al* [57]. The 128^3 DNS result is unfiltered.

CHAPTER 8

CONCLUSIONS

In this dissertation, some numerical characteristics of the Flowfield Dependent Variation (FDV) method were investigated. The spatial order-of-accuracy of the FDV scheme was established. Von Neumann stability analysis was conducted, which showed that FDV is more stable and less dispersive compared to Lax-Wendroff scheme. The dispersion errors due to FDV were characterized. A new formulation for quantifying the numerical viscosity inherent to the FDV scheme was developed. The intrinsic numerical viscosity and dissipation rate of FDV were quantified both in physical and spectral spaces.

At first, the Method of Manufactured Solutions (MMS) was applied to verify the spatial order-of-accuracy of the FDV scheme implemented in a compressible Navier-Stokes solver, which supports higher-order quadrilateral and hexahedral isoparametric Langrange elements. The order-of-accuracy test was carried out by comparing the numerical solutions to the exact (manufactured) solutions on a series of five different consistently-refined grid levels and three different orders of shape function polynomials. For the four test cases considered, spanning both inviscid Euler and laminar Navier-Stokes equations, the observed order-of-accuracy asymptotically approaches the formal order-of-accuracy of the FDV finite element method with corresponding *h*- and *p*-refinements, in good agreement with theory.

An extension of FDV method for large-eddy simulation (LES) of turbulent flows was presented. The governing equations suitable for LES, which comprises filtered Navier-Stokes system of equations, were formulated. The FDV parameters, the Jacobian terms of

the flux vectors and their gradients necessary for implementation of extra subgrid-scale (SGS) terms in the filtered equations were introduced. Justification for neglecting some terms containing the product of the diffusion gradient Jacobian $\boldsymbol{c}_{ij}$ with the third spatial derivatives of $\boldsymbol{F}_k$ and $\boldsymbol{G}_k$ was presented both qualitatively and quantitatively.

Two explicit subgrid-scale (SGS) closures namely, the standard Smagorinsky and dynamic Smagorinsky models were implemented in a newly-developed LES code. A finite element-based generalized top hat test filter was used for the dynamic model. The two SGS closures, as well as the implicit LES based on the numerical dissipation inherent to the FDV scheme were investigated and compared within the simulations of incompressible inviscid isotropic turbulence. The energy spectra from the implicit LES calculations showed reasonable agreement with the Kolmogorov's $k^{-5/3}$ power law in the inertial subrange, with the spectra moving closer to the Kolmogorov scaling at higher grid resolutions. The temporal profiles of kinetic energy also showed good agreement with the Kolmogorov's $t^{*-1.43}$ law of kinetic energy decay rate in the fully developed turbulent regime, particularly at 128^3 grid resolution.

Using the new formulation developed for quantifying the numerical viscosity inherent to the FDV scheme, the intrinsic numerical viscosity and dissipation rate of FDV were quantified both in magnitude and temporal distribution, and found to decrease in magnitude with an increase in grid resolution. When the FDV scheme was coupled with the two explicit SGS models, the numerical dissipation due to the scheme is found to be of the same order of magnitude in comparison with the SGS dissipation arising from the two SGS models. The FDV coupled with the standard Smagorinsky SGS model is the most dissipative among the three types of LES. Furthermore, at a finite number of flow

realizations, the numerical viscosities of FDV and that of the Streamline Upwind/Petrov-Galerkin (SUPG) finite element method were compared. In the initial stages of turbulence development, all the three LES cases have similar viscosities. But, once the turbulence is fully developed, implicit LES is less dissipative compared to the two SGS LES runs. It was also observed that the SUPG method is significantly more dissipative than the three LES approaches. The results from this study suggest that the FDV scheme has potential for implicit large-eddy simulations of incompressible free-shear turbulent flows.

For the LES computations involving incompressible viscous isotropic turbulence, the energy spectra and temporal profiles of kinetic energy obtained from the dynamic Smagorinsky model-based LES case showed good agreement with the experimental data of Comte-Bellot and Corrsin [67] on both 32^3 and 64^3 grid resolutions. Furthermore, the turbulent flow statistics (i.e., the temporal profiles of kinetic energy, density fluctuations, and skewness) obtained from the dynamic Smagorinsky model-based 64^3 LES case, involving compressible viscous isotropic turbulence, showed good agreement with 128^3 DNS data of Samtaney *et al* [57].

Utilization of high-order finite element methods for LES computations with a dynamic Smagorinsky model is possible through the use of higher-order shape function polynomials that enable efficient and accurate representation of turbulent flows on coarse grids. This will require the use of finite dimensional test filters other than the generalized top hat test filters currently employed, which are most appropriate for linear elements. The filter widths are not only expected to be smaller than the inertial subrange scales even on coarse grids for Smagorinsky model to be valid, but are also required to reflect the order of polynomial of shape function used [69]. The development of such a suitable class of finite

element-based test filters remains an open question and needs to be explored. A more detailed study of the effects of the neglected $\boldsymbol{c}_{ij}$ term that will be based on the asymptotic analysis of the eigenvalues of the Jacobian matrices awaits future research. The next logical step toward further investigation FDV scheme will involve large-eddy simulations of wall-bounded turbulent flows.

APPENDICES

APPENDIX A

FLUX JACOBIANS AND FLUX GRADIENTS

The Jacobians of the flux vectors $\boldsymbol{a}_i$, $\boldsymbol{b}_i$, and $\boldsymbol{c}_{ij}$ defined in equation (3.10) are necessary for the implementation of the FDV method. The first step to obtain these Jacobians is to write the convective flux vector $\boldsymbol{F}_i$ and the diffusive flux vector $\boldsymbol{G}_i$ given in equation (3.2) in terms of the conservation variables $\boldsymbol{U}$ and their gradients $\boldsymbol{U}_{,i}$. The second step is to differentiate with respect to $\boldsymbol{U}$ and $\boldsymbol{U}_{,i}$. Furthermore, the flux vector gradients $\boldsymbol{F}_{i,i}$ and $\boldsymbol{G}_{i,i}$ need to be evaluated as stated in equation (3.26). To preserve the order of accuracy imposed by the assumed shape functions, the flux vector gradients have to be written as functions of the vectors of the conserved variables and their respective gradients. Due to possible lengthy terms that could result when the flux Jacobians and the flux vector gradients are explicitly expanded in terms of the conserved variables and their gradients, the derivation process adopted herein employs an implicit differentiation technique. The gradients and Jacobians of various physical properties appearing in the fluxes are introduced in Section A.1, while Section A.2 summarizes the Jacobian terms for the filtered Navier-Stokes equations that are required for LES formulation. Section A.3 presents the justification for neglecting $\boldsymbol{c}_{ij}$ term in equation (3.9).

A.1 Physical Properties Jacobians and Gradients

The convective and the diffusive fluxes contain several physical properties which are generally non-linear functions of the conserved variables. The mathematical efforts required to analytically derive the flux Jacobians and the flux gradients, as well as the

complexity involved in the computer implementation for the resulting expressions, are greatly simplified by differentiating these terms implicitly. The listings of the derivatives of the different physical properties contained in the flux vectors are presented in this section. Each property is written in terms of the conserved variables, and the necessary Jacobian and gradient differentiations are introduced. Table A.1 summarizes all the physical properties that appear in the differentiation properties. It should be noted that the counters i, j, and k run from 1 to 3 , whereas counters r and s take values from 1 to 5.

Table A.1 List of the required physical properties gradients and Jacobians for implicit differentiation.

Filtered pressure:	$\bar{p}$	$\bar{p}_{,i}$	$\bar{p}_{,ij}$	$\frac{\partial \bar{p}}{\partial \boldsymbol{U}_r}$	$\frac{\partial \bar{p}_{,i}}{\partial \boldsymbol{U}_r}$	$\frac{\partial \bar{p}_{,i}}{\partial \boldsymbol{U}_{r,j}}$
Filtered temperature:	$\tilde{T}$	$\tilde{T}_{,i}$	$\tilde{T}_{,ij}$	$\frac{\partial \tilde{T}_{,i}}{\partial \boldsymbol{U}_r}$	$\frac{\partial \tilde{T}_{,i}}{\partial \boldsymbol{U}_{r,j}}$	
Filtered velocity vector:	$\tilde{u}_i$	$\tilde{u}_{i,j}$	$\tilde{u}_{i,jk}$	$\frac{\partial \tilde{u}_{i,j}}{\partial \boldsymbol{U}_r}$	$\frac{\partial \tilde{u}_{i,j}}{\partial \boldsymbol{U}_{r,k}}$	
Filtered viscous stress tensor:	$\tilde{\sigma}_{ij}$	$\tilde{\sigma}_{ij,k}$	$\frac{\partial \tilde{\sigma}_{ij}}{\partial \boldsymbol{U}_r}$	$\frac{\partial \tilde{\sigma}_{ij}}{\partial \boldsymbol{U}_{r,k}}$		
Subgrid-scale stress tensor:	τ_{ij}^{sgs}	$\tau_{ij,k}^{\text{sgs}}$	$\frac{\partial \tau_{ij}^{\text{sgs}}}{\partial \boldsymbol{U}_r}$	$\frac{\partial \tau_{ij}^{\text{sgs}}}{\partial \boldsymbol{U}_{r,k}}$		
Filtered strain-rate tensor:	$\tilde{S}_{ij}$	$\tilde{S}_{ij,k}$	$\frac{\partial \tilde{S}_{ij}}{\partial \boldsymbol{U}_r}$	$\frac{\partial \tilde{S}_{ij}}{\partial \boldsymbol{U}_{r,k}}$		
Filtered heat flux vector:	$\tilde{q}_i$	$\tilde{q}_{i,j}$	$\frac{\partial \tilde{q}_i}{\partial \boldsymbol{U}_r}$	$\frac{\partial \tilde{q}_i}{\partial \boldsymbol{U}_{r,k}}$		
Subgrid-scale heat flux vector:	q_i^{sgs}	$q_{i,j}^{\text{sgs}}$	$\frac{\partial q_i^{\text{sgs}}}{\partial \boldsymbol{U}_r}$	$\frac{\partial q_i^{\text{sgs}}}{\partial \boldsymbol{U}_{r,k}}$		
Turbulent SGS eddy-viscosity:	v_{sgs}	$v_{\text{sgs},i}$	$\frac{\partial v_{\text{sgs}}}{\partial \boldsymbol{U}_r}$	$\frac{\partial v_{\text{sgs}}}{\partial \boldsymbol{U}_{r,k}}$		
Filtered strain-rate tensor norm:	$\widetilde{\lvert S \rvert}$	$\widetilde{\lvert S \rvert}_{,i}$	$\frac{\partial \widetilde{\lvert S \rvert}}{\partial \boldsymbol{U}_r}$	$\frac{\partial \widetilde{\lvert S \rvert}}{\partial \boldsymbol{U}_{r,k}}$		

A.2 Filtered Navier-Stokes Jacobians

The explicit expansion of the filtered Navier-Stokes fluxes given in equation (3.2) are similar in all respect to their basic non-filtered Navier-Stokes counterparts except for the addition of the SGS terms (i.e., the SGS stress tensor τ_{ij} and the SGS heat flux vector q_i^{sgs}) to the diffusive flux vector $\boldsymbol{G}_i$. The detailed expansion of these non-filtered Navier-Stokes fluxes and their Jacobians are presented in the cited references [9] and [46]. The additional terms to the diffusive flux vector resulting in the diffusion Jacobian $\boldsymbol{b}_i$ and its gradient $\boldsymbol{c}_{ij}$ are presented below.

SGS diffusive flux vector $\boldsymbol{G_i^{sgs}} = \begin{bmatrix} 0 \\ \tau_{ij}^{\text{sgs}} \\ c_p q_i^{\text{sgs}} \end{bmatrix}$ A.1

SGS diffusive flux vector gradient $\boldsymbol{G_{i,k}^{sgs}} = \begin{bmatrix} 0 \\ \tau_{ij,k}^{\text{sgs}} \\ c_p q_{i,k}^{\text{sgs}} \end{bmatrix}$ A.2

SGS diffusion Jacobian $\frac{\partial \boldsymbol{G_i^{sgs}}}{\partial \boldsymbol{U}_s} = \begin{bmatrix} 0 \\ \frac{\partial \tau_{ij}^{\text{sgs}}}{\partial \boldsymbol{U}_s} \\ c_p \frac{\partial q_i^{\text{sgs}}}{\partial \boldsymbol{U}_s} \end{bmatrix}$ A.3

SGS diffusion gradient Jacobian $\frac{\partial \boldsymbol{G_i^{sgs}}}{\partial \boldsymbol{U}_{s,k}} = \begin{bmatrix} 0 \\ \frac{\partial \tau_{ij}^{\text{sgs}}}{\partial \boldsymbol{U}_{s,k}} \\ c_p \frac{\partial q_i^{\text{sgs}}}{\partial \boldsymbol{U}_{s,k}} \end{bmatrix}$ A.4

- Filtered strain-rate tensor

  $\tilde{S}_{ij} = \frac{1}{2}\left(\tilde{u}_{i,j} + \tilde{u}_{j,i}\right)$

  $\tilde{S}_{ij,k} = \frac{1}{2}\left(\tilde{u}_{i,jk} + \tilde{u}_{j,ik}\right)$

$$\frac{\partial \tilde{S}_{ij}}{\partial \boldsymbol{U}_r} = \frac{1}{2}\left(\frac{\partial \tilde{u}_{i,j}}{\partial \boldsymbol{U}_r} + \frac{\partial \tilde{u}_{j,i}}{\partial \boldsymbol{U}_r}\right)$$

$$\frac{\partial \tilde{S}_{ij}}{\partial \boldsymbol{U}_{r,k}} = \frac{1}{2}\left(\frac{\partial \tilde{u}_{i,j}}{\partial \boldsymbol{U}_{r,k}} + \frac{\partial \tilde{u}_{j,i}}{\partial \boldsymbol{U}_{r,k}}\right)$$

- Filtered strain-rate tensor norm

$$\widetilde{|S|} = \left(2\tilde{S}_{ij}\tilde{S}_{ij}\right)^{1/2}$$

$$\widetilde{|S|}_{,i} = \frac{2\tilde{S}_{ij}\tilde{S}_{ij,k}}{\widetilde{|S|}}$$

$$\frac{\partial \widetilde{|S|}}{\partial \boldsymbol{U}_r} = \frac{2\,\tilde{S}_{ij}}{\widetilde{|S|}}\frac{\partial\,\tilde{S}_{ij}}{\partial \boldsymbol{U}_r}$$

$$\frac{\partial \widetilde{|S|}}{\partial \boldsymbol{U}_{r,k}} = \frac{2\,\tilde{S}_{ij}}{\widetilde{|S|}}\frac{\partial\,\tilde{S}_{ij}}{\partial \boldsymbol{U}_{r,k}}$$

- Turbulent eddy viscosity

$$v_{\text{sgs}} = {C_s}^2\bar{\Delta}^2\widetilde{|S|}$$

$$v_{\text{sgs},i} = {C_s}^2\bar{\Delta}^2\widetilde{|S|}_{,i}$$

$$\frac{\partial v_{\text{sgs}}}{\partial \boldsymbol{U}_r} = {C_s}^2\bar{\Delta}^2\frac{\partial \widetilde{|S|}}{\partial \boldsymbol{U}_r}$$

$$\frac{\partial v_{\text{sgs}}}{\partial \boldsymbol{U}_{r,k}} = {C_s}^2\bar{\Delta}^2\frac{\partial \widetilde{|S|}}{\partial \boldsymbol{U}_{r,k}}$$

- SGS stress tensor

$$\tau_{ij}^{\text{sgs}} = -2\boldsymbol{U}_1 v_{\text{sgs}}\left(\tilde{S}_{ij} - \tfrac{1}{3}\delta_{ij}\tilde{S}_{nn}\right)$$

$$\tau_{ij,k}^{\text{sgs}} = -2\begin{bmatrix} \boldsymbol{U}_{1,k} v_{\text{sgs}} \left(\tilde{S}_{ij} - \frac{1}{3}\delta_{ij}\tilde{S}_{nn}\right) + \boldsymbol{U}_1 v_{\text{sgs},k} \left(\tilde{S}_{ij} - \frac{1}{3}\delta_{ij}\tilde{S}_{nn}\right) \\ + \boldsymbol{U}_1 v_{\text{sgs}} \left(\tilde{S}_{ij,k} - \frac{1}{3}\delta_{ij}\tilde{S}_{nn,k}\right) \end{bmatrix}$$

$$\frac{\partial \tau_{ij}^{\text{sgs}}}{\partial \boldsymbol{U}_1} = -2\begin{bmatrix} v_{\text{sgs}} \left(\tilde{S}_{ij} - \frac{1}{3}\delta_{ij}\tilde{S}_{nn}\right) + \boldsymbol{U}_1 \frac{\partial v_{\text{sgs}}}{\partial \boldsymbol{U}_1} \left(\tilde{S}_{ij} - \frac{1}{3}\delta_{ij}\tilde{S}_{nn}\right) \\ + \boldsymbol{U}_1 v_{\text{sgs}} \left(\frac{\partial \tilde{S}_{ij}}{\partial \boldsymbol{U}_1} - \frac{1}{3}\delta_{ij}\frac{\partial \tilde{S}_{nn}}{\partial \boldsymbol{U}_1}\right) \end{bmatrix}$$

$$\frac{\partial \tau_{ij}^{\text{sgs}}}{\partial \boldsymbol{U}_{k+1}} = -2\boldsymbol{U}_1 \left[\frac{\partial v_{\text{sgs}}}{\partial \boldsymbol{U}_{k+1}} \left(\tilde{S}_{ij} - \frac{1}{3}\delta_{ij}\tilde{S}_{nn}\right) + v_{\text{sgs}} \left(\frac{\partial \tilde{S}_{ij}}{\partial \boldsymbol{U}_{k+1}} - \frac{1}{3}\delta_{ij}\frac{\partial \tilde{S}_{nn}}{\partial \boldsymbol{U}_{k+1}}\right)\right]$$

$$\frac{\partial \tau_{ij}^{\text{sgs}}}{\partial \boldsymbol{U}_5} = 0$$

$$\frac{\partial \tau_{ij}^{\text{sgs}}}{\partial \boldsymbol{U}_{r,k}} = -2\boldsymbol{U}_1 \left[\frac{\partial v_{\text{sgs}}}{\partial \boldsymbol{U}_{r,k}} \left(\tilde{S}_{ij} - \frac{1}{3}\delta_{ij}\tilde{S}_{nn}\right) + v_{\text{sgs}} \left(\frac{\partial \tilde{S}_{ij}}{\partial \boldsymbol{U}_{r,k}} - \frac{1}{3}\delta_{ij}\frac{\partial \tilde{S}_{nn}}{\partial \boldsymbol{U}_{r,k}}\right)\right]$$

- SGS heat flux vector

$$q_i^{\text{sgs}} = -\boldsymbol{U}_1 \frac{v_{\text{sgs}}}{Pr_t}\frac{\partial \tilde{T}}{\partial x_i}$$

$$q_{i,j}^{\text{sgs}} = -\frac{1}{Pr_t}\left(\boldsymbol{U}_{1,j} v_{\text{sgs}}\frac{\partial \tilde{T}}{\partial x_i} + \boldsymbol{U}_1 v_{\text{sgs},j}\frac{\partial \tilde{T}}{\partial x_i} + \boldsymbol{U}_1 v_{\text{sgs}}\tilde{T}_{,ij}\right)$$

$$\frac{\partial q_i^{\text{sgs}}}{\partial \boldsymbol{U}_1} = -\frac{1}{Pr_t}\left(v_{\text{sgs}}\frac{\partial \tilde{T}}{\partial x_i} + \boldsymbol{U}_1 \frac{\partial v_{\text{sgs}}}{\partial \boldsymbol{U}_1}\frac{\partial \tilde{T}}{\partial x_i} + \boldsymbol{U}_1 v_{\text{sgs}}\frac{\partial \tilde{T}_{,i}}{\partial \boldsymbol{U}_1}\right)$$

$$\frac{\partial q_i^{\text{sgs}}}{\partial \boldsymbol{U}_{j+1}} = -\frac{\boldsymbol{U}_1}{Pr_t}\left(\frac{\partial v_{\text{sgs}}}{\partial \boldsymbol{U}_{j+1}}\frac{\partial \tilde{T}}{\partial x_i} + v_{\text{sgs}}\frac{\partial \tilde{T}_{,i}}{\partial \boldsymbol{U}_{j+1}}\right)$$

$$\frac{\partial q_i^{\text{sgs}}}{\partial \boldsymbol{U}_5} = -\boldsymbol{U}_1 \frac{v_{\text{sgs}}}{Pr_t}\frac{\partial \tilde{T}_{,i}}{\partial \boldsymbol{U}_5}$$

$$\frac{\partial q_i^{\text{sgs}}}{\partial \boldsymbol{U}_{r,k}} = -\frac{\boldsymbol{U}_1}{Pr_t}\left(\frac{\partial v_{\text{sgs}}}{\partial \boldsymbol{U}_{r,k}}\frac{\partial \tilde{T}}{\partial x_i} + v_{\text{sgs}}\frac{\partial \tilde{T}_{,i}}{\partial \boldsymbol{U}_{r,k}}\right)$$

A.3 Justification for Neglecting $\boldsymbol{c}_{ij}$ Term

In this Appendix, justification for neglecting the term containing the product of the diffusion gradient Jacobian $\boldsymbol{c}_{ij}$ with the third-order spatial derivatives of $\boldsymbol{F}_k$ and $\boldsymbol{G}_k$ in equation (3.9) is presented both qualitatively and quantitatively [12]. The qualitative justification involves the study of the nature of the Jacobian matrices. The representatives of $\boldsymbol{a}_i$, $\boldsymbol{b}_i$ and $\boldsymbol{c}_{ij}$ matrices are shown in Tables A.2, A.3 and A.4, respectively. One notices the following features in these Jacobians:

- $\boldsymbol{c}_{ij}$ term contains the third-order spatial derivatives of $\boldsymbol{F}_k$ and $\boldsymbol{G}_k$ with much smaller quantitative effect compared to the lower order spatial derivatives on the right-hand side of equation (3.9)
- $\boldsymbol{c}_{ij}$ Jacobian is much sparser than both $\boldsymbol{a}_i$ and $\boldsymbol{b}_i$, suggesting that its contribution to the overall calculations will be smaller than that of the two Jacobians retained.
- Using α and β to represent particular values of indices i and j, it is observed that the row of $\boldsymbol{c}_{\alpha\beta}$ corresponding to the velocity component v_γ is identically zero, where $\gamma \neq \alpha$, $\gamma \neq \beta$, and $\alpha \neq \beta$. That is, $\boldsymbol{c}_{\beta\alpha}$ makes no contribution to the calculation of v_γ. Similarly, $\boldsymbol{c}_{\alpha\beta}$ also makes no contribution to the calculation of v_γ. For instance, if one were to consider the $\boldsymbol{c}_{23}$ and $\boldsymbol{c}_{32}$ Jacobians, the row corresponding to the ρv_1 velocity component is zero in both matrices.
- It was observed during the simulations that the magnitude of elements in $\boldsymbol{c}_{ij}$ is typically much smaller than that of elements in $\boldsymbol{a}_i$ and $\boldsymbol{b}_i$. To demonstrate this observation, the isocontours of the norms of $\boldsymbol{a}_i$, $\boldsymbol{b}_i$ and $\boldsymbol{c}_{ij}$ are shown in Figures A.1 and A.2.

- Characteristic Reynolds numbers of the flow away from the wall are typically large ($Re \gg 1$) so that the convective terms dominate the viscous terms. Accordingly, convective Jacobians are dominant among the three Jacobians of interest. As discussed above, the magnitude of the elements in $\boldsymbol{c}_{ij}$ is the smallest among the three Jacobians. This is found to be the case even near walls.

The quantitative justification for neglecting the term involving $\boldsymbol{c}_{ij}$ involves comparing the orders of magnitude of the norms of the three Jacobians $\boldsymbol{a}_i$, $\boldsymbol{b}_i$ and $\boldsymbol{c}_{ij}$. Figures A.1 and A.2 present the iso-contours of the L_2 norms of the three Jacobians $\boldsymbol{a}_i$, $\boldsymbol{b}_i$, and $\boldsymbol{c}_{ij}$. It is seen that the L_2 norm of $\boldsymbol{c}_{ij}$ is maximum near the wall, which follows from the fact that $\boldsymbol{c}_{ij}$ represents viscous effects that are dominant near the wall. More importantly, the L_2 norm of $\boldsymbol{c}_{ij}$ is $O(10^4 \sim 10^5)$ smaller than the L_2 norm of $\boldsymbol{a}_i$ (and hence $\boldsymbol{a}_i$ + $\boldsymbol{b}_i$). Thus, one can neglect the term containing $\boldsymbol{c}_{ij}$ on the right-hand side of equation (3.9).

Table A.2 Navier-Stokes $\boldsymbol{a_1}$ Jacobian

0	1	0	0	0
a_{21}^1	$(3-\gamma)u_1$	$(1-\gamma)u_1$	$(1-\gamma)u_3$	$(\gamma-1)$
$-u_1u_2$	u_2	u_1	0	0
$-u_1u_3$	u_3	0	u_1	0
a_{51}^1	a_{52}^1	$(1-\gamma)u_1u_2$	$(1-\gamma)u_1u_3$	γu_1

$$a_{21}^1 = \frac{1}{2}\left((\gamma-3)u_1^2 + (\gamma-1)(u_2^2+u_3^2)\right)$$

$$a_{51}^1 = -u_1\left((1-\gamma)(u_1^2+u_2^2+u_3^2) + \gamma e_t\right)$$

$$a_{52}^1 = \gamma e_t + \frac{1-\gamma}{2}(3u_1^2+u_2^2+u_3^2)$$

Table A.3 Navier-Stokes $\boldsymbol{b_1}$ Jacobian

0	0	0	0	0
b_{21}^1	$\frac{\mu_R \rho,1}{\rho^2}$	$\frac{\lambda \rho,2}{\rho^2}$	$\frac{\lambda \rho,3}{\rho^2}$	0
b_{31}^1	$\frac{\mu \rho,2}{\rho^2}$	$\frac{\mu \rho,1}{\rho^2}$	0	0
b_{41}^1	$\frac{\mu \rho,3}{\rho^2}$	0	$\frac{\mu \rho,1}{\rho^2}$	0
b_{51}^1	b_{52}^1	b_{53}^1	b_{54}^1	$\frac{k \rho,1}{\rho^2 c_v}$

Table A.4 Navier-Stokes $\boldsymbol{c_{23}}$ Jacobian

0	0	0	0	0
0	0	0	0	0
$\frac{\lambda u_3}{\rho}$	0	0	$\frac{-\lambda}{\rho}$	0
$\frac{\mu u_2}{\rho}$	0	$\frac{-\mu}{\rho}$	0	0
$(\mu + \lambda)\frac{u_2 u_3}{\rho}$	0	$\frac{-\mu u_3}{\rho}$	$\frac{-\lambda u_2}{\rho}$	0

(a) $\boldsymbol{a_i}$

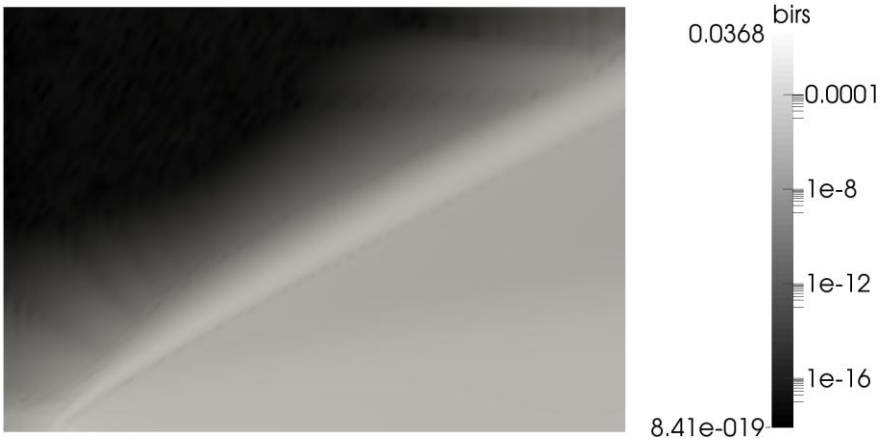

(b) $\boldsymbol{b}_i$

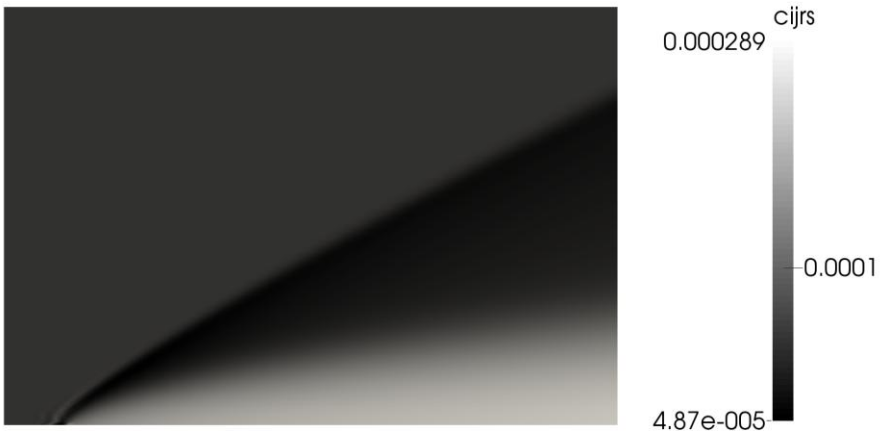

(c) $\boldsymbol{c}_{ij}$

Figure A.1: Contour plots of L_2 norms of Jacobians for supersonic flow over flat plate: (a) $\boldsymbol{a}_i$, (b) $\boldsymbol{b}_i$, and (c) $\boldsymbol{c}_{ij}$.

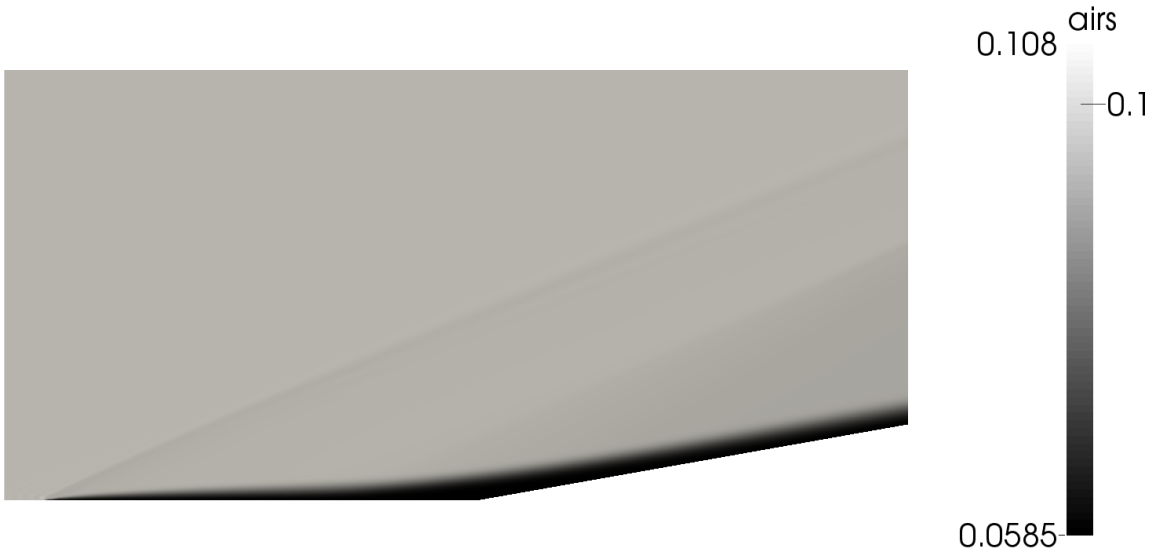

(a) $\boldsymbol{a}_i$

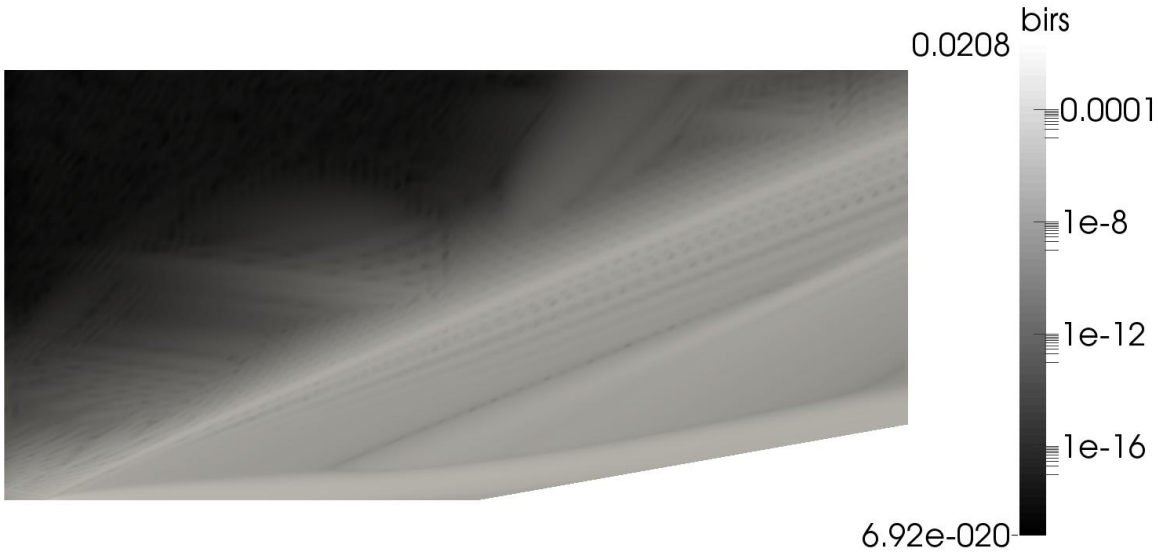

(b) $\boldsymbol{b}_i$

(c) $\boldsymbol{c}_{ij}$

Figure A.2: Contour plots of L_2 norms of Jacobians for supersonic flow over compression corner: (a) $\boldsymbol{a}_i$, (b) $\boldsymbol{b}_i$, and (c) $\boldsymbol{c}_{ij}$.

APPENDIX B

COEFFICIENTS USED IN THE MANUFACTURED SOLUTIONS

The values of the coefficients used in the manufactured solutions for Euler and Navier-Stokes equations consisting of the supersonic and subsonic flow cases are tabulated below. It should be noted that a_i constants have the same dimensions as the primitive variables and b_i constants are dimensionless.

Table B.1 Constants for Subsonic Euler Manufactured Solution

Variable, ϕ	a_0	a_1	a_2	a_3	b_1	b_2	b_3
ρ (kg/m^3)	1	0.15	-0.1	0	1	0.5	0
u (m/s)	70	5	-7	0	1.5	0.6	0
v (m/s)	90	-15	8.5	0	0.5	2/3	0
p (N/m^2)	1 x 10^5	2 x 10^4	5 x 10^4	0	2	1	0

Source: Ref. [53]

Table B.2 Constants for Supersonic Euler Manufactured Solution

Variable, ϕ	a_0	a_1	a_2	a_3	b_1	b_2	b_3
ρ (kg/m^3)	1	0.15	-0.1	0	1	0.5	0
u (m/s)	800	50	-30	0	1.5	0.6	0
v (m/s)	800	-75	40	0	0.5	2/3	0
p (N/m^2)	1 x 10^5	2 x 10^4	5 x 10^4	0	2	1	0

Source: Ref. [53]

Table B.3 Constants for Subsonic Navier-Stokes Manufactured Solution

Variable, ϕ	a_0	a_1	a_2	a_3	b_1	b_2	b_3
ρ (kg/m^3)	1	0.1	0.15	0.08	0.75	1	1.25
u (m/s)	70	4	-12	7	5/3	1.5	0.6
v (m/s)	90	-20	4	-11	1.5	1	0.9
p (N/m^2)	1 x 10^5	-3 x 10^4	2 x 10^4	-2.5 x 10^4	1	1.25	0.75

Source: Ref. [53]

Table B.4 Constants for Supersonic Navier-Stokes Manufactured Solution

Variable, ϕ	a_0	a_1	a_2	a_3	b_1	b_2	b_3
ρ (kg/m^3)	1	0.15	-0.1	0.08	1	0.5	1.25
u (m/s)	800	50	-30	7	1.5	0.6	0.6
v (m/s)	800	-75	40	-11	0.5	1.5	0.9
p (N/m^2)	1 x 10^5	2 x 10^4	5 x 10^4	-2.5 x 10^4	2/3	1	0.75

Source: Ref. [53]

REFERENCES

[1] J. Green. Interactions between shock waves and turbulent boundary layers. *Progress in Aerospace Sciences,* 11:235-340, 1970.

[2] R. H. Korkegi. Survey of viscous interactions associated with high Mach number flight. *AIAA Journal,* 9:771-784, 1971.

[3] T. Adamson, and A. Messiter. Analysis of two-dimensional interactions between shock waves and boundary layers. *Annual Review of Fluid Mech*anics, 12:103-138, 1980.

[4] G. S. Settles. Experimental research on swept shock wave/boundary layer interactions. *Technical Report* 8823, Air Force, 1988.

[5] G. A. Richardson and T. J. Chung. Computational relastivitic astrophysics using the flowfield-dependent variation theory. *The Astrophysical Journal Supplement Series*, 139:539-563, 2002.

[6] G. A. Richardson, T. J. Cassibry, T. J. Chung, and S. T.Wu. Finite element form of fdv for widely varying flowfield. *Journal of Computational Physics,* 229:145-167, 2010.

[7] K. T. Yoon and T. J. Chung. Three dimensional mixed explicit-implicit generalized Galerkin spectral element methods for high speed turbulent compressible flows. *Computer Methods in Applied Mechanics and Engineering*, 135:343-367, 1996.

[8] K. T. Yoon, S. Y. Moon, S. A. Garcia, G. W. Heard, and T. J. Chung. Flowfield-dependent mixed explicit-implicit (FDMEI) methods for high and low speed and compressible and incompressible flows. *Computer Methods in Applied Mechanics and Engineering,* 151:75-104, 1998.

[9] T. J. Chung. *Computational Fluid Dynamics*. Cambridge University Press, 2002.

[10] W. H. Reed, T. R. Hill, Triangular Mesh Methods for the Neutron Transport Equation, Technical Report LA-UR-73-479, Los Alamos National Laboratory, New Mexico, U.S.A., 1973.

[11] E. M. Collins, On Mesh Quality Considerations for the Discontinuous Galerkin Method, PhD thesis in computational engineering, Mississippi State University, 2009.

[12] B. Girgis, S. L. Rani, and A. Frendi. Flowfield dependent variation method: A numerical scheme for the solution of low- to high Mach number flow problems. *International Journal of Numerical Methods for Heat & Fluid Flow,* in press, 2015.

[13] S. Y. Moon, C. H. Sohn, and C. W. Lee. Applications of a flowfield-dependent mixed explicit-implicit (FDMEI) method to heat and fluid dynamics problems. *Numerical Heat Transfer*, 39:389-404, 2001.

[14] F. Canabal and A. Frendi. Study of the ignition over-pressure suppression technique by water addition. *Spacecraft and Rockets*, 43(4):853-865, 2006.

[15] E. Garnier, N. Adams, and P. Sagaut. *Large Eddy Simulation for Compressible Flows*. Springer, 2009.

[16] S. B. Pope. *Turbulent Flows.* Cambridge University Press, Cambridge, 2000.

[17] H. Pitsch, O. Desjardins, G. Balarac, and M. Ihme. Large-eddy simulation of turbulent reacting flows. *Progress in Aerospace Science*, 44:466-478, 2008.

[18] D. Haworth and K. Jansen. Large-eddy simulation on unstructured deforming meshes: towards reciprocating IC engines. *Computers and Fluids* 29(5):493-524, 2000.

[19] M. Berglund and C. Fureby. Large-eddy simulation of flow in a solid rocket motor. In Proceedings of 39th AIAA Aerospace Sciences Meeting and Exhibit, *AIAA paper 2001-0895*, Reno, Nevada, 2001.

[20] P. Moin and S. V. Apte. Large-eddy simulation of realistic gas turbine combustors. *AIAA Journal*, 44(4): 698-708, 2006.

[21] C. T. Wall and P. Moin. Numerical methods for large eddy simulation of acoustic combustion instabilities. *Tech. Rep. TF-91*. Stanford, CA: Stanford Univ., 2005.

[22] D. J. Bonody and S. K. Lele. Current status of jet noise predictions using large-eddy simulation. *AIAA Journal*, 46(2): 364-380, 2008.

[23] G. Eggenspieler and S. Menon. Large-eddy simulation of pollutant emission in a DOE-HAT combustor. *Journal of Propulsion and Power*, 20(6):1076-1085, 2004.

[24] P. J. Mason. Large-eddy simulations: a critical review of the technique. *Quarterly Journal of the Royal Meteorology Society* 120(515):1-26, 1994.

[25] J. S. Smagorinsky. General circulation experiments with the primitive equations I. The basic experiment. *Monthly Weather Review*, 91(3):99-164, 1963.

[26] D. K. Lilly. On the application of the eddy viscosity concept in the inertial subrange of turbulence. *NCAR Manuscript 123*, Boulder, Colorado, 1966.

[27] K. E. Jansen. Preliminary large-eddy simulation of flow around a NACA 4412 airfoil using unstructured grids. In CTR *Annual Research Briefs.* Stanford, CA: Center for Turbulence Research, NASA Ames/Stanford Univ., 61-72, 1995.

[28] K. E. Jansen. A stabilized finite element method for computing turbulence. *Computer Methods in Applied Mechanics and Engineering*, 174:299-317, 1999.

[29] F. Chalot, B. Marquez, M. Ravachol, F. Ducros, F. Nicoud, and T. Poinsot. A consistent finite approach to large-eddy simulation. *AIAA paper 98-2652*, 1998.

[30] Tejada-Martínez, A. E. and K. E. Jansen. A dynamic Smagorinsky model with dynamic determination of the filter width ratio. *Physics of Fluids*, 16:2514-2528, 2004.

[31] V. Levasseur, P. Sagaut, F. Chalot, and A. Davroux. An entrophy-variable-based VMS/GLS method for the simulation of compressible flows on unstructured grids. *Computer Methods in Applied Mechanics and Engineering*, 195:1154-1179, 2006.

[32] A. Leonard. Energy cascade in large-eddy simulations of turbulent fluid flows. *Advances in Geophysics*, 18A:237-248, 1974.

[33] A. Favre. Turbulence: Space-time statistical properties and behavior in supersonic flows. *Physics of Fluids*, 26(10): 2851-2863, 1983.

[34] B. Vreman, B. Guerts, and H. Kuerten. A priori tests of large-eddy simulation of the compressible plane mixing layer. *J. Eng. Math.*, 29: 299-327, 1995.

[35] B. Vreman, B. Guerts and H. Kuerten. Large-eddy simulation of turbulent mixing layers. *J. Fluid Mech.*, 339:357-390, 1997.

[36] P. Moin, K. Squires, W. Cabot, and S. Lee. A dynamic subgrid model for compressible turbulence and scalar transport. *Physics of Fluids A*, 3(11):2746-2757, 1991.

[37] M. Germano, U. Piomelli, P. Moin, and W. H. Cabot. A dynamic subgrid-scale eddy viscosity model. *Physics of Fluids A*, 3(7): 1760-1765, 1991.

[38] A. Yoshizawa. Statistical theory for compressible turbulent shear flows with the application to subgrid modeling. *Physics of Fluids A*, 29(7): 2152-2164, 1986.

[39] G. Erlebacher, M. Y. Hussaini, C. G. Speziale, and T. A. Zang. Toward the large-eddy simulation of compressible turbulent flows. *J. Fluid Mech.*, 238:155-185, 1992.

[40] T. A. Zang, R. B. Dahlburg, and J. P. Dahlburg. Direct and large-eddy simulations of three-dimensional compressible Navier-Stokes turbulence. *Physics of Fluids A*, 4(1): 127-140, 1992.

[41] D. K. Lilly. A proposed modification of the Germano subgrid-scale closure method. *Physics of Fluids A*, 4(3): 633-635, 1992.

[42] E. Garnier, M. Mossi, P. Sagaut, P. Comte and M. Deville. On the use of shock-capturing schemes for large-eddy simulation. *Journal of Computational Physics*, 153: 273-311, 1999.

[43] A. E. Tejada-Martínez and K. E. Jansen. Spatial test filters for dynamic model large-eddy simulation on finite elements. *Communications in Numerical Methods in Engineering*, 19:205-213, 2003.

[44] A. N. Brooks and T. J. R. Hughes. Streamline upwind/Petrov Galerkin formulations for convection dominated flows with particular emphasis on the incompressible Navier-Stokes equations. *Computer Methods in Applied Mechanics and Engineering*, 32:199-259, 1982.

[45] G. Karypis and V. Kumar. *METIS: unstructured graph partitioning and sparse matrix ordering system.* Technical Report, Department of Computer Science, University of Minnesota, 1995.

[46] B. Girgis. Numerical Simulations of Plasma Dynamics using the Flowfield Dependent Variation (FDV) Method. PhD Dissertation, The University of Alabama in Huntsville, 2013.

[47] P. J. Roache. *Verification and Validation in Computational Science and Engineering*. Hermosa Publishers: New Mexico, 1998.

[48] P. Knupp and K. Salari. In *Verification of Computer Codes in Computational Science and Engineering*, Rosen, K. H. (ed.), Chapman and Hall/CRC, Boca Raton, FL, 2003.

[49] C. J. Roy. Review of code and solution verification procedure in computational simulation. *Journal of Computational Physics*, 205(1):131-156, 2005.

[50] C. J. Roy, E. Tendean, S. P. Veluri, R. Rifki, E. A. Luke, and S. Hebert. Verification of RANS turbulence models in Loci-CHEM using the method of manufactured solutions. *AIAA Paper* 2007-4203, 2007.

[51] P. J. Roache. Perspective: A method for uniform reporting of grid refinement studies. *Journal of Fluid Engineering*, 116(3); 405-413, 1994.

[52] O. C. Zienkiewicz, R. L. Taylor, and J. Z. Zhu. *The Finite Element Method: Its Basis and Fundamentals*. Elsevier, sixth edition, 2005.

[53] C. J. Roy, C. C. Nelson, T. M. Smith, and C. C. Ober. Verification of euler/navier-stokes codes using the method of manufactured solutions, *International Journal of Numerical Methods in Fluids*, 44(6):599-620, 2004.

[54] P. J. Roache. Code verification by the method of manufactured solutions. *Journal of Fluid Engineering*, 124(1):4-10, 2002.

[55] W. L. Oberkampf and T. G. Trucano. Verification and Validation in Computational Fluid Dynamics. *Progress in Aerospace Sciences*, 38(3):209-272, 2002.

[56] W. L. Oberkampf and F. G. Blottner. Issues in Computational Fluid Dynamics Code Verification and Validation. *AIAA Journal*, 36(5):687-695, 1998.

[57] R. Samtaney, D. I. Pullin, and B. Kosovic. Direct numerical simulation of decaying compressible turbulence and shocklet statistics. *Physics of Fluids*, 13:1415-1430, 2001.

[58] B. Thornber, A. Mosedale, and D. Drikakis. On the implicit large eddy simulations of homogeneous decaying turbulence. *Journal of Computational Physics*, 226:1902-1929, 2007.

[59] S. Bidadi and S. L. Rani. Investigation of numerical viscosities and dissipation rates of second-order TVD-MUSCL schemes for implicit large-eddy simulation. *Journal of Computational Physics,* 281:1003-1031, 2015.

[60] M. Ciardi, P. Sagaut, M. Klein, and W. N. Dawes. A dynamic finite volume scheme for large-eddy simulation on unstructured grids. *Journal of Computational Physics,* 210:632-655, 2005.

[61] A. N. Kolmogorov. The local structure of turbulence in incompressible viscous fluid for very high Reynolds numbers. *Dokl. Akad. Nauk. SSSR*, 30:301-305, 1941.

[62] M. Oberlack. On the decay exponent of isotropic turbulence. *Proceedings in Applied Mathematics and Mechanics,* 1: 294-297, 2002.

[63] V. Yakhot. Decay of three-dimensional turbulence at high Reynolds numbers. *Journal of Fluid Mechanics*, 505:87-91, 2004.

[64] A. N. Kolmogorov. On generation of isotropic turbulence in an incompressible viscous liquid. *Dokl. Akad. Nauk. SSSR*, 31:538-541, 1941

[65] M. Lesieur. *Turbulence in Fluids*. Kluwer Academic Publishers, fourth edition, Springer, Dordrecht, 2008.

[66] J. A. Domaradzki, Z. Xiao, and P. K. Smolarkiewicz. Effective eddy viscosities in implicit large eddy simulations of turbulent flows. *Physics of Fluids*, 15(12):3890-3893, 2003.

[67] G. Comte-Bellot and S. Corrsin. Simple Eulerian time-correlation of full and narrow-band velocity signals in grid-generated ‘isotropic’ turbulence. *Journal of Fluid Mechanics* 48 (1971) 273-337.

[68] R. Rogallo. Numerical experiments in homogeneous turbulence, Technical Report TM-81315, NASA, 1981.

[69] K. E. Jansen. Large-eddy simulation using unstructured grids. In C. Liu, Z. Liu (Eds) *Advances in DNS/LES* pp. 117-128, Columbus: Greyden, 1997.

[70] P. K. Subbareddy and G. V. Candler. A fully discrete, kinetic energy consistent finite-volume scheme for compressible. *Journal of Computational Physics*, 228:1347-1364, 2009.

[71] C. H. Whiting and K. E. Jansen. A stabilized finite element method for incompressible Navier-Stokes equations using a hierarchical basis. *International Journal of Numerical Methods in Fluids*, 35(1):93-116, 2001.

[72] K. Senguta, G. B. Jacobs and F. Mashayek. Large-eddy simulation of compressible flows using a spectral multidomain method. *International Journal of Numerical Methods in Fluids*, 61:311-340, 2009.

[73] E. T. Spyropoulos and G. A. Blaisdell. Evaluation of the dynamic model for simulations of compressible decaying turbulence. *AIAA Journal*, 34(5):990-998, 1996.

[74] D. P. Rizzetta, M. R. Visbal and G. A. Blaisdell. A time-implicit high-order compact differencing and filtering scheme for large-eddy simulation. *International Journal of Numerical Methods in Fluids*, 42:665-693, 2003.

[75] S. Nagarajan, S. K. Lele and J. H. Ferziger. A robust high-order compact method for large eddy simulation. *Journal of Computational Physics*, 191:392-419, 2003.

[76] M. P. Martín, U. Piomelli and G. V. Candler. Subgrid-scale models for compressible large-eddy simulations. *Theoretical and Computational Fluid Dynamics*, 13:361-376, 2000.

[77] R. H. Pletcher, J. C. Tannehill, and D. A. Anderson. *Computational Fluid Mechanics and Heat Transfer*. CRC Press, third edition, 2013.

[78] H. Yu, S. S. Girimaji and L. Luo. DNS and LES of decaying isotropic turbulence with and without frame rotation using lattice Boltzmann method. *Journal of Computational Physics*, 209:599-616, 2005.

[79] J. R. Ristorcelli and G. A. Blaisdell. Consistent initial conditions for the DNS of compressible turbulence. *Physics of Fluids*, 9(1):4-6, 1997.

[80] P. D. Lax and B. Wendroff. Systems of conservation laws. *Communications on Pure and Applied Mathematics*, 13:217-237, 1960.

[81] S. F. Olatoyinbo, S. L. Rani, and A. Frendi. Large-eddy simulation of decaying isotropic turbulence using the flowfield dependent variation method. *International Journal of Numerical Methods for Heat & Fluid Flow*, in press, 2015.